

**Non-Equilibrium Chalcogen Concentrations in Silicon:
Physical Structure, Electronic Transport, and Photovoltaic Potential**

A thesis presented

by

Mark Thomas Winkler

to

The Department of Physics

in partial fulfillment of the requirements

for the degree of

Doctor of Philosophy

in the subject of

Physics

Harvard University

Cambridge, Massachusetts

October 2009

©2009 by Mark Thomas Winkler

All rights reserved.

**Non-Equilibrium Chalcogen Concentrations in Silicon:
Physical Structure, Electronic Transport, and Photovoltaic Potential**

Eric Mazur

Mark Winkler

ABSTRACT

This thesis explores the structure and properties of silicon doped with chalcogens beyond the equilibrium solubility limit, with a focus on the potential presence of an impurity band and its relevance to photovoltaics. The investigations that we report here shed new light on the electronic role of sulfur dopants in particular, and also provide new evidence of a semiconductor-to-metal transition consistent with the formation of an electron-conducting impurity band. The thesis is divided into three primary studies.

First, we describe doping silicon with a single fs-laser pulse. We find that irradiation above the melting threshold is sufficient for doping a thin layer of silicon to non-equilibrium sulfur concentrations. Next, we explore the interaction of many fs-laser pulses with a silicon substrate. Temperature-dependent electronic transport measurements indicate metallic conduction, while a form of Fermi level spectroscopy and optical absorption data indicate the presence of an impurity band located 200 – 300 meV below the conduction band edge. Third, we investigate silicon doped to non-equilibrium concentrations using a different technique: ion-implantation followed by pulsed laser melting and crystal regrowth. We determine one of the sulfur states present at low sulfur dose. Additional transport measurements point to the presence of a semiconductor-to-metal transition at sulfur doses corresponding to implanted sulfur concentrations just above 10^{20} cm^{-3} .

Finally, in the appendices of this thesis, we describe methods to laser-dope silicon while avoiding the development of significant surface roughness that typically characterizes such samples. Additionally, we present the status of investigations into laser-doping silicon with selenium to non-equilibrium concentrations.

Table of Contents

<i>Abstract</i>	<i>iii</i>
<i>Table of Contents</i>	<i>iv</i>
<i>List of Figures</i>	<i>vii</i>
<i>List of Tables</i>	<i>ix</i>
<i>Acknowledgements</i>	<i>x</i>
<i>Citations to Published Work</i>	<i>xiii</i>
1 Introduction	1
1.1 Motivation	1
1.2 The thermodynamics of converting solar energy to work	2
1.3 High efficiency photovoltaics	6
1.3.1 Multi-junction photovoltaics	6
1.3.2 Impurity band photovoltaics	7
1.4 The delocalization of electron wavefunctions and impurity bands	8
1.5 Connection to this thesis	9
1.6 Organization of the dissertation	10
2 Background	12
2.1 Doping semiconductors to high concentrations	13
2.1.1 Ion implantation	13
2.1.2 Femtosecond laser doping	14
2.2 Properties of fs-laser doped silicon	16
2.2.1 Optical properties and physical structure	16
2.2.2 Electrical properties and devices	19
2.2.3 State of the field	21
2.3 Femtosecond laser irradiation of silicon	22
2.3.1 The optical properties of silicon	23
2.3.2 The interaction of a fs-laser pulse with silicon	25

2.4	Experimental notes and updates	28
2.4.1	Our experimental setup	28
2.4.2	Updates to previous work	30
2.5	What this thesis addresses	33
3	Measurement of electronic transport properties	36
3.1	Literature	37
3.2	The Hall effect	38
3.2.1	A simple approach	38
3.3	The Hall effect and semiconductor statistics	42
3.3.1	Concentration of electrons in the conduction band	43
3.3.2	Impurities and their excitations in a silicon lattice	46
3.3.3	Fitting for the energy of a donor electron state	48
3.3.4	Developing statistical intuition	50
3.4	Impurity bands	54
3.5	Neglect of the Hall scattering factor	57
3.6	The Hall effect and deep sulfur impurities	59
4	Doping silicon beyond equilibrium using a single femtosecond laser pulse	60
4.1	Chapter abstract	60
4.2	Introduction	61
4.3	Experimental setup	64
4.4	Results	68
4.5	Discussion	69
4.6	Conclusion	75
4.7	Acknowledgments	76
5	Optical and electronic properties of femtosecond laser-doped silicon	77
5.1	Abstract	77
5.2	Introduction	78
5.3	Experimental	80
5.4	Results	82
5.5	Discussion	86
5.5.1	Electrical measurements on p-type 1—20 $\Omega\cdot\text{cm}$ silicon	86
5.5.2	Electrical measurements on other silicon substrates	90
5.5.3	Comments regarding potential errors in the measurement of the Hall effect	98
5.6	Conclusion	101
5.7	Acknowledgements	102
5.8	Layer isolation using Silicon-On-Insulator (SOI) wafers	103
5.8.1	Structural considerations when fs-laser doping an SOI wafer	103
5.9	Extended optical absorption data on un-annealed samples	106

6 Silicon doped with sulfur via laser-induced melting and rapid solidification	109
6.1 Introduction	110
6.1.1 Details of S:Si	111
6.2 Experimental setup	112
6.3 Results	116
6.4 Discussion	120
6.4.1 Diode-isolation of the implanted layer	120
6.4.2 Determining the binding energy of implanted sulfur at low doses . .	125
6.4.3 High dose samples and impurity band conduction	130
6.5 Conclusion	134
7 Summary and future directions	136
A Controlling surface morphology in fs-laser doped silicon	140
A.1 Introduction	140
A.2 Experimental	141
A.3 Results	144
A.4 Discussion	147
A.5 Conclusion	150
A.6 Acknowledgements	151
B Femtosecond laser doping of silicon with selenium	152
B.1 Introduction	153
B.2 Experimental	154
B.2.1 Special notes regarding selenium doping	158
B.3 Results	158
B.3.1 Collaborative results	164
B.4 Discussion	165
B.5 Conclusion	170
B.6 Acknowledgements	171
References	172

List of Figures

1.1	Thermodynamic limits of a solar heat engine	4
1.2	Impurity band photovoltaic	7
2.1	Photograph of black silicon process	15
2.2	SEM image of micro-spikes on laser-doped surface	16
2.3	Optical properties of silicon laser-doped using various background gases . .	17
2.4	Cross-sectional TEM analysis of femtosecond laser irradiated silicon	18
2.5	Effect of annealing on optical properties for different chalcogens	19
2.6	Optical absorption as a function of diffusion length	20
2.7	Selected properties of fs laser-doped silicon devices	21
2.8	Band diagram of silicon	23
2.9	Summary of timescales in laser irradiated solids	27
2.10	Schematic: apparatus for femtosecond laser doping	29
2.11	Correcting mistakes in previous optical data	32
2.12	Homogenizing the laser doping process	34
3.1	Geometry for a Hall effect measurement	39
3.2	Model of donor compensation and ionization in semiconductors	46
3.3	Typical trends in $n(T)$ for a doped semiconductor	51
3.4	Graphical techniques for learning about the Fermi level	53
3.5	Equilibrium sulfur donor states in silicon	58
4.1	Sample geometry for Hall measurements	66
4.2	Sample geometry for $I - V$ measurements	67
4.3	SIMS depth profiles and integrated dose	70
4.4	$I - V$ properties of diodes formed via doping with a single laser pulse . . .	71
5.1	Sample geometry for Hall measurements	82
5.2	$I - V$ properties as a function of temperature	83
5.3	Temperature dependent sheet carrier concentration of laser-doped Si	84
5.4	$I - V$ properties of junctions between laser-doped silicon and various substrates	86
5.5	Rectification ratio versus substrate dopant parameters	87
5.6	Band-bending model of a silicon homojunction	93

5.7	Summary of parameter space that achieves rectification	96
5.8	Hall mobility of fs-laser doped silicon	100
5.9	Structure of an SOI wafer	104
5.10	Device layer morphology of laser-doped SOI wafers	105
5.11	Optical absorptance data extended to photon energies of 0.08 eV	107
6.1	Structure of ion implanted and laser melted S:Si	113
6.2	Sheet carrier concentration, resistivity, and mobility – Dose series	117
6.3	Sheet carrier concentration, resistivity, and mobility – Anneal series	118
6.4	Sheet carrier concentration for an SOI wafer implanted with a low sulfur dose	119
6.5	Transition to intrinsic conduction in PLM substrates	121
6.6	Low temperature diode-isolation uncertainties	124
6.7	Fitting carrier concentration data for the sulfur binding energy	127
6.8	Transition to metallic conduction in PLM S:Si	131
6.9	Low temperature mobility in PLM S:Si	133
A.1	Fluence distribution for specular fs-laser doped Si	143
A.2	Photograph and SEM of specular fs-laser doped Si	145
A.3	TEM and SAD of specular fs-laser doped Si	145
A.4	SIMS of specular fs-laser doped Si	146
A.5	Absorptance of specular fs-laser doped Si	147
B.1	Degradation of thin selenium films	157
B.2	SEM image of silicon doped with Se using fs-laser irradiation	159
B.3	Optical properties of silicon doped with Se using fs-laser irradiation	160
B.4	Current-voltage properties of silicon doped with Se using fs-laser irradiation	161
B.5	Temperature dependent charge transport in Se:Si	162
B.6	High temperature carrier concentration for Se:Si	163
B.7	TEM image of Se:Si	165
B.8	Principle component analysis of EXAFS spectra versus infrared absorptance	166

List of Tables

1.1	Record setting photovoltaic efficiencies by technology	5
2.1	Current laser parameters relative to previous work	31
3.1	Estimated critical concentrations for a transition to metallic conduction for selected dopants in silicon	56
4.1	Hall measurements: silicon doped with sulfur using a single laser pulse . . .	69
5.1	Selected properties of silicon substrates laser-doped with sulfur	81
6.1	Sulfur dose and annealing temperature of measured PLM S:Si	114
B.1	Selected properties of silicon substrates laser-doped with selenium	155

Acknowledgements

It is fitting to begin this thesis with acknowledgement of those that made it possible, as every part of it depends on many more people than myself. I must begin by thanking my parents. In the fullest sense of the word, my mom and dad provided me with an education. They read to me as a child, pestered me about that status of my homework, and taught me that milk does a body good. At the time, I did not realize how valuable such an education is, nor the relative rarity of parents that care so deeply about providing one. More importantly, though, they taught me even rarer and more valuable lessons: the paramount value of friends and family, the importance of moderation in all things (including moderation), and a deep love of Cardinal baseball. All were critical to success over the last five years.

My adviser, Eric Mazur, is responsible for the field in which I have spent the last several years working, and has unwaveringly supported me as I did so. Eric trusts his graduate students implicitly; empowering them to be originators not only of their own research, but also portions of the research process in which students do not typically participate. As evidenced by both their research and hiking abilities, Eric's graduate students become strong, independent scientists as a result.

The Mazur group is as much a way of life as it is a group of people making new science happen — but I will stick to the science in these pages. I learned the true secrets of

scientific research from mentors such as Brian, Geoff, Rafa, Tommaso, and Cleber. Those in the Mazur group learning alongside me — Eric and Jess — helped me digest what they meant. The constructive criticism and support of colleagues and friends such as Jason, Yu-Ting, Paul, Kevin, Prakriti, Loren, Tina, Sam, Jim, Iva and Maria taught me what a research community is. On a daily basis, I cannot imagine a more creative or helpful person to have shared a lab with than Eric Diebold; I am likewise grateful to Renee, who was an outstanding partner and critical ear for many of the experiments in this thesis. The size and scope of the Mazur group prevents me from recognizing the important role that all its members played in creating my academic home over the last five years, but each member played their own role in making that home a reality.

Throughout the last several years, I had the good fortune of frequently interacting with the faculty who ended up on my thesis committee. Both Michael Aziz and Tonio Buonassisi gave abundantly of their time and intellect throughout this process. They encouraged collaboration and offered thoughtful criticism of my work. I am a better scientist for my interactions with them.

My scientific community extended well beyond the Mazur group and my committee, though. I learned the power of and discipline required for collaborative work together with Bonna, Joe, and Matt. I also am indebted to their advisers, Tonio Buonassisi and Silviya Gradecak, for providing the intellectual, financial, and personal support that made the collaboration possible. The Aziz group, especially Dan, Ikurou, and Atsushi, worked hard to provide me with samples and help me understand the material they were giving me. The Harvard community is filled with talented people that support students in their efforts: whether it is Stan in the machine shop, Jim in the electronics shop, or Noah and the entire staff of CNS, I rarely had to approach a technical task alone. I also owe a great deal to the Harvard Energy Journal Club and the students that comprise it. As my academic home

away from home, I certainly learned as much at our Monday meetings as I did anywhere else at Harvard. Finally, some of my friends and colleagues occasionally provided me a literal home away from home toward the end of this process. Kurt and Joyce graciously opened their door to me whenever I needed it, as did Bill and Cara.

Finally, it is impossible to imagine the last five years absent the love, support, and companionship of my best friend and wife, Jess. What we have seen together in the last five years is a far more coherent reminder of what is possible in that amount of time than any research that I have done: whether the number of weddings we have witnessed (fourteen, including our own), the number of nieces and nephews we have welcomed into our lives (four), the number of advanced degrees we have accumulated (also four), or the cumulative amount of time we have each spent on the Fung Wah bus traveling to see each other (about a month each). Here's to what's possible in all of the years to come!

*Mark Winkler
Cambridge, Massachusetts
October, 2009*

Acknowledgements of Financial Support

This thesis is based on work funded by the National Science Foundation under contract CBET-0754227, and support from the National Science Foundation Graduate Research Fellowship.

Citations to Published Work

Parts of this dissertation cover research reported in the following articles:

- [1] M. T. Winkler, M. Sher, and E. Mazur, “Doping silicon with a single femtosecond laser pulse,” *soon to be submitted for publication in Physical Review B*.
- [2] M. T. Winkler, M. Sher, and E. Mazur, “Controlling the surface morphology of femtosecond laser doped silicon,” *soon to be submitted for publication in Optics Express*.
- [3] B. Newman, J. Sullivan, M. Winkler, M. Sher, M. Marcus, M. Smith, S. Gradecek, E. Mazur, and T. Buonassisi, “Illuminating the mechanism for sub-bandgap absorption in chalcogen doped silicon materials for pv applications,” in *European Union Photovoltaic Solar Energy Conference*, (Hamburg, Germany), 2009.
- [4] P. G. Maloney, P. Smith, V. King, C. Billman, M. Winkler, and E. Mazur, “Emissivity of microstructured silicon,” *submitted for publication in Applied Optics*.
- [5] B. R. Tull, M. Winkler, and E. Mazur, “The role of diffusion in broadband infrared absorption in chalcogen-doped silicon,” *Applied Physics A – Materials Science Processing*, vol. 96, no. 2, 2009.
- [6] T. Shih, M. T. Winkler, T. Voss, and E. Mazur, “Dielectric function dynamics during femtosecond laser excitation of bulk ZnO,” *Applied Physics A – Materials Science Processing*, vol. 96, no. 2, pp. 363–367, 2009.

*To my amazing wife JESSICA,
for your love, support, and companionship*

*When you get to a fork in the road,
take it.*

YOGI BERRA

Chapter 1

Introduction

1.1 Motivation

Photovoltaics convert energy from radiant heat into useful work. They are thus heat engines, and the first and second laws of thermodynamics place a very general upper limit on the efficiency with which they can convert heat to work. As originally proposed [1] and derived [2] by Carnot and Clausius, respectively, a thermodynamic cycle accepting heat Q_{hi} from a high temperature heat reservoir ($T = T_{hi}$), rejecting a portion of that heat to a low temperature reservoir ($T = T_{lo}$), and converting the difference W to work, can have no higher an efficiency than that of a reversible cycle. This limiting efficiency is:

$$\frac{W}{Q_{hi}} = \eta = 1 - T_{lo}/T_{hi}. \quad (1.1)$$

This limit is known as the Carnot limit, and is named after a specific, reversible thermodynamic cycle that achieves this efficiency. Thermodynamics is mute how or whether one might achieve this efficiency. Regardless, one utility of this relationship is in providing a metric against which we can measure the performance of a particular implementation of a

heat engine.

For a terrestrial device converting the heat contained within the near-blackbody spectrum emitted by the sun, the Carnot limit is quite generous. Absorbing heat from a reservoir at approximately 6000 K and, as required by the 2nd law, rejecting waste heat at the lower terrestrial temperatures of approximately 300 K, the ultimate efficiency is approximately 95%. Currently, photovoltaics operate at substantially lower efficiencies.

Achieving higher efficiencies is one route to lowering the cost of energy from solar power, an important goal for a carbon-neutral energy economy. This thesis is concerned with a non-equilibrium doping technique that may represent a route toward realizing an impurity band photovoltaic. Such a device has substantially higher limiting efficiencies than current photovoltaic technology. Thus, we motivate our work with a brief thermodynamic discussion that makes clear the potential gains from pursuing higher photovoltaic efficiencies.

1.2 The thermodynamics of converting solar energy to work

We begin by considering a general heat engine that converts radiant solar heat into useful work (not necessarily a photovoltaic, which would be a specific type of solar heat engine). The thermodynamics of converting solar energy into work are highly influenced by the degree to which we concentrate the sunlight onto our solar heat engine.¹ We define a concentration factor c as

$$\begin{aligned} c &= \frac{\text{solid angle subtended by the sun as seen by solar heat engine}}{4\pi} \\ &= \frac{\Omega_{conc}}{4\pi}, \end{aligned} \tag{1.2}$$

where we have defined Ω_{conc} as the solid angle that the sun occupies in the field of view

¹Reference [3] gives a particularly lucid discussion of the thermodynamic complexities introduced by the radiant transfer of heat, as opposed to heat transfer by conduction or convection.

of the solar heat engine. Lacking any effort to concentrate the sunlight, Ω_{conc} is simply equal to $\Omega_{sun-earth}$, the solid angle subtended by the sun from the earth. It is convenient to define

$$\begin{aligned} c_0 &= \frac{\Omega_{sun-earth}}{4\pi} \\ &\approx \frac{6.8 \times 10^{-5}}{4\pi} \\ &\approx 5 \times 10^{-6}, \end{aligned} \tag{1.3}$$

as the concentration factor for unfocused sunlight. By focusing sunlight it is conceivable for the sun to occupy the entire 4π steradians field of view of the photovoltaic; thus c can range from c_0 to 1. In practice, it is difficult to achieve concentrations much higher than $c/c_0 = 1000$.

We can derive several interesting limits to the efficiency of solar energy conversion as a function of concentration factor. For example, we can insist the entire process be reversible, in which case — provided we concentrate the solar radiation sufficiently — we can come very near the limit of 95% given by equation 1.1. We can also consider the maximal efficiency that results from using radiative heat from the sun to bring a terrestrial heat reservoir to a high temperature, which is then used to provide heat to a Carnot engine. This scheme would describe the ultimate efficiency of a technology such as concentrated solar thermal, in which solar radiation is used to heat a working fluid that drives a electric turbine. The results of such calculations, similar to those derived in reference [4] and discussed in more detail in reference [3], are shown in Figure 1.1.

If we choose instead to use a photovoltaic — a device that converts solar energy directly to an electric current driven across a resistive load — as our solar heat engine, there exists more restrictive thermodynamic limitations. To date, photovoltaic technology is dominated by semiconductors, specifically silicon, in which there is a single characteristic

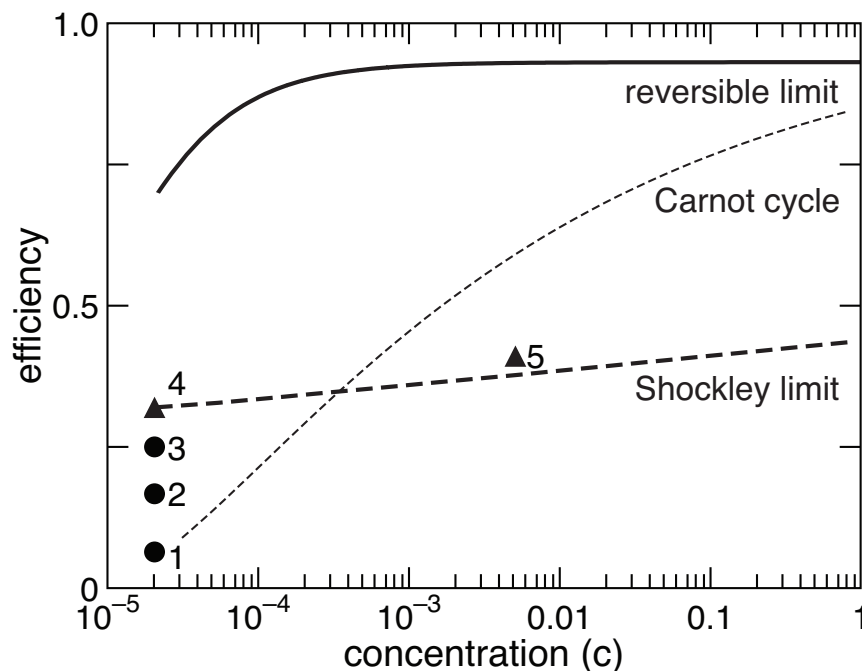


Figure 1.1: Thermodynamic efficiency limits of a solar heat engine. Several important limits are plotted, such as the ultimate reversible limit (solid line), the efficiency of running a Carnot cycle using the absorbing body as the high temperature reservoir (light dashed line), and the Shockley-Queisser limit of photovoltaic efficiency (heavy dashed line). Also plotted are record-setting efficiencies for several technologies, enumerated in Table 1.1.

absorbing energy E_g . Photons with energy less than E_g pass through the absorber unaffected, while photons with energy greater than E_g are absorbed, but produce an amount less than E_g of work. Taken together with the principle of detailed balance, which enforces microscopic reversibility on such a system, we obtain an efficiency limit that is generally lower than the other limits considered in Figure 1.1. This limit, also shown in Figure 1.1, is the so-called Shockley-Queisser limit, originally derived for illumination under a blackbody [5] and later modified for the details of the solar spectrum [6].

Superimposed on Figure 1.1 is the maximal recorded efficiency of several different photovoltaic technologies [7]. We see that current records are well below the reversible thermodynamic limit, even at high concentration. When comparing the crystalline Si record to

Figure 1.1 label	absorber material(s)	c/c_0	η [7]
1	organic	1	6.4%
2	CdTe	1	16.7%
3	crystalline Si	1	25.0%
4	GaInP/GaInAs/Ge	1	32.0%
5	GaInP/GaP/Ge	454	41.1%

Table 1.1: Enumeration by technology of record-setting cells designated in Figure 1.1. Note that entries 4 and 5 are multijunction cells, and are not limited by the Shockley limit. All data is drawn from reference [7]

the Shockley limit, however, we see that the designers of semiconductor photovoltaic cells have done an impressive job extracting a high percentage of the work that is thermodynamically available to them given the platform they are using. For example, the maximum recorded efficiency for a silicon solar cell is $\eta = 25\%$, while the Shockley-Queisser limit for silicon is 31% — thus the technology has realized over 80% of its thermodynamic potential. To put this in perspective, the nation’s fleet of coal-fired power plants operates with an average efficiency of about 35%² despite limiting efficiencies (according to equation 1.1) of over 60%.³

The solution, as we see from from Figure 1.1, is to pursue photovoltaic technologies — points 4 and 5 in the figure are examples — that can exceed the Shockley limit and come closer to the reversible limit. Technologies exist that can yield efficiencies substantially closer to the reversible thermodynamic limit, and we discuss them next.

²according the Energy Information Agency, heat rates for coal fired primary energy conversion average 10,000 BTU / kW · hr, which is equivalent to a thermodynamic efficiency of about 36%

³Simply using equation 1.1 with $T_{hi}=775$ K, a typical boiler temperature in a sub-critical coal power plant according to MIT’s excellent overview of coal power: ”The Future of Coal,” available at <http://web.mit.edu/coal/>

1.3 High efficiency photovoltaics

The largest irreversible loss in a semiconductor photovoltaic with a single absorbing gap stems from attempting to simultaneously satisfy the two primary goals of harvesting solar photons:

1. to absorb as large a fraction of incident photons as possible (*i.e.* generate a large photocurrent); and
2. to extract as large a quantity of free energy per photon as possible (*i.e.* generate a large voltage).

Unfortunately, these two goals are at cross-purposes in a semiconductor. Meeting the first of the two goals implies choosing a material with a small band gap; however, this choice will yield a small voltage. Meeting the second of the two goals implies choosing a material with a large band gap, but such materials absorb fewer photons and generate smaller photocurrents.

1.3.1 Multi-junction photovoltaics

We mentioned above that points 4 and 5 in Figure 1.1 were not subject to the Shockley limit. They represent multi-junction solar cells, which use multiple absorbing layers, each tuned to a different portion of the solar spectrum. By doing so, high and low energy photons are absorbed in regions with large and small band gaps, respectively. This scheme does indeed meet both goals enumerated above, and — as evident in Figure 1.1 — they can achieve considerable improvements in efficiency. However, practical considerations intervene in this otherwise ideal solution. Cell designs often include rare materials such as indium that are not sufficiently abundant to scale to the terrawatt production levels necessary for a globally significant energy source [8]; in addition, the growth procedures

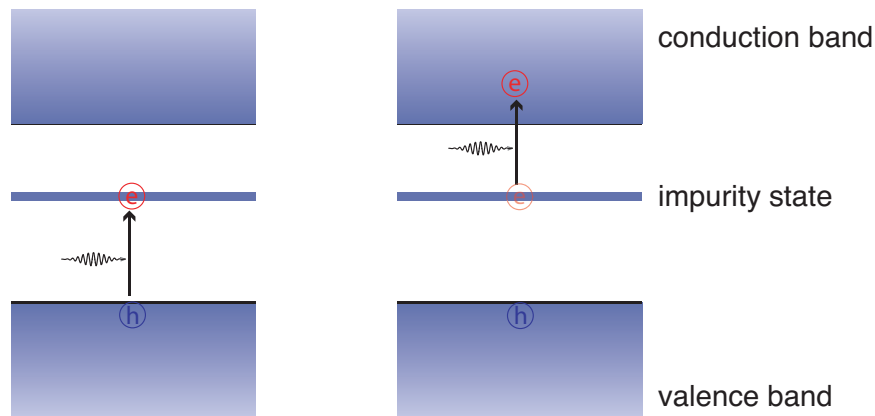


Figure 1.2: The premise of the impurity photovoltaic effect: impurities with energy states within the band gap of the absorber facilitate the creation of charge carriers through the absorption of two or more lower energy photons.

necessary to integrate the multiple layers are costly. The question of whether the higher efficiency of a multi-junction cell can compensate for these problems is a subject of debate. Other technologies, however, may offer a way around this problem.

1.3.2 Impurity band photovoltaics

An alternative high efficiency approach is the impurity band photovoltaic. The use of impurities to increase absorption in semiconductor photovoltaics was suggested very early in their development [9]. The basic appeal is evident in Figure 1.2, in which two photons with energy less than the band gap give rise to a free electron-hole pair via an impurity energy level somewhere in the band gap of the host material.

To significantly increase absorption of infrared energy in the solar spectrum, however, the optically sensitive impurities must be located relatively deep in the band gap of the host material. Such localized impurities have long been recognized to be responsible for non-radiative recombination [10,11], a process in which a free electron and free hole recombine within the material and generate heat rather than useful work. Recently, however, it was pointed out that when such impurities are present in sufficiently high concentration,

they may form an impurity band which suppresses such impurity-mediated recombination, while still facilitating the absorption of photons with energy less than the band gap [12,13]. The concept of “lifetime recovery” through an *increase* in deep states was recently demonstrated [14]. The first demonstration of an impurity band photocurrent involved the use of quantum dot superlattices [15], but more familiar materials are currently an area of intense research interest [14,16]. Impurity band photovoltaics have ultimate efficiencies approaching 65%, far higher than the Shockley-Queisser limit [12].

1.4 The delocalization of electron wavefunctions and impurity bands

Mott originally explained that the delocalization of electron wave functions in highly doped semiconductors can occur through an electron-electron interaction that screens the binding fields of the electron-donating centers [17–19]. This transition in a semiconductor — from low density, localized dopant-electron behavior to high density, delocalized dopant-electron behavior — is part of a broader phenomenon known as the metal-insulator transition. For most of the last century, though, research into this effect in silicon has focused on shallow donors such as boron and phosphorus [19–23]. Researchers have also studied the effect that impurity bands have on electronic transport for shallow donors in GaAs [24–26] and CuInSe₂ [27] as well.

There is a substantial body of literature regarding the transition from insulating to metallic conduction in extrinsic semiconductors; a great deal of it is reviewed in reference [23]. Reviewing that literature is beyond the scope of this document, but we will mention several pertinent aspects here. Semiconductors, by definition, are a condensed state of matter characterized by finite conductivity *only* at finite temperature. Thus the rigorous

experimental proof of an insulator-to-metal transition is a measurement of non-zero conductivity at (or very near) $T = 0$ K. For phosphorus in silicon, for example, this occurs at a critical density of $3.75 \times 10^{18} \text{ cm}^{-3}$ [28]. Fundamentally, this transition to a metallic state occurs when impurity states are spaced so closely that the Coulomb attraction that binds donor electrons to their parent dopant atoms is sufficiently screened by the wavefunctions of neighboring donor electrons that such bound states are no longer stable. This description is effectively the same that Mott gave to describe the transition from an insulating to a metallic state [19], and is still frequently invoked [23]. Mathematically, we can state this condition as:

$$n_c^{1/3} a_h^* = C_0, \quad (1.4)$$

where n_c is the critical density above which a material acts as a metal, a_h^* is the Bohr radius of the impurity's donor electron, and C_0 is a constant that Mott predicted would be of order unity. Empirically, C_0 has been found to have the value $C_0 = 0.26$ for a broad class of materials [22]. Recently, some authors have suggested that C_0 might be as large as 0.88 for deep states in silicon [13].

1.5 Connection to this thesis

This thesis discusses chalcogen impurities — such as sulfur and selenium — in a silicon lattice at concentrations approaching or above the critical concentration for the Mott transition. As we will see in Chapter 2, this does indeed lead to the absorption of photons with energy less than the band gap of silicon, as would be expected for an impurity band material. Already several interesting devices have been demonstrated from this technique, but many questions remain regarding these materials and their suitability for the impurity band photovoltaic effect. This thesis addresses some of the outstanding questions regarding

the structure and nature of electronic transport in these materials.

1.6 Organization of the dissertation

The central theme of this thesis is investigating the physical and electronic structure of non-equilibrium concentrations of chalcogens — primarily sulfur, and to a lesser extent selenium — in a silicon lattice.

Chapter 2 reviews the experimental techniques employed in this thesis. Both techniques — ion implantation followed by pulsed laser melting and resolidification, as well as irradiation of a silicon wafer by intense femtosecond laser pulses in the presence of the chalcogen — are briefly reviewed. Significant attention is given to the femtosecond laser process, as this thesis contributes not only to characterizing such samples, but also to development of the process itself.

Chapter 3 summarizes the theory of the electronic transport measurements relevant to this thesis.

Chapter 4 investigates the interaction of a single laser pulse with a silicon wafer in the presence of a sulfur hexafluoride background gas. Structural, electronic, and optical properties are considered.

Chapter 5 addresses the electronic properties of silicon doped with sulfur to non-equilibrium concentrations using many femtosecond laser pulses above the ablation threshold.

Chapter 6 presents temperature-dependent electronic transport measurements of silicon doped to non-equilibrium concentrations via ion-implantation followed by pulsed laser melting and crystalline regrowth.

Chapter 7 summarizes the work in this thesis, and places it in the context of

outstanding challenges in our understanding on non-equilibrium chalcogen-doped silicon.

Appendix A describes experimental advances in controlling the morphology of femtosecond laser doped silicon.

Appendix B describes the current status of investigations into fs-laser doping of selenium.

Chapter 2

Background

This thesis is concerned with the structure and properties of silicon doped with chalcogens — primarily sulfur, but also selenium — beyond the solid solubility limit. We will primarily consider doping silicon with sulfur using femtosecond laser pulses; we will also consider some comparisons to sulfur included via ion-implantation, and selenium included using a femtosecond laser. We note here that although part of the allure of the doping techniques described in this thesis is their potential extension to host materials other than silicon and dopants other than sulfur and selenium, we will limit our discussion to the study of sulfur and selenium impurities in a silicon matrix.

The purpose of this chapter is to summarize the state of non-equilibrium chalcogen doping in silicon as it is relevant to the remainder of this thesis, and also motivate a new approach to studying this material. We begin with a historical overview, followed by a brief review of the physics of the interaction between a fs-laser pulse and a silicon surface. We follow with a few experimental details and improvements implemented over the course of this thesis, and conclude with the outstanding issues that motivate and are addressed by this thesis.

2.1 Doping semiconductors to high concentrations

Impurities play a critical role in determining many properties of silicon, such as the optical [29, 30], electrical [31–33], and in some cases structural properties [34]. When impurities are used intentionally to control such properties, we refer to them as dopants, and fairly exhaustive reviews of known information for common dopants in silicon are readily available [35–37]. The earliest approaches for achieving controllable dopant concentrations in semiconductors were equilibrium techniques that involved bringing the host material — whether as a liquid or solid — to a temperature that yielded significant solubility of the desired dopant. We can determine the maximum solubility of a given element from its equilibrium phase diagram, and such information is available for many common elements [37]. Sulfur and selenium, the elements of interest to this thesis, have equilibrium solubility limits around 10^{16} cm^{-3} [37–40]. To achieve the high concentrations necessary to exceed the Mott limit (as described in chapter 1) with materials that have relatively low equilibrium solubility in silicon, other doping techniques are necessary.

2.1.1 Ion implantation

Ion implantation — the firing of highly energetic ions at an otherwise cold lattice — can place high concentrations of impurities into a host lattice according to predictable spatial distributions [41]. The energy dissipated by the decelerating ions, however, often causes significant rearrangement of the host lattice and degrades any pre-existing crystal order. Crystal order can be re-established via thermal annealing; however, such processes may cause dopant concentrations above the solubility limit to precipitate out. Alternatively, pulsed lasers (with pulse durations in the ns — μs regime) can melt the implanted layer [42, 43]; subsequent resolidification will, under certain circumstances, occur epitaxially atop the crystalline substrate [44]. In the process, if the velocity of the resolidification front

exceeds that of the diffusive velocity of the dopants, the dopants can be trapped in a process known as solute trapping. The dopants, or solutes, are often trapped in substitutional sites [43]. Accurate and predictive theories [45–47] exist to describe the thermodynamics and kinetics of solute trapping.

Using this technique, highly non-equilibrium concentrations of dopants can be trapped. The concentration of the dopant still has an upper limit, which is the solubility of the dopant along the liquidus line of the phase diagram; this limit is about 5×10^{21} cm^{-3} for most materials [48]. However, this concentration is generally above that required for a Mott transition to metallic conduction [19], and offers the possibility to explore the creation of impurity bands with well known dopant distributions in silicon crystals free of extended defects. Indeed, several research groups are exploring the creation of impurity band photovoltaics [14] and other sub-band gap devices [49] using these techniques.

In this thesis, we will explore silicon supersaturated with sulfur using ion implantation followed by pulsed laser melting and crystal regrowth. Details of the particular process relevant to this thesis can be found elsewhere [49,50], and we will summarize the pertinent experimental specifics in chapter 6.

2.1.2 Femtosecond laser doping

Femtosecond laser-doping is an alternative approach to achieving non-equilibrium dopant concentrations; however, this technique did not originate with doping in mind. Over ten years ago, the Mazur group began exploring the interaction of femtosecond laser pulses with a silicon surface. The first reports regarded the development of spikes and ripples on the surface of a silicon wafer exposed to a series of femtosecond laser pulses above the ablation threshold (Figures 2.1 and 2.2) [51,52].¹ As visible in Figure 2.1, this

¹Unless otherwise mentioned, all the experiments described in this section involve the interaction of 100s of laser pulses with a silicon surface, and a laser fluence above the silicon ablation threshold. For clarity and

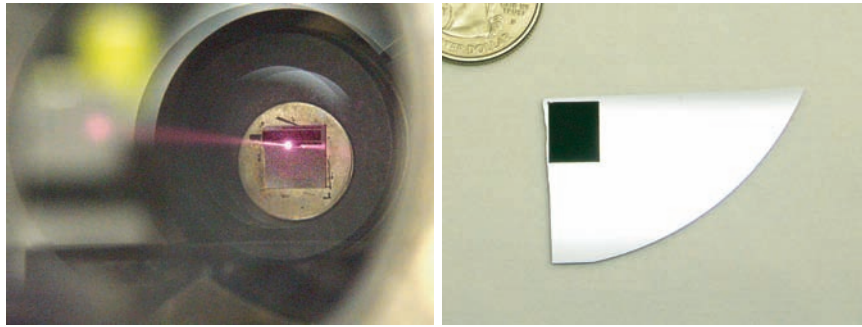


Figure 2.1: *Left*: Photograph of the laser interacting with a silicon substrate; view is just off-axis of the laser-beam toward the silicon wafer *Right*: A silicon wafer after irradiation in an SF_6 environment with laser pulses above the ablation threshold.

laser-induced surface roughness lends to the silicon a strikingly black appearance, which quickly earned it the casual name “black silicon.” In general, fs-laser irradiation near or above the ablation threshold leads to the development of spikes or bumps between the nano- and micro-scale, both in height and spacing; however, the exact morphology was found to depend strongly on the the chemical species and phase of the ambient environment [53, 54]. The Mazur group eventually explained these morphological features [55] as an evolution of laser-induced periodic surface structures, a very general phenomena that can be observed on many different types of solids [56–59]. The laser-induced surface roughness is an interesting field of study in its own right, and the Mazur group has demonstrated significant control over the size, spacing, and other details of the morphology [52, 54, 60]. The morphology continues to be fruitful field of study for applications including field emission [55], superhydrophobicity [61], and surface-enhance raman scattering [62]. A thorough review of the morphology can be found in reference [63]; details have also been published regarding the crystal structure of the silicon ejected from the surface during the ablation process [64].

Researchers soon realized that the development of this morphology, however, occurred alongside a second process: doping silicon with the ambient chemical species to

brevity, we refer the reader to the references for experimental particulars.

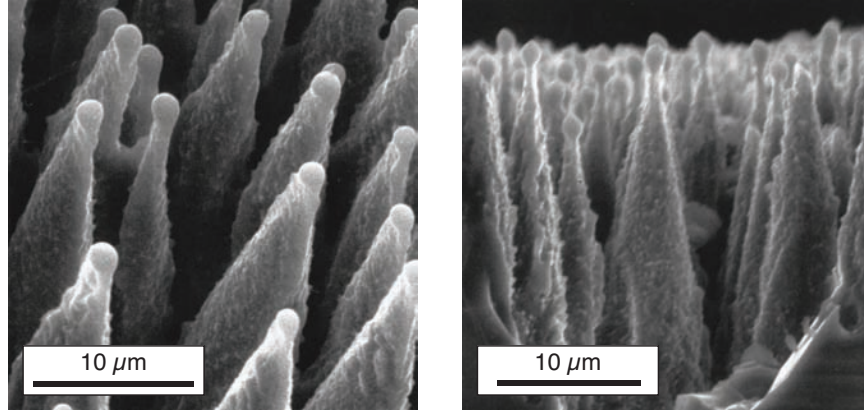


Figure 2.2: Scanning electron microscope images of a surface microstructured in SF_6 , both are taken from reference [51]. *Left:* A view 45° angle from the original surface normal *Right:* A cross-sectional view of the spikes obtained by cleaving the wafer.

highly non-equilibrium concentrations. As we will discuss in detail below, atoms from the ambient environment are implanted into the silicon wafer during irradiation at concentrations above 10^{20} cm^{-3} . In Chapter 4 and Appendix A we demonstrate conclusively that this doping process and the development of the “black” surface morphology are independent phenomena. Next we will summarize what is known regarding this new doping process.

2.2 Properties of fs-laser doped silicon

2.2.1 Optical properties and physical structure

Shortly after reporting the fs-laser induced surface roughness described above, the Mazur group reported that the same laser-structured silicon exhibited anomalous sub-bandgap infrared absorption for photon energies as low as 0.5 eV (Figure 2.3) [65], despite silicon’s typical transparency to photons with energy less than its room-temperature band gap of $E_g = 1.12 \text{ eV}$. After exploring the dependence of this infrared absorption on background gas and laser parameters, it was realized that the absorption of sub-band gap photons was connected to the presence of sulfur in the ambient environment [53, 55, 66, 67].

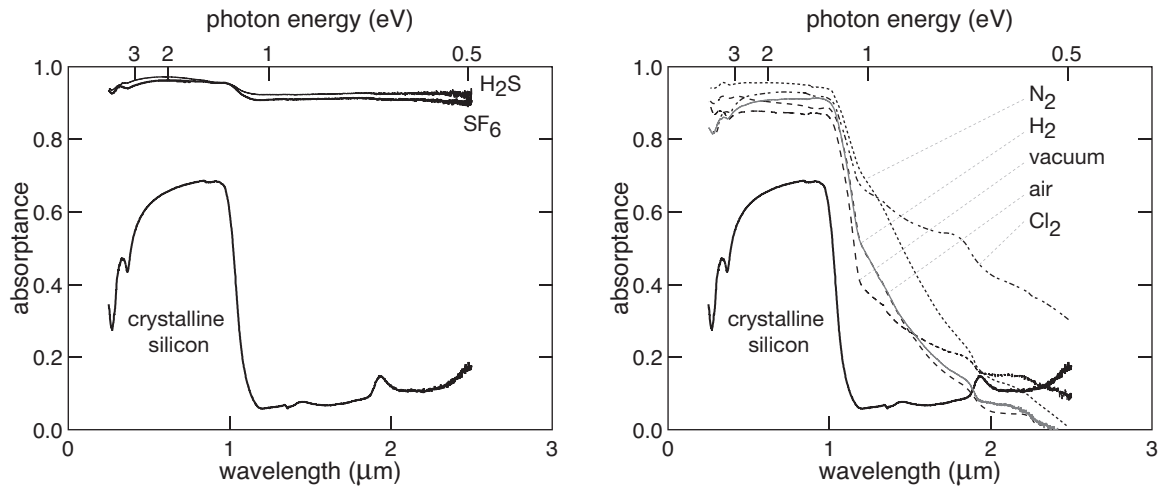


Figure 2.3: *Left:* Near-unity absorption of photon energies (top-axis) less than the band gap of silicon occur for sulfur containing gases (adapted from [67]). *Right:* When a silicon wafer is irradiated in the presence of non-sulfur containing gases, it shows only defect-like absorption at the band-edge (adapted from [53]).

Shortly afterward, the Mazur group demonstrated that similar sub-band gap absorption occurred whenever the ambient environment included one of the heavy chalcogens (S, Se, Te) [68]. Secondary ion mass spectroscopy (SIMS) and Rutherford backscattering spectrometry (RBS) indicated that — in each case of high sub-band gap absorption — chalcogen dopants were present in extraordinarily high concentrations. Although the surface roughness present for all of these measurements creates quantitative difficulty for SIMS and RBS techniques, chalcogens were clearly present in concentrations of approximately 10^{20} cm^{-3} . The equilibrium solubility limit for both sulfur and selenium is approximately 10^{16} cm^{-3} [37–40].

An investigation of the crystal structure of fs-laser doped silicon revealed that the doped region coincided with a region of silicon that had lost a degree of crystalline order (Figure 2.4). Cross-sectional transmission electron microscopy indicated a polycrystalline region extending approximately 100 nm from the surface — roughly the region that RBS and SIMS indicated was supersaturated with the dopant. Although selected area diffrac-

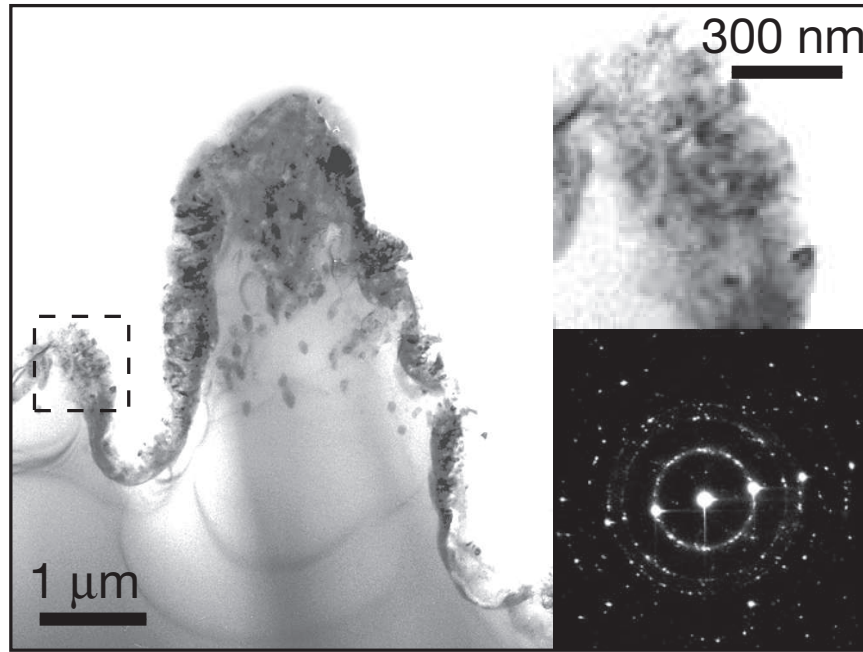


Figure 2.4: Cross-sectional TEM imaging of a silicon surface irradiated with fs-laser pulses significantly above the ablation threshold in a background gas of SF_6 . *Left and upper right*: bright field images show the laser modified surface layer. *Lower right*: Selected area diffraction analysis of the laser modified surface layer. Images obtained from reference [66].

tion (SAD) indicated a distinctly polycrystalline nature to the laser-affected region, the researchers estimated the grain size to be 50 nm or less [66,69]. Thermal annealing, however, brought about significant recovery of crystallinity, as evidenced in both the bright field TEM, as well as the selected area diffraction.

The effect of annealing on the sub-band gap optical properties has also been investigated. If the infrared absorption arose from a non-equilibrium concentration of chalcogens, researchers hypothesized that thermal treatment should facilitate a return to equilibrium and loss of the sub-band gap optical absorption. As shown in Figure 2.5, annealing does indeed reduce the sub-band gap absorption [65,66]. By exploring this behavior for the entire family of chalcogens, a complicated relationship was found between the deactivation of infrared absorption, the dopant species, and the parameters of the thermal annealing (Figure

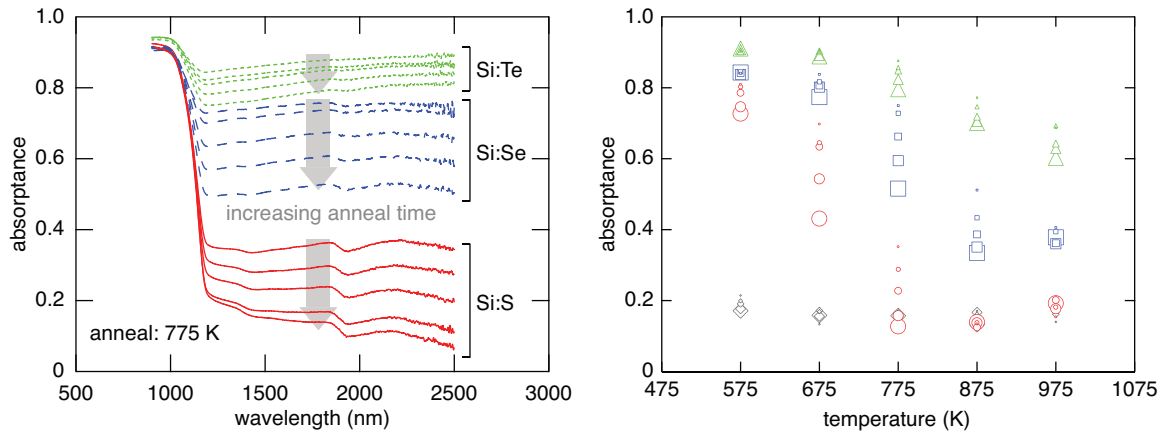


Figure 2.5: In these plots we observe the dramatically different manner in which optical properties respond to annealing depending on the dopant chosen (see reference [70]) *Left:* Absorption spectra for silicon irradiated in the presence of sulfur (red), selenium (blue) and tellurium (green) after annealing at 775 K for increasing lengths of time. *Right:* Average absorbance between 1250–2500 nm for sulfur (circles), selenium (squares), and tellurium (triangles) for various temperature (x-axis) and times (size of marker) anneals. The time of the anneals was (from smallest to largest): 10 min, 30 min, 100 min, 6 hr, 24 hr).

2.5). The Mazur group later showed that this behavior is more easily understood when viewed as a function of the diffusion length of the dopant (Figure 2.6) [70], in which case all data points collapse onto a similar curve. Figure 2.6 also clearly shows that the deactivation of the dopant occurs on a length scale similar to the grain size. We have suggested (in reference [70]) a potential model that explains this behavior. Briefly, the model proposes that dopants contribute to infrared absorption so long as they are within crystalline grains and coordinated with the silicon lattice, but precipitate into a non-optically sensitive phase when they reach grain boundaries. The results of this model are also shown on Figure 2.6.

2.2.2 Electrical properties and devices

The electrical properties of chalcogen-doped silicon have also been probed. The current-voltage properties of the junction between the laser-doped region and the substrate were investigated, and the junction was observed to rectify (Figure 2.7). Also, room temper-

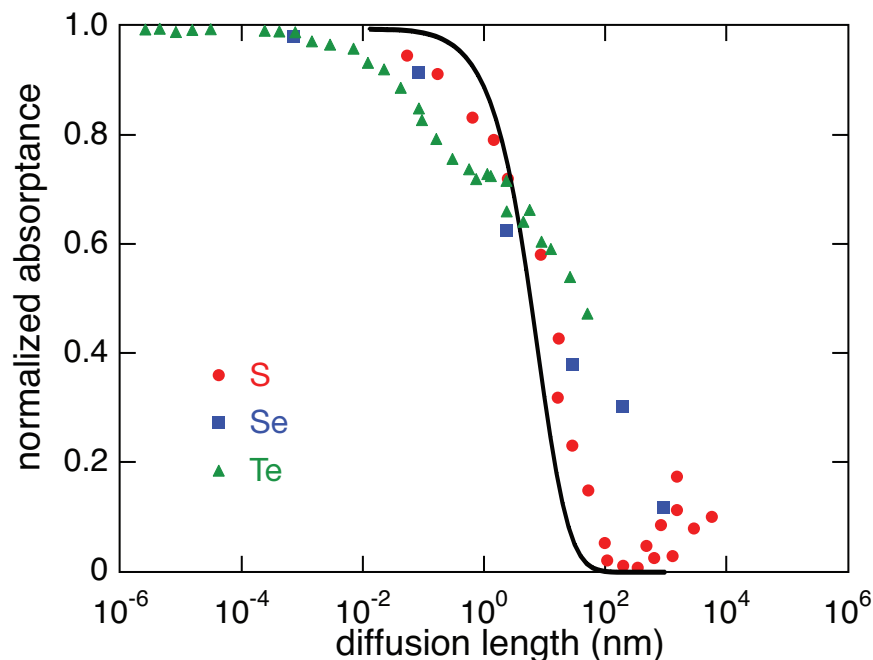


Figure 2.6: We use the annealing time t and temperature T to calculate the diffusion length $d = \sqrt{Dt}$ of the dopant (where D is the temperature dependent diffusivity). We see that despite the widely varying behaviors seen in Figure 2.5, the average infrared absorption behaves similarly when viewed in this fashion. The dark line plots the result of the model described in the text. Data is primarily from reference [70], with some more recent data shown as well.

ature Hall measurements indicated that the sulfur dopants were indeed acting as electron donors, changing the sign of the Hall coefficient when a p-type silicon substrate was laser-doped [55].

The presence of both infrared absorption and rectification led to speculation that the fabrication of a silicon-based infrared detector would be possible. Early work on avalanche photodiodes [65] demonstrated the promise that fs-laser doping had for silicon-based infrared detection. A short time later, the Mazur group demonstrated a low-bias silicon photodiode with responsivity to photon energies as low as 0.8 eV [71]. The geometry of this device is shown in Figure 2.7. The fs-laser doped photodiode, when operated at low biases of only a few volts or less, not only exhibited photoresponse for photon energies as

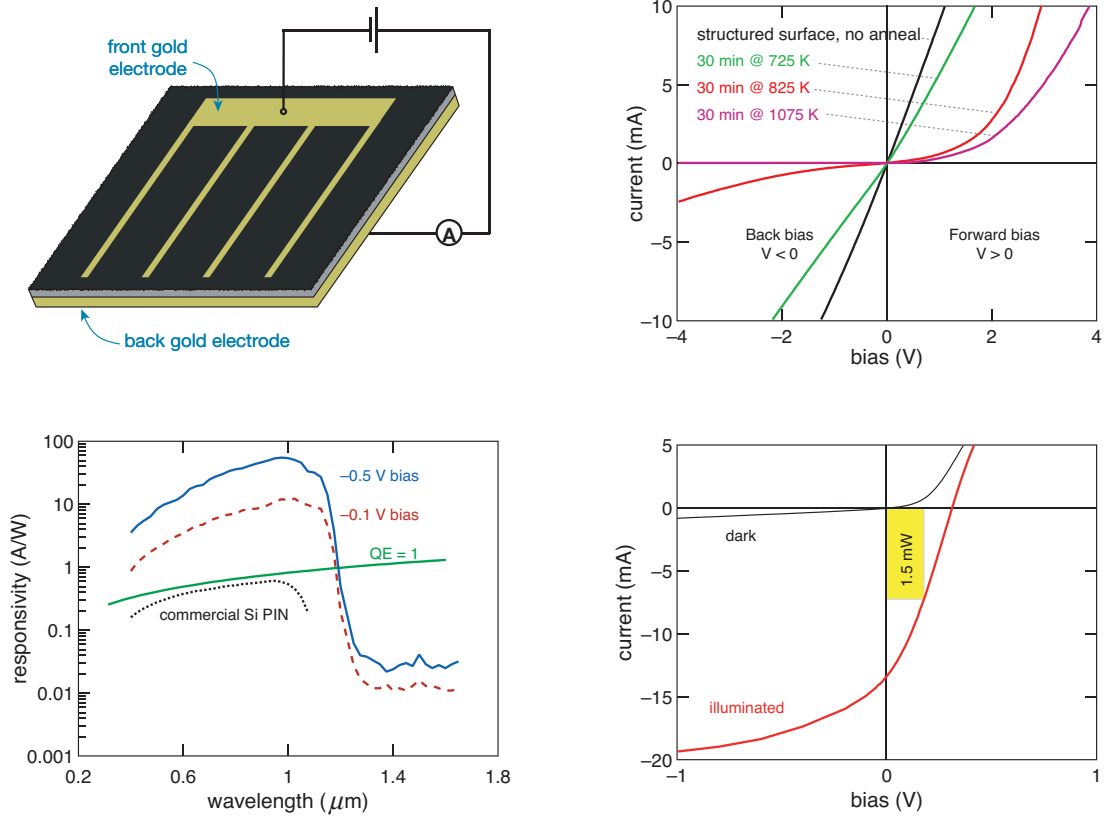


Figure 2.7: *Upper left*: Device geometry; *Upper right*: the current voltage relationship exhibits rectification after a brief anneal; *lower right*: photovoltaic performance has been demonstrated under AM 1.5 solar irradiation; and *lower left*: at low bias we observe significant gain in the visible, and measurable response in the infrared [55, 71]

small as 0.8 eV, but also tremendous gain (Figure 2.7). These phenomena remain unexplained. Demonstration photovoltaics have also been fabricated [55, 72], but have demonstrated low efficiency ($\eta < 2.5\%$). To date, we have no evidence that sub-band gap photons are converted to free electron-hole pairs capable of doing work in an external circuit.

2.2.3 State of the field

Sulfur and selenium have long been recognized as double donors in silicon that introduce states deep within the band gap [38, 73], and these states have previously been investigated for their potential in IR-detection [29, 74, 75]. Additionally, lasers have been

involved in doping and annealing semiconductors for decades [43,76]. In retrospect, perhaps it seems quite plausible that short pulsed laser should serve to implant chalcogen dopants into silicon, which should then in turn serve as absorption centers as well as electron donors.

However, several outstanding questions remain wholly unanswered by this scenario. Foremost is the broad, featureless nature of the absorption exhibited by fs-laser doped silicon. Doping to equilibrium levels introduces resonances rather than the featureless absorption we observe. As we will explore in chapter 6, similar optical properties are observed in chalcogen-doped silicon that is prepared in a wholly different manner, and that possesses a markedly different (and more intact) crystal structure. This raises the question of whether the absorption is a more universal phenomena related to high chalcogen concentrations than we first assumed. If so, this begs the question of what state or states give rise to this absorption. Can we understand it as an impurity band, and if so, can it be exploited for greater photovoltaic efficiencies? Before proceeding to this question, though, we provide a brief review of the femtosecond laser literature as it relates to silicon, and summarize several updates we have made to our experimental procedures.

2.3 Femtosecond laser irradiation of silicon

This thesis deals in large part with dopants incorporated into a silicon lattice via femtosecond laser irradiation. In the historical overview offered above, we largely ignored the question of what happens when a femtosecond pulse strikes the surface of our silicon wafer. There is a diverse array of literature concerned with this question [77–91], and we briefly summarize the points pertinent to this thesis. This process and the relevant literature has also been described in more detail and with commendable clarity elsewhere [55,72].

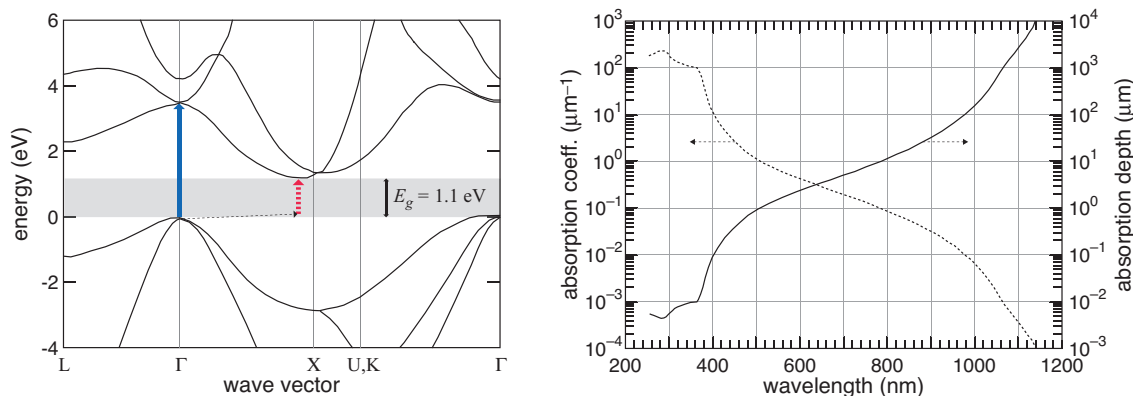


Figure 2.8: *Left*: Band diagram of silicon, from [92]. Figure was originally adapted by the author, and modified slightly for use in [72]. *Right*: Linear absorption coefficient and absorption length of intrinsic silicon at 300 K as a function of wavelength of the absorbed photon. Data obtained from [93], originally adapted in this format for [72].

2.3.1 The optical properties of silicon

The band diagram of silicon is shown in Figure 2.8. Optical absorption via an electronic transition is possible for any photon with energy greater than about 1.1 eV. For photons with energy between approximately 1.1 and 3.4 eV, however, the excitation of an electron from the valence band maximum to an empty state in the conduction band requires momentum from a phonon. The attendance of a phonon for this transition makes absorption in this manner far less likely than for a so-called direct transition, one in which no momentum and thus no phonon is required. The relative probabilities of these phenomena is clearly reflected in the enormous difference in the absorption depth for the two processes (see Figure 2.8). For a direct transition, a photon must travel only 10 nm or so before absorption; while for an indirect transition the photon must meander through the silicon nearly 1000 times farther: about 10 μm .

The above statements are only true, however, provided the photons do not perturb the potential landscape in which they are traveling, which is to say: as long as we reside in the regime of linear optics. The experiments described in this thesis employ femtosecond

laser pulses, however, and as we will see below, absorption of such pulses tends to be non-linear in nature.

Fs-lasers are used in a diverse range of fields and applications in both research and industry; several excellent reviews of their design and use are available [94,95]. Besides their other interesting properties and uses, short pulses of light can exhibit incredibly high peak electric fields. We can see this quite easily from Maxwell's equations, which tell us that the irradiance (or Poynting vector) is related to the electric field by:

$$\langle S \rangle = \frac{1}{2} c \epsilon_0 E^2, \quad (2.1)$$

where $\langle S \rangle$ represents the average irradiance. If we approximate average irradiance (power per area) as the energy in our pulse (2.5 mJ) when focused to a circle of radius 5 μm (achievable with an inexpensive lens), arriving over a pulse duration of 50 fs, we arrive at a peak electric field of $E \approx 10^{12} \text{V/m}$ — an electric field far in excess of the binding fields of an electron to an atom, which are on order 10^9V/m ! We should draw two conclusions from this calculation. The first is that the interaction of a fs-laser pulse with silicon will be quite different than what the data of Figure 2.8 would tell us. Second, and perhaps more qualitatively, these enormous fields mean that we can drive matter into exotic conditions, in which a large fraction of the valence electrons are removed from bonds over a potentially non-thermal timescale. There is no immediate intuition to be drawn from this, other than the fact that exploring new regimes of material conditions — whether it is preparing a very cold, very small, or very hot set of conditions — often stimulates the discovery of new physics and materials. We proceed below with a description of how this intense interaction occurs.

2.3.2 The interaction of a fs-laser pulse with silicon

The absorption of a femtosecond laser pulse requires careful attention primarily for two reasons. First, the magnitude of the electric field associated with the pulse implies a fundamentally non-linear absorption process, which means that the quantities given in Figure 2.8 can no longer be of assistance in determining the absorption depth. And second, because electrons are the particles that first absorb the energy in a laser pulse, and because it takes between 1 and 10 ps for a hot electron gas to thermalize with a crystal lattice [78], there is a highly non-equilibrium environment immediately following laser pulse absorption. This highly non-equilibrium scenario is characterized by an extremely hot (several 1000 K) electron gas inside of a room temperature lattice. All of the details of what happens next follows from these two facts and the intensity of the laser pulse.

The non-linear interaction of the laser pulse with the silicon lattice can dramatically decrease the absorption depth, and thus the volume into which the laser energy is deposited. Early in the study of the interaction of picosecond laser pulses with a silicon surface, it was recognized that short pulse irradiation led to the formation of a high-density electron-hole plasma at the silicon surface [78–82], and several researchers made the observation that the simple energetics of the melting threshold (about 2 kJ/m²) implied a decreased absorption length [80, 82]. After the invention of the femtosecond laser, pump-probe spectroscopy demonstrated that melting occurred a significant time after the arrival of the laser pulse (about 1 ps after the arrival of a 90 fs laser pulse in this case), demonstrating the intermediate role and timescale of the electron-hole plasma in conveying the laser energy to the lattice [83, 84]. The creation of this electron-hole plasma can change the characteristics of the laser-silicon interaction, even over the course of a single pulse [85].

Thus a physical picture emerges in which the front portion of the fs-laser pulse is absorbed to create a dense electron hole plasma, which then absorbs (and partially reflects)

the remaining portion of the pulse. The important observation, for the sake of this thesis, is that the absorption length for the fs-laser pulse is effectively orders of magnitude smaller than Figure 2.8 would suggest. We will observe this directly in chapter 4.

What happens after the absorption of the pulse can vary a good deal, and depends entirely on the wavelength and energy of the laser pulse. As mentioned above, the lattice thermalizes with the hot electron gas on a timescale of about 1 ps. If the energy of the pulse is sufficient to remove 10–15% of valence electrons from bonding states, the lattice becomes unstable and transitions to a liquid before the heat is transferred to the lattice via electron-phonon coupling; this process known as non-thermal melting [84, 86–88]. At pulse energies that do not initiate such abrupt disordering of the lattice, however, the hot electron-hole plasma distributes its energy to the lattice over several picoseconds via electron-phonon coupling. This heat diffuses inward through the silicon lattice from the surface, raising its temperature and — if there is sufficient heat to raise the lattice temperature above the melting point — causing a transition to a liquid state near the surface. The melt depth will increase with laser energy until, at still higher energies, boiling will occur at the surface. As the liquid phase becomes superheated, the gas phase can nucleate at high rates in the melt and eject material from the silicon surface. This process is known as ablation. The thresholds for these phenomena are subject to precise experimental details. For example, melting and ablation thresholds for 620 nm, 120 fs laser light have been reported to be 1.5 and 3.0 kJ/m² [89, 90]; authors using the same wavelength and slightly shorter (90 fs) pulses report the melting threshold to be 1 kJ/m² [83]. Still other authors report the melting threshold for 780 nm, 100 fs laser pulses at 2.5 kJ/m² [91]. There appears to be some ambiguity in the literature, as to whether or not threshold fluence is reported as the incident fluence F , or incident fluence corrected for reflection at the incident wavelength $F/(1 - R)$. For 30 ps, 532 nm laser pulses, the melting threshold is more universally agreed

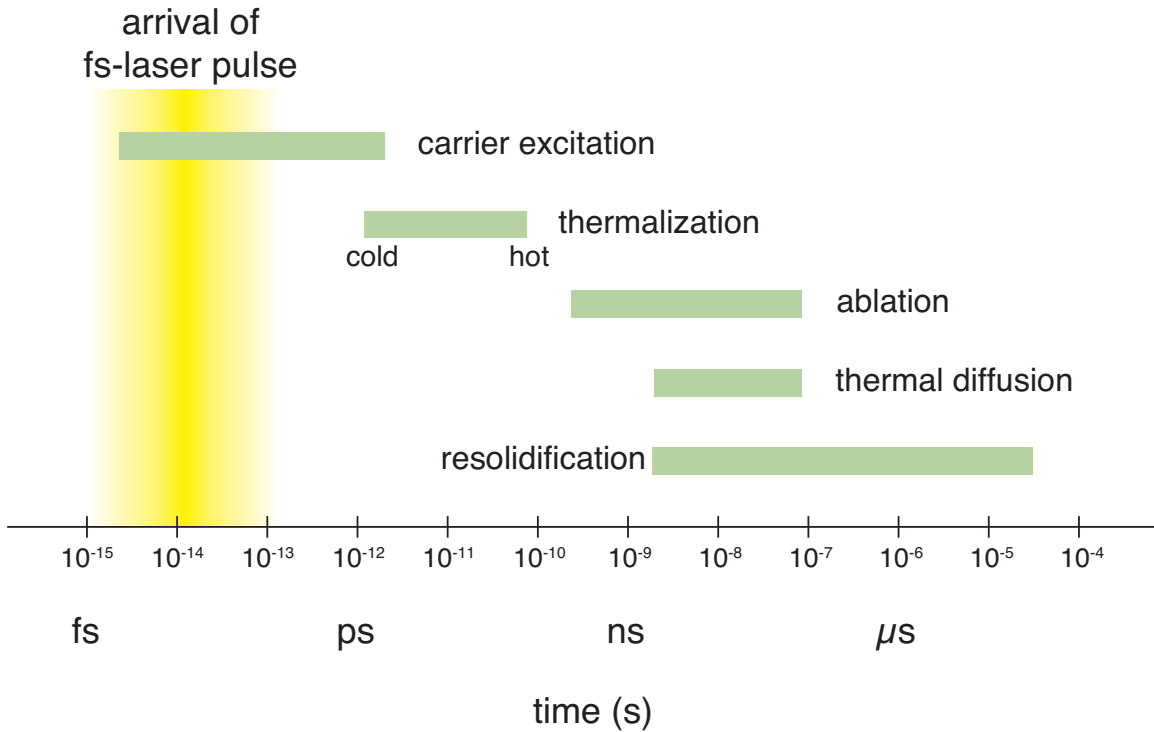


Figure 2.9: An approximate summary of important material processes compared to our femtosecond laser pulse. This log-scale timeline shows that the arrival of the laser pulse is over before even the fastest lattice processes. The graphic also shows the timescales of other important physical phenomena, such as material ablation, thermal diffusion among the lattice nuclei, and resolidification of a fs-laser melted surface. A more detailed discussion of this graphic can be found in reference [103]

upon to be 2.1 kJ/m^2 [77–82] Several excellent papers [77, 86, 87, 90, 91, 96–102] discuss the details of melting and ablation in greater detail; several melting thresholds are compiled and compared to a theoretical model in reference [102].

Perhaps more important for most of the work in this thesis, however, is the nature of solidification, which occurs several nanoseconds after irradiation [78, 103]. Again, this phenomenon is highly dependent on precise experimental conditions. For 30 ps laser pulses at $\lambda = 532 \text{ nm}$, laser-melted silicon re-solidifies in the amorphous phase at fluences just above the melting threshold of 2.1 kJ/m^2 , but in a crystalline arrangement at fluences above 2.5 kJ/m^2 [77–79]. Similar observations have been documented for approximately

100 fs-laser pulses [91], but the thresholds for amorphization and crystallization were found to be 2.5 and 5.5 kJ/m², respectively, although the authors are unclear on precisely what pulse duration they employ. As the authors in reference [44] and [77] discuss, the physical issue underlying this problem is the time it takes for epitaxial growth to occur. If the resolidification front moves faster than 15 m/s [96], atoms do not have time to find their equilibrium positions, and the resolidified layer will be amorphous. If the molten phase persists longer and the re-solidification front moves more slowly, then in general epitaxial re-growth will occur; in this case the re-solidified layer will be crystalline. In general, higher laser fluences will generate longer melt durations and slower re-solidification fronts. Thus, a common theme in laser-melting literature is that after exposure to a laser pulse just above the melting threshold, silicon re-solidifies as an amorphous solid; at some higher fluence threshold, however, melting is followed by crystalline regrowth. The timescales of the phenomena discussed above are summarized in figure 2.9.

2.4 Experimental notes and updates

The experimental setup used for laser-doping has been reviewed extensively elsewhere [55,72]. We briefly review it here. We also note, for the convenience of future students, some changes to “standard operating procedures” that may be convenient to know as one gets to know the history of the project.

2.4.1 Our experimental setup

In the experiments described in this thesis, we employ amplified femtosecond laser pulses of temporal duration $\tau \leq 100$ fs and center wavelength $\lambda = 800$ nm. The repetition rate of the pulse train (*i.e.* the number of pulses generated per second) is any integer division of 1000 (*e.g.*, 1000 Hz, 500 Hz, 333 Hz, *etc*). The pulse has an approximately Gaussian

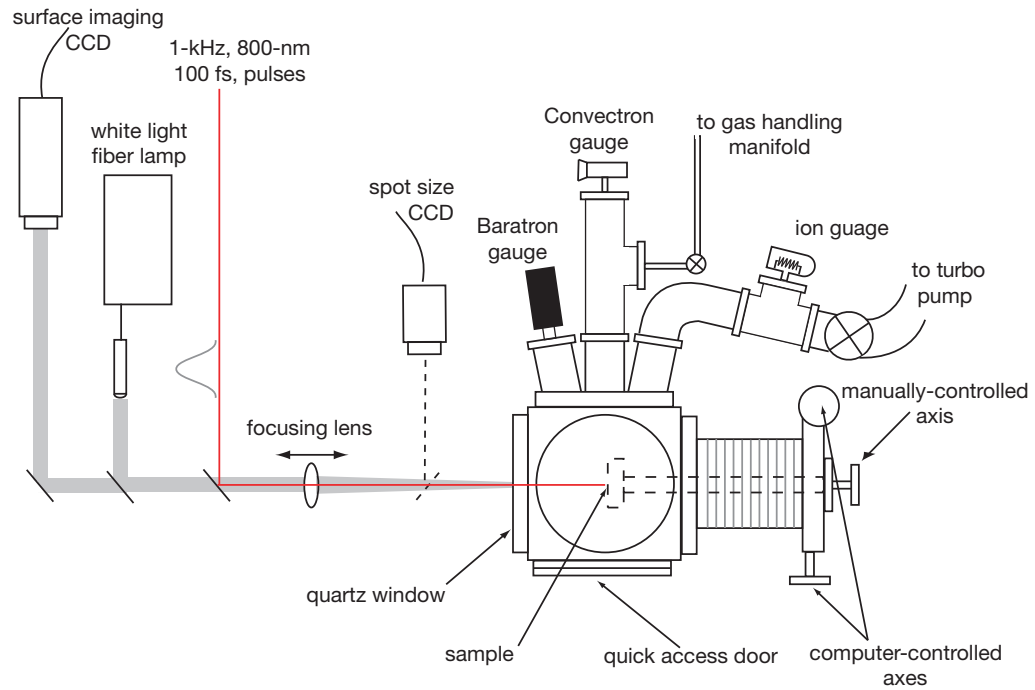


Figure 2.10: A schematic representation of the femtosecond laser-doping apparatus.

spatial profile, and an average pulse energy is 2.5 mJ. We can vary pulse energy continuously down to approximately 50 μJ using a half-wave plate to rotate the pulse polarization prior to temporal compression, a process that employs polarization sensitive optics. We direct the train of fs-laser pulses to the setup depicted schematically in Figure 2.10.

We prepare a silicon wafer for laser exposure using an RCA clean [104] followed by a dilute (5% HF) etch in hydrofluoric acid to remove the native oxide. If we are introducing Se or Te as dopants, we thermally evaporate a thin (75 nm) layer of that dopant onto the silicon wafer. We immediately load the wafer into the vacuum chamber, and evacuate the chamber to high vacuum (pressure $\leq 10^{-5}$ Pa). We then backfill with a gas: if we are introducing sulfur into silicon, we backfill with 6.7×10^4 Pa of SF_6 ; if we are doping using a thin solid film of Se or Te, we fill the chamber with the same pressure of N_2 .² The wafer

²In references [55] and [72], we find that the ambient gas has a tremendous impact on the hydrodynamics

is positioned in front of the focus of the fs-laser pulse, which is sent through a $f = 350$ mm plano-convex lens as it travels toward the vacuum chamber. A CCD camera, carefully positioned at an identical distance from a glass pick-off as the silicon wafer, is used to measure the spatial profile of the laser pulse.

The lens is positioned to create a spatial intensity profile at the wafer surface with a full-width at half-maximum w . The laser repetition rate is set to a frequency f ; the wafer is translated in the x-direction in front of the beam using stepper motors a distance typically on order of 1 cm, stepped vertically a distance Δ_y , translated in the reverse direction, and the process is repeated. We assign a quantity, shots per area, to the exposure; it is defined as:

$$S/A = \frac{\pi w^2}{\Delta_x \Delta_y} = \frac{f \cdot \pi w^2}{v \Delta_y}, \quad (2.2)$$

where $\Delta_x = v/f$, and all other quantities were defined above. The details of translation are selected in order to distribute laser pulses across the surface in a fashion that is particular to the experiment. Typically we fix $\Delta_x = \Delta_y$, a subject discussed further in section 2.4.2.

2.4.2 Updates to previous work

In this section, we emphasize differences between the fs-laser doped samples produced for this thesis and prior work [55, 72]. Most of these changes were made for the sake of greater sample cleanliness or experimental accuracy.

Changes to the experimental setup

If comparing these results to previous work, note the following changes in procedures.

- We cleaned the interior of the vacuum chamber before most sample runs. Cleaning consisted of wiping down surfaces with methanol and baking out ($T_{peak} < 150$ °C) for

of melting and ablation; thus, an inert atmosphere is used during fs-laser doping with a thin solid film

approximately 24 hours before most fabrication runs. A turbo pump was installed, with a dry scroll pump (rather than an oil pump) backing it. Typical base vacuum for the bake out was in the 5×10^{-8} torr range, with typical pre-doping pump down to approximately $< 10^{-6}$ torr.

- We installed a new laser system, which we use for all experiments except those of Appendix A. Important parameters for both laser systems are outlined in Table 2.1 below.
- We clean all silicon wafer substrates with the RCA clean prior to laser-doping

	Previous laser	Current laser
pulse duration (fs)	> 100	< 70
pulse energy (mJ)	0.3	2.5
center wavelength (nm)	800	800
repetition rate (Hz)	1000	1000

Table 2.1: Changes to laser parameters relative to previous work

Corrections to optical data

Previous reports of optical data regarding fs-laser doped silicon included errors in the optical absorbance. Because laser-doped silicon has a rough surface that generates diffuse reflection, an integrating sphere is necessary measure reflectance. However, the coating used in the integrating sphere — intended to be a uniform reflector, with a reflectance of $R = 1$ over the entire spectral range of interest — has significant spectral features in the infrared. These features introduced spurious data at $\lambda = 1400$ nm and $\lambda = 1900$ nm, as well as a general positive slope of the absorbance in the infrared. We have corrected these

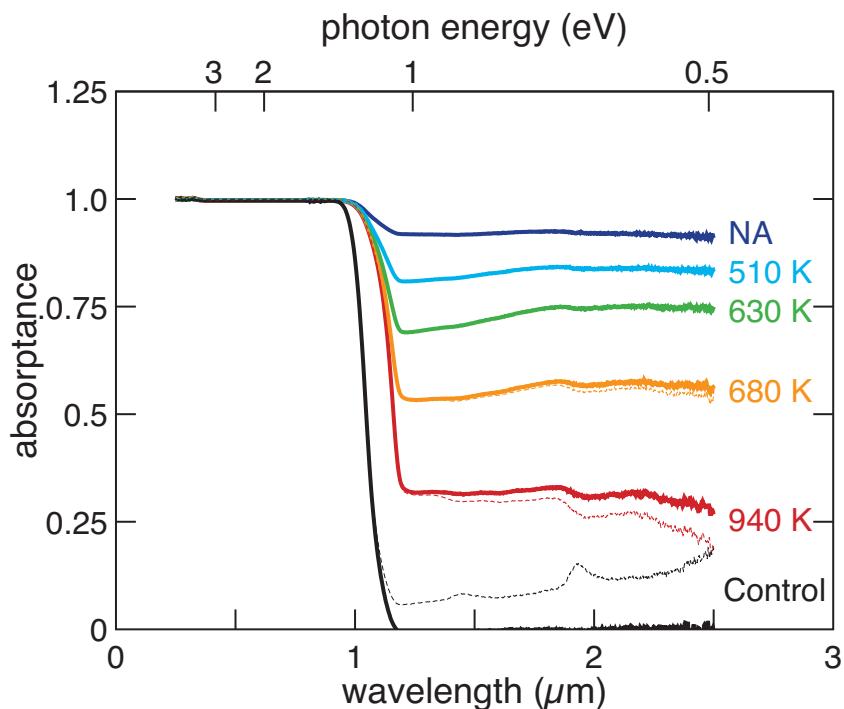


Figure 2.11: Absorbance of a boron-doped ($1 - 20 \Omega\cdot\text{cm}$) silicon wafer irradiated with a homogenized 100 shots per area in a 500 torr SF_6 environment. Uncorrected data is shown with dotted lines; corrected data is shown with solid lines. The derivation of the correction can be found in [105].

errors using an unpublished technique that involves careful comparison to references [105].

Example data, both inclusive of and corrected for the error, are shown in Figure 2.11.

Also, in Figure 2.11 we show normalized absorbance ($\bar{A} = (1 - R - T)/(1 - R)$) as opposed to absorbance $A = 1 - R - T$. Normalizing the absorbance in this fashion expresses the fraction of light absorbed that penetrates the initial air-silicon interface. This measurement accurately reflects the fact that silicon absorbs strongly in the visible (see, for example, Figure 2.8). Additionally, provided we had a non-roughened surface, \bar{A} would allow us to calculate the absorption coefficient for absorption through a uniform medium of thickness d , neglecting internal reflections:

$$\bar{A} = I(d)/I_0 = \exp(-\alpha d). \quad (2.3)$$

Homogenizing the doping process

Finally, we mention briefly a change to typical laser exposure conditions. Prior to this work, researchers employed a laser exposure scheme in which the following parameters would be typical:

$$\Delta_x = v/f = w/100 \quad (2.4)$$

$$\Delta_y = w/2, \quad (2.5)$$

where $\Delta_{x,y}$ is the spacing between incident laser pulses on the silicon surface, v is the velocity with which the silicon wafer is translated in x-direction, f is the repetition rate of the laser, and w is the full-width at half-maximum of the laser spatial-intensity profile. Such an exposure recipe results in a highly non-uniform distribution of laser pulses across the silicon surface. This inhomogeneity has evident consequences that are visible as streaks and lines in laser-doped areas. The problem was exacerbated when we installed a higher power laser which enabled larger a w ; an example is shown in Figure 2.12. To correct this problem, we homogenized the irradiation pattern such that $\Delta_x = \Delta_y$. A new laser exposure parameter was defined

$$S/A = \frac{\pi w^2}{\Delta_x \Delta_y}, \quad (2.6)$$

where all parameters were defined above, except S/A which is the shots per area. The success of this method in reducing large-scale inhomogeneities is obvious in Figure 2.12.

2.5 What this thesis addresses

It is the author's hope that this section gave the reader an appreciation for the history and state of knowledge of non-equilibrium chalcogen doping prior to the writing of

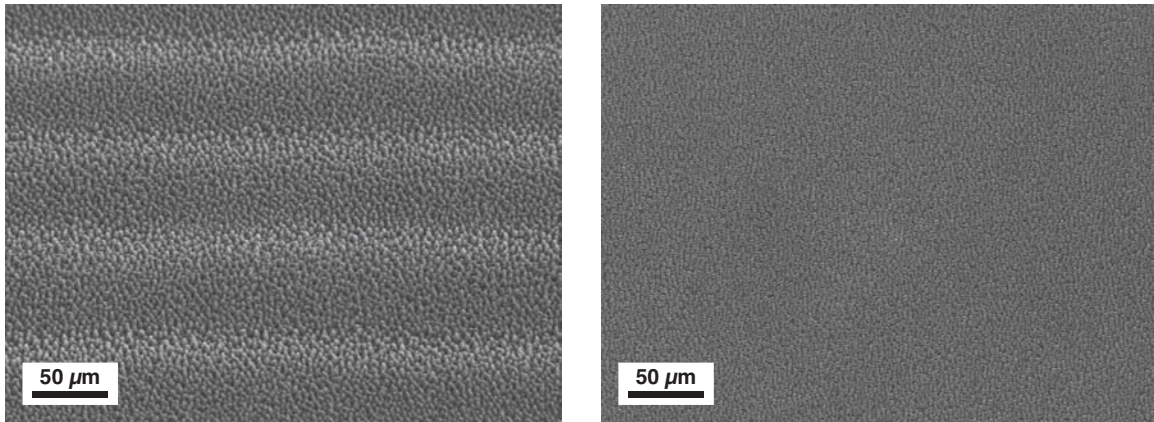


Figure 2.12: *Left:* Using the previous method of laser exposure, streaks and lines are visible. *Right:* These can be corrected by distributing laser shots identically on both exposure axes.

this thesis. As implied in Chapter 1, the motivating question behind this work is whether a supersaturation of chalcogen dopants in silicon represent a practical technique for realizing intermediate-band photovoltaics. Before an intelligent approach to the technological question can be formulated, we must investigate the fundamental nature and material physics of non-equilibrium chalcogen concentrations in silicon. The techniques and methods used to interrogate non-equilibrium chalcogens — which have to-date often centered around device fabrication rather than fundamental science — have not sufficiently reduced the system to its basic components. Thus a central theme of this thesis is developing new techniques and model systems for studying the physics of highly chalcogen doped silicon, rather than its device properties. The focus of this development is always to answer the questions that, in the view of the author, are currently the most pressing:

- Does non-equilibrium chalcogen doping of silicon introduce an impurity band of delocalized electronic states within the band gap of silicon?
- If so, what is the location and width of that band inside the gap? What are its optical properties?

- Regardless of the presence of an impurity band, what structural and electronic states are formed during the doping process? Through what mechanisms do they give rise to absorption of photons with energy less than the band gap of silicon?

In the next chapter, we outline the new experimental methods developed for this thesis. In Chapter 4, we address the structural and electronic nature of the sulfur included by a single fs-laser pulse in order to learn about the process of laser doping. In later chapters, we will explore the temperature dependence of electronic transport in silicon doped to non-equilibrium levels with fs-laser pulses as well as by ion implantation followed by pulsed laser melting. The goal of these transport measurements is to identify the energy state(s) of the chalcogen dopants and to understand the nature of the electronic conduction. Armed with this information on physical and electronic structure, we will conclude with a critical analysis of the successes and failures of this approach, and what we have learned regarding the suitability non-equilibrium chalcogen doping for impurity band photovoltaics.

Chapter 3

Measurement of electronic transport properties

Because of the simple relation between the Hall coefficient and the electron concentration ... it undoubtedly occupies the position of PRIMUS INTER PARES amongst the transport properties of conductors.

E.H. Putley in “The Hall Effect and Its Applications”

The construction of an apparatus for the measurement of the temperature-dependence of the Hall effect was a major effort during this thesis. Although only a portion of this thesis is devoted to the study of such data, we summarize the relevant theory and literature for the benefit of future students, as well as results discussed later. Over 130 years have passed since Edwin Hall discovered his namesake effect [106]¹, and thus many excellent specialist’s texts exist on the subject [107–110]. Thus, the focus of this chapter is brevity and relevance to the experimental results that follow.

¹as a graduate student

3.1 Literature

We begin by referring the reader to several excellent references. Reference [107] gives an excellent theoretical treatment of the Hall effect; reference [108] is often cited in this regard as well, but the author has found it less helpful. For the experimentalist, reference [109] treats the subject in a manner that is perhaps more relevant. A wonderful mix of history, theory, and experimental wisdom is given in reference [110], while brief but helpful primers to the subject appear in several review articles [111, 112], including one specifically for polycrystalline materials [113]. Understanding the Hall effect in semiconductors demands a detailed knowledge of semiconductor statistics, which is carefully reviewed in reference [114] – a reference that is a familiar and essential citation in any paper regarding the interpretation of temperature-dependence of the free carrier concentration in semiconductors. Additionally, an understanding of the errors introduced by experimental concerns such as contacts is critical to understanding the measurement of either the Hall effect or the resistivity [115–118]

Finally, the question of deriving knowledge of impurity bands from Hall measurements was first addressed by Mott [18, 19]. Experimental specifics for GaAs [24–26], CuInSe₂ [27], and to some extent Si [119–121] have all been explored. To a large extent, the literature regarding the question of impurity band conduction is concerned with the fundamental nature of the transition between insulating and conducting instances of the solid state; to the extent that extrinsic semiconductors offer a platform to study this transition, a great deal of work over the last 50 years is reviewed in reference [23].

3.2 The Hall effect

The Hall effect offers tremendous insight into nearly all classes of materials, and especially crystalline or partially crystalline semiconductors. If a means is established to study the effect as a function of temperature, a wealth of information can be determined, including dopant and impurity concentrations, dopant binding energy, and host material band gap. The general experimental geometry is shown in Figure 3.1. A current density of magnitude J is excited in the \hat{x} direction in a slab of the material to be studied. The slab is immersed in a magnetic field of magnitude B oriented in the direction \hat{z} . As we will show below, the Lorentz force causes deflection of the charge within the current in the \hat{y} direction; this deflection continues until the displaced charge sets up a field that exactly cancels the Lorentz force. The exact geometry of the slab can take several forms, so long as the current in the \hat{y} direction is exactly zero when the measurement is made.

3.2.1 A simple approach

In this section we will present a brief derivation of the physics behind the Hall effect. The approach may seem overly complex — indeed, we will neglect most of the more sophisticated adjustments we discuss below anyway — but is intended to help the Hall-effect initiate become familiar with subtleties often addressed only obliquely in the literature. For experimental reasons, we will be forced to neglect many of these considerations, such as the value of the Hall scattering factor r_H , but we will make the case that this is unimportant for the results of this thesis.

The motion of electrons with effective mass m_e^* under the influence of an electric field \vec{E} and a magnetic field \vec{B} is governed by the Lorentz equation. We add to this description a model of scattering under which scattering events occur after an average time interval τ , a model known as the relaxation-time approximation:

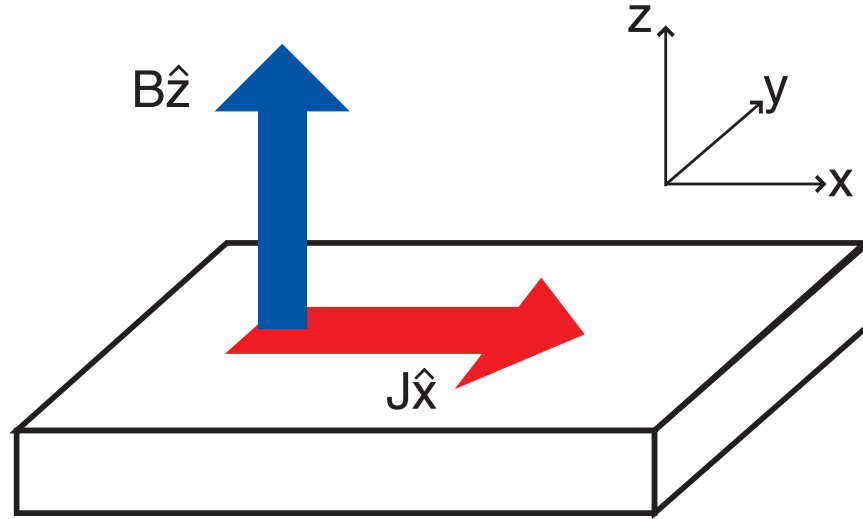


Figure 3.1: The experimental layout for a typical Hall effect measurement.

$$m \frac{d\vec{v}}{dt} = (-q)(\vec{E} + \vec{v} \times \vec{B}) - \vec{p}/\tau, \quad (3.1)$$

where v is the charge carrier velocity, q is the charge of the electron, and $\vec{p} = m\vec{v}$ is the momentum of the charge carriers. We can solve 3.1 in the steady state ($d\vec{v}/dt = 0$) for the geometry we describe above ($\vec{B} = B\hat{z}$, \vec{E} and \vec{J} confined to the x-y plane):

$$\begin{pmatrix} E_x \\ E_y \end{pmatrix} = \begin{pmatrix} \frac{-m_e^*}{q\tau} & -B \\ B & \frac{-m_e^*}{q\tau} \end{pmatrix} \cdot \begin{pmatrix} v_x \\ v_y \end{pmatrix}. \quad (3.2)$$

Considering the form of the current density

$$\vec{J} = (-q)n\vec{v}, \quad (3.3)$$

and that we will typically use it (rather than the electric field \vec{E}) as the dependent experimental variable, we rewrite equation 3.2, first multiplying both sides by the inverse of the

matrix on the right-hand side, and then substituting \vec{J} for \vec{v} using equation 3.3:

$$\begin{aligned} \begin{pmatrix} J_x \\ J_y \end{pmatrix} &= \frac{nq^2}{m_e^*} \begin{pmatrix} \frac{\tau}{1 + \omega_c^2 \tau^2} & -\frac{\omega_c \tau^2}{1 + \omega_c^2 \tau^2} \\ \frac{\omega_c \tau^2}{1 + \omega_c^2 \tau^2} & \frac{\tau}{1 + \omega_c^2 \tau^2} \end{pmatrix} \cdot \begin{pmatrix} E_x \\ E_y \end{pmatrix} \\ \begin{pmatrix} J_x \\ J_y \end{pmatrix} &= \begin{pmatrix} \sigma_{xx} & -\sigma_{xy} \\ \sigma_{xy} & \sigma_{xx} \end{pmatrix} \cdot \begin{pmatrix} E_x \\ E_y \end{pmatrix} \\ \vec{J} &= \boldsymbol{\sigma} \cdot \vec{E}, \end{aligned} \tag{3.4}$$

where $\omega_c = qB/m_e^*$ is the well-known cyclotron frequency, and the definitions of σ_{xx} and σ_{xy} should be apparent. Immediately following from equation 3.4 are natural limits for any galvanomagnetic measurement: a high and low field regime determined by whether $\omega_c \tau$ is significantly greater or less than one. When $\omega_c \tau \ll 1$, we are in the low-field regime, and electron scattering events occur much less frequently than the time for a cyclotron orbit; whereas when $\omega_c \tau \gg 1$, we reside in the high-field regime, and many cyclotron orbits occur before a electron scattering event. For a simple DC electric field in the \hat{x} direction, for which $B = 0$ (and thus $\omega_c = 0$), we obtain the familiar result:

$$J_x = q \left(\frac{q\tau}{m_e^*} \right) nE_x = q\mu nE_x, \tag{3.5}$$

with the familiar value for $\mu = q\tau/m_e^*$. Using this identification for μ , which is often an experimental parameter for which we can anticipate approximate values, we can create a quick guide as to whether our measurements will reside in the high- or low-field regime. The experimental apparatus used for measurements in this thesis is limited to fields of $B \leq 1$ Tesla, thus we can calculate

$$\omega_c \tau = \frac{qB}{m_e^*} \cdot \frac{m_e^* \mu}{q} = \mu B. \quad (3.6)$$

The samples studied in this thesis are crystalline or poly-crystalline silicon bearing chalcogen impurities of concentrations in excess of 10^{19} cm^{-3} ; their mobility will be $\mu \approx 100 \text{ cm}^2 / \text{V}\cdot\text{s}$ or less.² With fields limited to 1 Tesla, $\mu B \approx 10^{-2}$, and we reside firmly in the low-field limit. We will return to this point later.

Measurement of the Hall effect occurs under open-circuit conditions between the two extreme points along the y-axis (see Figure 3.1), thus we set the current $J_y = 0$ to obtain from equation 3.4:

$$\sigma_{xy} E_x + \sigma_{xx} E_y = 0, \quad (3.7)$$

and

$$J_x = \frac{1}{\sigma_{xx}} (\sigma_{xx}^2 + \sigma_{xy}^2) E_x. \quad (3.8)$$

We thus can use equations 3.7 and 3.8 to calculate the Hall coefficient:

$$R_H = \frac{E_y}{B J_x} = -\frac{\sigma_{xy}/B}{\sigma_{xx}^2 + \sigma_{xy}^2}. \quad (3.9)$$

Simple geometric concerns (*i.e.* $E_y = V_{Hall}/w$ and $I_e = wdJ_x$, where w and d are the width and depth of our sample respectively) and substitution of our expressions for σ_{xx} and σ_{xy} from equation 3.4 yields the result:

$$R_{Hall} = d \frac{V_{Hall}}{I_e B} = \frac{1}{qn}. \quad (3.10)$$

²Note that this means the mobility is $\mu \leq 10^{-2} \text{ m}^2/\text{V}\cdot\text{s}$ in SI units

This relatively simple result is the same as that often derived from more elementary considerations. The above treatment, however, neglected the thermal statistics of charge carriers: in general, there is not a single scattering time τ for all carriers. Instead, τ will depend on the energy of the scattered charge carrier and the mechanism by which it scatters (*e.g.*, acoustic phonons, ionized impurities, *etc.*). Thus, the elements of σ in equation 3.4 must be averaged over all electron states, weighted by the occupation, energy, and density of states for carriers at each energy. Treatment in this fashion, the most general of which would begin from the Boltzman transport equation, yields a slight adjustment to our above treatment for the low-field limit $\omega_c\tau \ll 1$:

$$V_{Hall} = r_H \frac{I_e B}{qdn}, \quad (3.11)$$

where r_H is the so-called Hall scattering factor:

$$r_H = \frac{\langle \tau^2 \rangle}{\langle \tau \rangle^2}. \quad (3.12)$$

The Hall scattering factor can be calculated analytically for many common scattering mechanisms. Perhaps more importantly, it can be measured. Careful inspection of equation 3.4 in the case of the high-field limit $\omega_c\tau \gg 1$ yields $r_H = 1$. In section 3.5, we will argue that even without being able to measure r_H we can proceed accurately.

3.3 The Hall effect and semiconductor statistics

In this section we review elements of semiconductor statistics that are of direct relevance to work in this thesis. The reader should refer to reference [114] for more detail.

3.3.1 Concentration of electrons in the conduction band

In general, we are concerned with calculating the electron concentration in the conduction band of silicon. In quite general terms, we can write this down as the product between the probability $f(E)$ that an electron occupies a state of energy E with the density of states $g(E)$, integrated over the energy of all states in the conduction band:

$$n = \int_{E_c}^{\infty} f(E) \cdot g(E) \cdot dE, \quad (3.13)$$

where E_c is the bottom of the conduction band, and we have set the upper limit of integration to ∞ . Strictly, we should integrate only over the energy range covered by the conduction band of silicon, but the upper limit of integration is unimportant provided it is above any occupied state. The integrand of equation 3.13 is composed of the occupation probability, $f(E)$, which has the form of the well-known Fermi function

$$f(E) = \frac{1}{1 + \exp\left(\frac{E - E_F}{k_b T}\right)}, \quad (3.14)$$

and the density of states $g(E)$, which we approximate near the bottom of the conduction band in silicon with the form

$$g(E) = 4\pi \left(\frac{2m_e^*}{h^2}\right)^{3/2} (E - E_c)^{1/2}. \quad (3.15)$$

where m_e^* is the effective mass of an electron near the conduction band minimum, h is Planck's constant, and E_c and E_F are the positions of the conduction band edge and Fermi level, respectively. Performing some elementary operations, we can write the integral of 3.13 as

$$n = 2 \left[\frac{2\pi m_e^* k_b T}{h^2} \right]^{3/2} \cdot 2\pi^{-1/2} \int_0^{\infty} \frac{\epsilon^{1/2} d\epsilon}{1 + \exp(\epsilon - \eta)}, \quad (3.16)$$

In equation 3.16 we have introduced the so-called reduced Fermi energy η , a dimensionless quantity that expresses the distance of the Fermi level from the conduction band edge as a multiple of the characteristic thermal energy k_bT :

$$\eta = \frac{E_F - E_c}{k_bT}. \quad (3.17)$$

We emphasize that $\eta < 0$ when the Fermi level is below the conduction band, and thus within the band gap. Also, we can rewrite equation 3.16 in a simple form by grouping the terms

$$\mathcal{F}_{1/2}(\eta) = 2\pi^{-1/2} \int_0^\infty \frac{\epsilon^{1/2} \cdot d\epsilon}{1 + \exp(\epsilon - \eta)}, \quad (3.18)$$

which is known as the Fermi-Dirac integral, and takes as an argument the reduced Fermi energy η ; and

$$N_c(T) = 2 \left[\frac{2\pi m_e^* k_b T}{h^2} \right]^{3/2} = 5.45 T^{3/2} \times 10^{15} \text{cm}^{-3} \cdot \text{K}^{-3/2}, \quad (3.19)$$

which is known as the band edge density of states, and has a value of about $3 \times 10^{19} \text{cm}^{-3}$ in silicon at room temperature. Using the substitutions of equation 3.18 and 3.19, the carrier concentration in the conduction band take the following simple form:

$$n(T, \eta) = N_c(T) \mathcal{F}_{1/2}(\eta). \quad (3.20)$$

In general, the Fermi-Dirac integral is one of a class of integrals $\mathcal{F}_j(\eta)$ defined by the subscript j . We will only have need of the $j = 1/2$ member of this family, and will drop the subscript for the remainder of this thesis. Further, we separate our analysis into systems that are *non-degenerate*, loosely defined as systems for which the dimensionless quantity η is several integers less than zero, and systems that are *degenerate*, which corresponds to any

system where this condition is not met. The term degenerate comes up frequently in the analysis of the carrier concentration, and in the context of semiconductor statistics, it simply refers to any instance in which η is close to or larger than 0. Historically, the term comes from the fact that the heat capacity of metals, governed by the limited number of electrons near the Fermi level that can participate in the absorption of heat, is much smaller than would be predicted classically. This phenomena was referred to as the “degeneration” of the heat capacity to small values. Thus, any context in which the Fermi level is near or within a partially filled band – and thus reduces the number of electrons that can participate in a particular phenomena relative to classical expectations – is considered degenerate.

However, returning to semiconductor statistics: in practice, the non-degenerate limit obtains when η is less than about -2 , in which case we do not lose much accuracy if we approximate $\mathcal{F}(\eta) = \exp(\eta)$. In this case, we can write our original equation for the carrier concentration simply as

$$n(T, \eta) = N_c(T)\exp(\eta). \quad (3.21)$$

Experimentally, we will often need to test for the condition of non-degeneracy when we have measured the carrier concentration over a particular temperature range. Referring to equation 3.20, we see that this amounts to determining whether the relationship

$$\frac{n(T)}{N_c(T)} \leq \mathcal{F}(\eta = -2) \approx 0.13, \quad (3.22)$$

is maintained over our measurement range. Such a determination is calmingly simple to make.

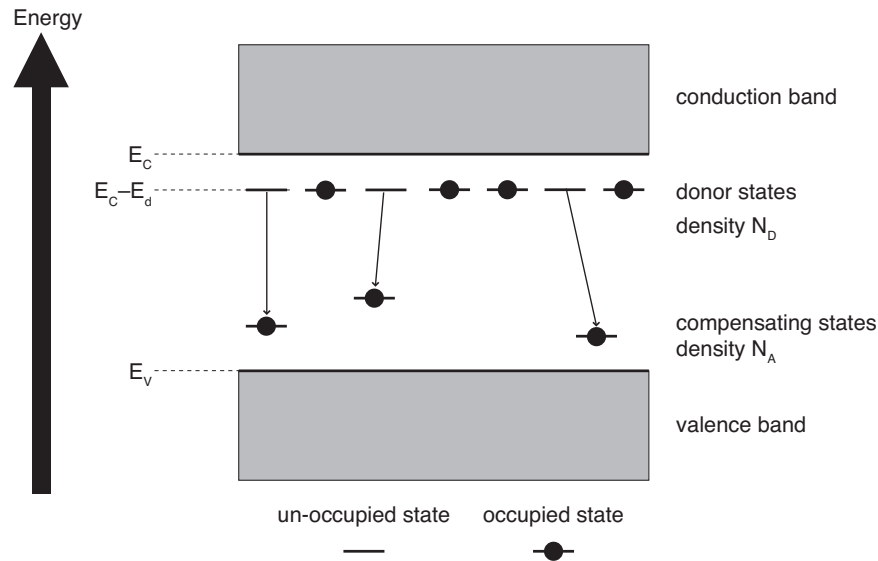


Figure 3.2: A schematic model of a donor-dominated semiconductor at $T = 0$ K. In this example, donors are characterized by a density N_d and a binding energy E_d . A much lower concentration N_a of compensating impurities introduce hole-like states to which donor electrons relax in all temperature ranges of interest.

3.3.2 Impurities and their excitations in a silicon lattice

Dopants are often added to silicon to alter its electrical and optical properties. Dopants that introduce excess electron states into the band gap, which through thermal ionization can be excited into the conduction band, are called donors. Alternatively, dopants that introduce hole-like states into the band gap, which through thermal excitation can be excited into the valence band, are called acceptors. When a donor (acceptor) state is occupied by an electron (hole), we consider it neutral; otherwise we consider it ionized. In addition to their density N_d , donor states are characterized by the energy E_d required to remove an electron from a neutral donor atom and place it in the conduction band with energy E_c . Acceptors are likewise characterized by their density N_a and the energy E_a required to remove a hole from a neutral acceptor atom and place it into the valence band with energy E_v .

In this thesis, we are generally interested in the case where $N_a \ll N_d$. In this case, even at $T = 0$ K, a portion of the donor state electrons will relax to the lower energy states available in the holes introduced by the acceptors, and a density N_a donor states will be empty. The ionization of donor states in this fashion is known as compensation. In this case, E_a is unimportant (indeed, compensation generally arises from a variety of states throughout the band gap), and the system is characterized by N_a , N_d , and E_d . Additionally, at finite temperatures, a portion of the remaining donors will be ionized through thermal excitation of the electrons to the conduction band.

The total occupation of the donor states can be expressed statistically as a function of the Fermi level E_F and the temperature T , but we must consider this problem carefully. In general, donor states have a level of spin degeneracy for which we must account. For example, a simple hydrogen-like donor can, in its ground state, host an electron of either spin up or spin down. We describe such a donor as having spin degeneracy $\beta = 2$. However, β can take on a variety of values depending of the details of the dopant, but will in general be on order 1. For a general donor state of spin degeneracy β , the ionized fraction will be:

$$\begin{aligned} N_d^+ &= \frac{N_d}{1 + \beta^{-1} \exp\left[\frac{E_F - E_C + E_d}{k_b T}\right]} \\ &= N_d [1 + \beta^{-1} \exp(\epsilon_d + \eta)]^{-1}, \end{aligned} \quad (3.23)$$

which can be derived from the statistical mechanics of fermions, and where we have re-introduced the reduced Fermi energy of equation 3.17, as well as the reduced binding energy $\epsilon_d = E_d/k_b T$.

Above, we derived equation 3.20 to be the the electron concentration in the conduction band. This equation is true regardless of whether we have doped a semiconductor or not, provided the approximation of a parabolic conduction band minimum is valid. For

a doped, compensated semiconductor, however, we can constrain the concentration of free electrons in the conduction band n to be equal to the concentration of ionized donors, minus the concentration of compensating impurities:

$$\begin{aligned}
 n(T, \eta) &= N_c(T) \mathcal{F}(\eta) \\
 &= N_d^+ - N_a \\
 &= N_d [1 + \beta^{-1} \exp(\epsilon_d + \eta)]^{-1} - N_a.
 \end{aligned} \tag{3.24}$$

There is a unique value of η that satisfies this equation for a particular value of T , N_a , N_d , E_d , and β . In general, this form of equation is not useful for us experimentally, though, as both T and η vary with temperature, and we do not immediately have knowledge of η . Without knowing η , we cannot fit equation 3.24 for the temperature independent (and material specific) quantities N_d , N_a , E_d , and β . We would prefer an equation of the form:

$$n \equiv n(T; N_d, N_a, E_d, \beta), \tag{3.25}$$

such that we can treat the temperature independent quantities as fitting parameters, and provided we have at least four (n, T) data points, solve for them. Generally we will collect many more data points, so as to over-constrain the problem. In the next section we describe how this is done.

3.3.3 Fitting for the energy of a donor electron state

Good approximations exist for $\mathcal{F}(\eta)$ even in the slightly degenerate regime: for $\eta \leq +1$, we can use approximations of the form

$$\mathcal{F}(\eta) = [C + \exp(-\eta)]^{-1}. \tag{3.26}$$

As we mentioned in equation 3.21, if $\eta \leq -2$, we can set $C = 0$ and $\mathcal{F}(\eta) \approx \exp(\eta)$ is an accurate approximation. For larger values of η , but still $\eta \leq 1$ we can use $C = 0.27$ without introducing an error of more than a percent or so [114]. Substituting 3.26 into equation 3.24, we can rearrange it as a quadratic in $\exp(\eta)$. Solving this equation yields the following solution for the Fermi level:

$$\exp(\eta) = \frac{2(N_d - N_a)}{[N_c - C(N_d - N_a) + \beta^{-1}N_a\exp(\epsilon_d)] + \left[[N_c - C(N_d - N_a) + \beta^{-1}N_a\exp(\epsilon_d)]^2 + 4\beta^{-1}(N_c + CN_a)(N_d - N_a)\exp(\epsilon_d) \right]^{1/2}}. \quad (3.27)$$

By simply inserting this equation into equation 3.20 we obtain for the carrier concentration:

$$n = \frac{2N_c(N_d - N_a)}{[N_c + C(N_d - N_a) + \beta^{-1}N_a\exp(\epsilon_d)] + \left[[N_c - C(N_d - N_a) + \beta^{-1}N_a\exp(\epsilon_d)]^2 + 4\beta^{-1}(N_c + CN_a)(N_d - N_a)\exp(\epsilon_d) \right]^{1/2}}. \quad (3.28)$$

As we have previously discussed, when the system is comfortably non-degenerate ($\eta \leq -2$), we set $C = 0$ and equation 3.28 becomes

$$n = \frac{2(N_d - N_a)}{\left[1 + \frac{N_a}{\beta N_c} \exp(\epsilon_d) \right] + \sqrt{\left[1 + \frac{N_a}{\beta N_c} \exp(\epsilon_d) \right]^2 + \frac{4}{\beta N_c} (N_d - N_a) \exp(\epsilon_d)}}, \quad (3.29)$$

and the Fermi level is given simply using equation 3.21:

$$E_c - E_F = k_b T \exp(n/N_c). \quad (3.30)$$

The equations 3.28 and 3.29 are precisely of the form we sought ($n \equiv n(T; N_d, N_a, E_d, \beta)$). The only temperature-dependent parameter on the right hand side is the temperature itself, which enters through N_c and $\epsilon_d = E_d/k_b T$. Thus, given a set of measurements of n as a function of T , we can find the best fit values for N_d , N_a , E_d , and β in a least squares sense using any numerical technique that suits us.

3.3.4 Developing statistical intuition

Limiting behaviors of the carrier concentration

There are several limiting cases and simple examples that we will be well-served to consider. First, we consider the behavior of the carrier concentration as a function of temperature, via equation 3.29. We briefly consider three limits. First, when $\epsilon_d \rightarrow 0$ ($k_b T \gg E_d$), the denominator is equal to 2, and the carrier concentration becomes

$$n(T) = N_d - N_a, \quad (3.31)$$

which represents the expected result that, at high enough temperatures, all donors are ionized; the carrier concentration is thus equal to the donor concentration minus the concentration of any compensating impurities. As we cool the sample down, n will eventually begin to decrease as donor states begin to freeze out. If the degree of compensation is small, such that it is possible for $N_a \ll n \ll N_d$, we can approximate equation 3.29 as:

$$n(T) \approx \sqrt{\beta N_c N_d} \exp\left(-\frac{E_d}{2k_b T}\right). \quad (3.32)$$

In this regime, a plot of $\log(n)$ versus $1/T$ will exhibit a slope of $E_d/2$. We refer to this temperature regime, if the degree of compensation is small enough for it to exist, as the *donor-dominated freeze-out* regime. If we continue cooling, we will eventually reach the *compensation-dominated freeze-out* regime, for which — when we examine 3.29 in the limit that $n \ll N_a \ll N_d$ — we can write:

$$n(T) \approx \beta N_c \frac{N_d - N_a}{N_a} \exp\left(-\frac{E_d}{k_b T}\right). \quad (3.33)$$

In the compensation-dominated freeze-out regime, a plot of $\log(n)$ versus $1/T$ will exhibit a slope of E_d . We have shown these regimes schematically in Figure 3.3. Provided we are studying a sample in non-degenerate conditions, consideration of these limits often gives us a starting point for a fit or insight into the value of the binding energy E_d .

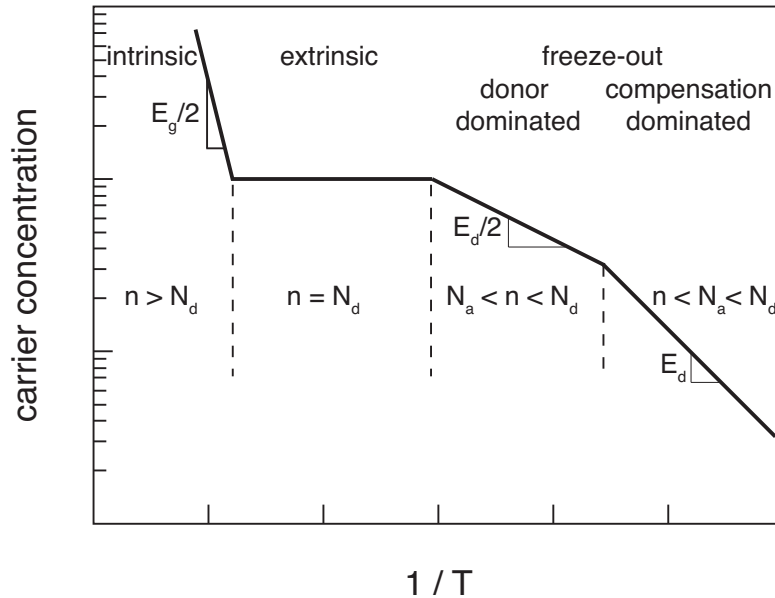


Figure 3.3: Typical ionization of a monovalent impurity in silicon. In addition to the regimes discussed in the text, we also show the *intrinsic* regime, in which excitation of electrons from the valence band to the conduction band dominates the behavior of $n(T)$. This regime has a significantly steeper slope in this plot, equal to half the band gap of the material.

Behavior of the Fermi level

We will often find it useful to speculate intelligently on the effect that changing the value of N_d and E_d has on the position of the Fermi level E_F . In an extrinsic semiconductor, the Fermi level is fixed by the constraint of equation 3.24. If we consider only cases that are not more than mildly degenerate ($\eta \leq 1$), we can make use of the approximation of equation 3.26 with $C = 0.27$, and arrange equation 3.24 in a dimensionless form:

$$\frac{1}{0.27 + \exp(-\eta)} = \frac{N_d/N_c}{1 + \beta^{-1}\exp(\epsilon_d + \eta)} - \frac{N_a}{N_c}. \quad (3.34)$$

For clarity we have not written explicitly N_c 's dependence on temperature, and we remind the reader that $\eta = (E_F - E_c)/k_bT$ and $\epsilon_d = E_d/k_bT$. We first consider the form of both sides, noting that the left-hand side (LHS) is a monotonically increasing function of E_F , while the right-hand side (RHS) is a monotonically decreasing function of E_F . This observation indicates, provided N_d , E_d , and N_a take experimentally reasonable values, the two functions will have to intersect at some value of E_F . The value of E_F at intersection is then the value that satisfies equation 3.34, and the value of E_F in our system.

We can consider the solution of this equation graphically, plotting both the left- and right-hand sides as a function of the value of the Fermi level E_F . The value for which the two curves intersect is the solution to the equation, and the value of the Fermi level in our system. We consider a system at $T = 300$ K, with a compensation fraction $N_a/N_d = .001$, a value representative of most of the samples we will study in this thesis.

In the top portion of Figure 3.4, we see the effect that changing the concentration of donors (N_d) has on our system. Because N_d does not effect the *fraction* of ionized donors at a particular value of temperature and Fermi level, a change of N_d simply shifts vertically the curve reflecting the RHS of equation 3.34. This shift forces the the Fermi level that

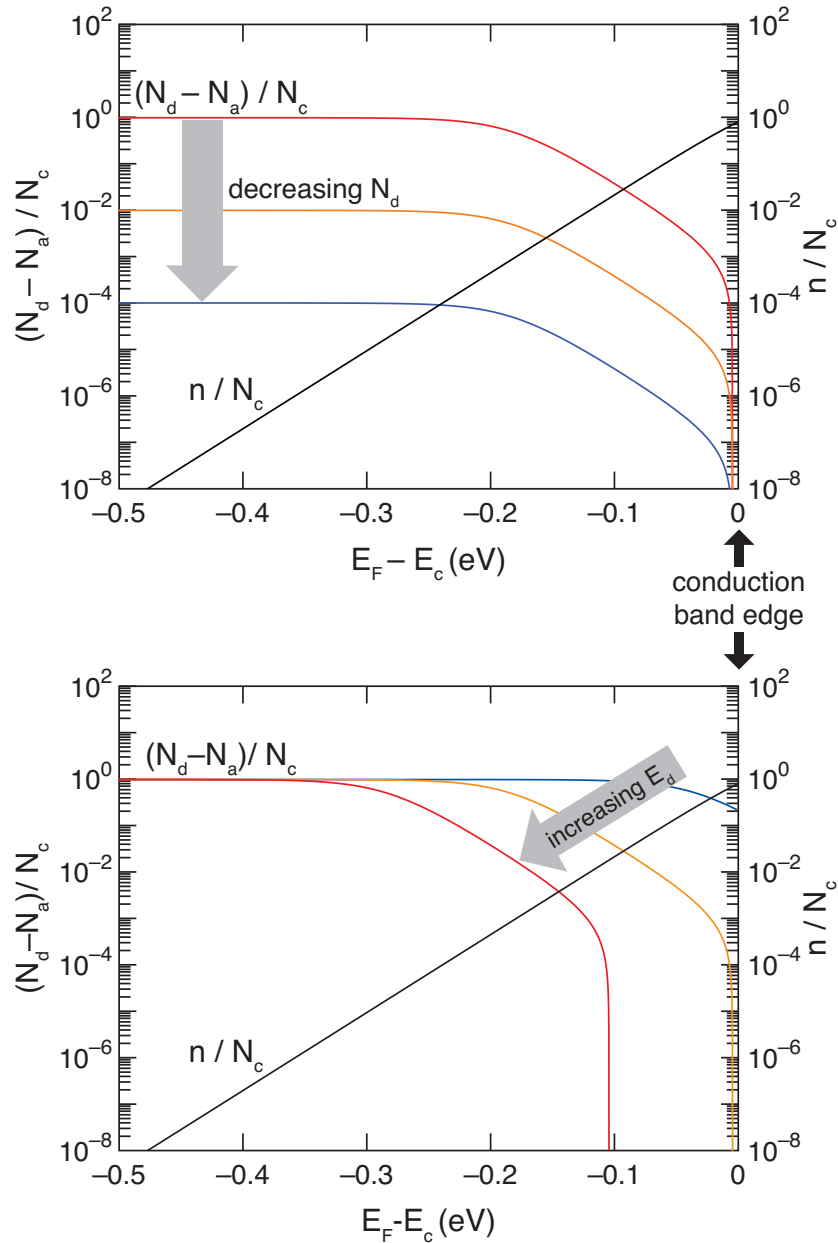


Figure 3.4: Graphical techniques for finding the Fermi level. The value of E_F corresponds to the solution of equation 3.34, which we find graphically as the point of intersection between the two sides of the equation. For this plot, we use $T = 300$ K, $\beta = 2$, and $N_a/N_d = 10^{-3}$; at this temperature $N_c = 3 \times 10^{19} \text{ cm}^{-3}$. *Top:* Decreasing the doping concentration N_d will always shift the location of intersection (and thus the value of E_F) lower in the band gap. In this plot, $E_d = 0.2$. *Bottom:* Increasing E_d will also shift E_F deeper into the gap to move the Fermi function out of the conduction band, due to fewer conduction band electrons. We plot values of $E_d = [0.05, 0.2, 0.3]$ eV.

satisfies equation 3.34 to assume a lower value. Physically this accounts for the fact that fewer donors will decrease the number of electrons in the conduction band at a particular value of E_F . Thus, the Fermi level must decrease to move the Fermi function out of the conduction band, and thus decrease the number of free electrons in our system.

In the bottom portion of Figure 3.4, we can see graphically the effect that changing the value of the binding energy E_d of a donor electron has on the position of the Fermi level. At a given temperature and donor concentration, increasing E_d moves the location of the Fermi level deeper into the band gap. Physically, we know that a larger binding lead to a lower fraction of ionized impurities at a given temperature; while simultaneously, the Fermi function will sweep through deeper donor states at lower values of E_F , emptying them and forcing the electrons into the conduction band. These two facts together prove to us that the Fermi level must, therefore, shift to lower energies with an increase in the value of E_d . We also see that at dopant concentrations comparable to N_c , especially for deep-lying donor states such as $E_d = 0.3$ eV, that the Fermi level sits fairly far above the level of the donor state. This observation — necessary to account for the significant occupation of these deep states at such high concentration — will be of use to us in Chapters 5 and 6.

3.4 Impurity bands

The above discussion implicitly assumes that the dopant electrons can be considered to be isolated impurities with identical ionization energies E_d , the value of which is characteristic of the structure and species of the dopant. Indeed, in chapter 6 we will exploit this fact to identify a particular state of sulfur present in our samples. The assumption is mathematically evident in equation 3.23, in which we enforce on the dopant states the condition that they all reside at the same energy level. Provided the dopants are spaced far

apart relative to the Bohr radius of the bound dopant electrons, the Fermi level and electron concentration will behave as we have discussed. However, at high concentrations, this is no longer an accurate description. Researchers recognized very early in the investigation of doped semiconductors that large concentrations of impurities led to a decrease in the apparent donor energy [32, 33].³

A primary reason for decreased thermal ionization energies relates to electron-electron interactions that shield the Coulomb field between a parent donor and its electron. As the dopant-to-dopant spacing — which for a dopant concentration N_d is approximately $N_d^{-1/3}$ — approaches the Bohr radius a_H^* of the dopant atom, this type of interaction becomes increasingly important. The original premise for a metal-insulator transition, suggested by Mott [17, 19], was that when the product

$$N_d^{1/3} a_H^* \approx C, \quad (3.35)$$

where C is a constant of order unity, a semiconductor would transition to a metal with finite conductivity even at $T = 0$. Somewhat later, Edwards and Sienko found that the value $C = 0.26$ is almost universally true [22, 124]. The field of metal-insulator transitions is quite broad, and extends to many materials other than doped semiconductors. There is a sizable body of literature, however, dealing with the transition in silicon, due to the ready availability of high-quality and well-characterized samples that can be easily doped to well-known, uniform concentrations [20, 28, 119]. We summarize some of these data in Table 3.1. The important observation for our purposes is that we can use equation 3.35 to predict the critical concentration for a transition to metallic conduction, provided we know the Bohr radius. The Bohr radius can be approximated using the binding energy of a particular

³Interestingly, this does not cause a corresponding shift in the optical absorption spectrum of the impurities [122], an interesting piece of physics related to an effect known as the Franck-Condon shift [123].

dopant using the simple Bohr model,

$$a_H^* = \frac{1}{4\pi\epsilon_0} \frac{q^2}{2\epsilon_r E_d}, \quad (3.36)$$

where $\epsilon_r = 11.9$ is the relative permittivity of silicon, and ϵ_0 is the permittivity of free space. Table 3.1 shows that calculations of this sort, using measured ionization energies, generate results in rough agreement with the experimentally determined critical densities n_{crit} at the metal-insulator transition 3.35.

Sulfur and other deep-states in silicon rarely appear in the literature of metal-insulator transitions, although this is beginning to change due to interest in the impurity-band photovoltaic effect [13]. This omission is not surprising, as their low solubility in silicon means that it is often impossible — using conventional doping techniques — to reach the high concentrations necessary for a metal-insulator transition. This thesis, of course,

Material	E_d (meV)	a_H^* (nm)	n_{crit}^{calc} (10^{18} cm^{-3})	n_{crit}^{exp} (10^{18} cm^{-3})
Si:P	45	1.34	7.3	3.5
Si:As	53.7	1.13	12.3	5
Ge:Sb	10.3	5.87	0.09	0.01
Ge:As	14.2	4.26	0.23	0.4
Ge:P	12.9	4.69	0.17	0.3
Si:S (1)	110	0.55	105	?
Si:S (2)	300	0.20	2100	?

Table 3.1: A comparison of calculations of the critical concentration of dopants necessary for a transition to metallic conduction by assuming a simple relationship between the binding energy E_d and the Bohr radius a_h^* . Better estimates can be acquired if the details of the wavefunction of the impurity electron are considered when assigning a value to a_h^* . For deep states such as sulfur, we consider two representative states, but are likely underestimating the Bohr radius (and overestimating the n_{crit}). Experimental values of n_{crit} are from reference [20] and [21]. Values of E_d are from Table 19.2 of reference [125].

deals with materials that bypass this obstacle using non-equilibrium doping techniques. We will seek signs of metal-insulator transitions in chapters 5 and 6, including increases in mobility with with increased dopant concentration, finite low-temperature conductivity, and insensitivity of carrier concentration to temperature [119].

3.5 Neglect of the Hall scattering factor

As we mentioned above, the specifics of our experiment will not permit access to the high-field limit, thus the Hall scattering factor r_H will remain unknown. Ignorance of r_H is not unusual in Hall effect measurements. In well-known materials, when large magnetic fields are available, r_H can generally be measured. However, in the characterization of new materials, it is frequently impractical to measure r_H and it is neglected. Although neglecting r_H introduces absolute errors into our calculation of n and μ , it will not affect analyses in which the primary scattering mechanism does not change over the temperature range of interest.

The primary concern when the value of r_H is unknown is twofold: first, an error of potentially 50% is introduced into the value of carrier concentration n and mobility μ . Such an error is not of major concern to us, as detailed analysis will deal with the slope of $\text{Log}(n)$ versus $1/T$. An error that is constant with temperature will provide a vertical shift of these curves, but not effect an analysis interested in slope. The second concern, however, is that r_H may change value with temperature. Such behavior has been demonstrated to cause potential errors in the fitting of temperature dependent Hall data in GaAs [112]. However, the Hall scattering factor has been measured to be $r_H \approx 1$ for heavily doped silicon [126] such as the samples we will study. Perhaps most importantly, the only experiment where these adjustments are directly relevant in this thesis is in the fitting of section 6.4.2. Similar fitting

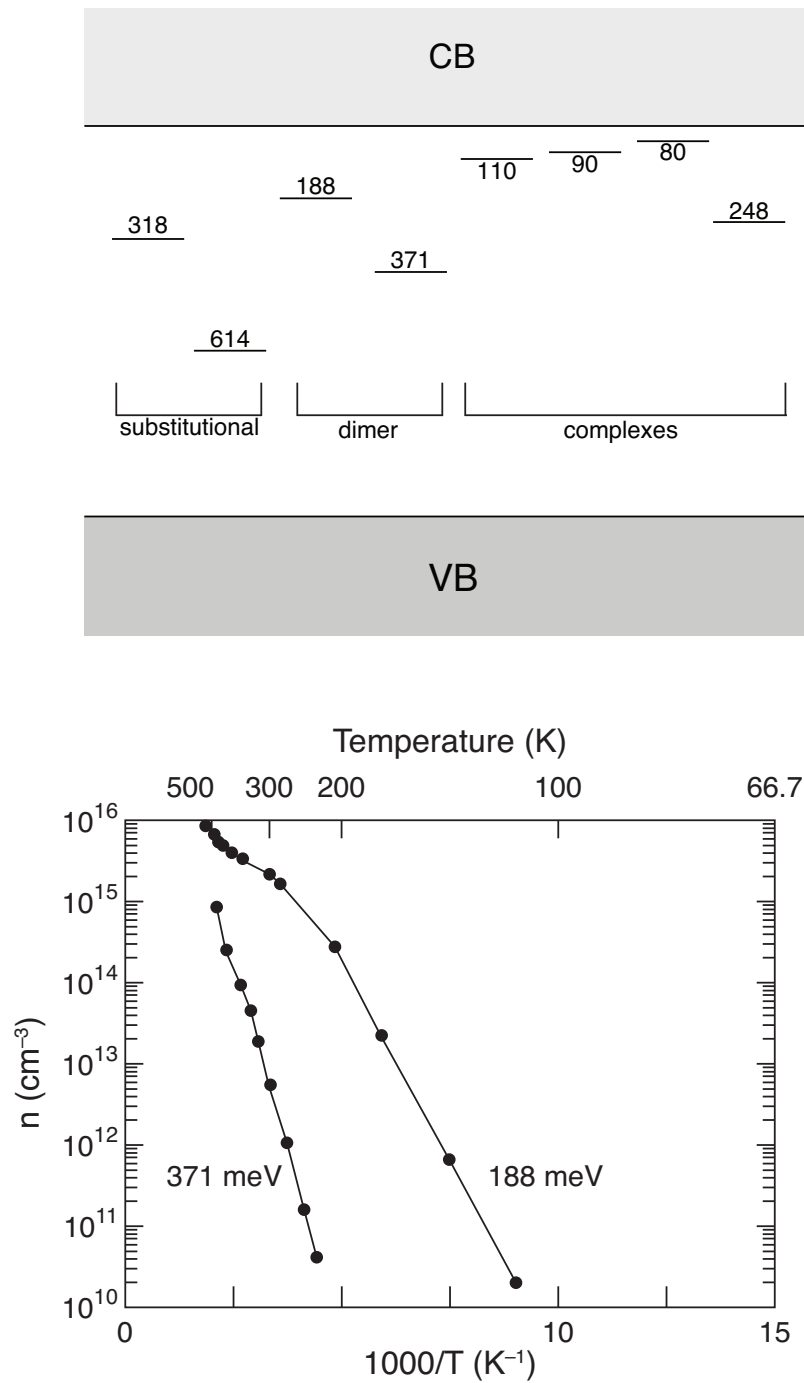


Figure 3.5: Equilibrium sulfur donors in silicon. *Top*: Donor states of sulfur in silicon [129]; energies given as meV below the conduction band edge. When known, the structure is given below; for the substitutional and dimer states, the two levels correspond to single and double ionization of the state. *Bottom*: Temperature-dependent Hall effect measurements of the dimer state as originally reported by Carlson and Hall; adapted from [38].

has been carried out for sulfur donor states previously [38,127,128] using the approximation $r_H = 1$, and these experiments yielded very good agreement with the donor binding energies found via other means. So although we do not expect ignorance of the Hall scattering factor to affect our conclusions, it is prudent to keep it in mind, and we hope the discussion has been helpful to some readers.

3.6 The Hall effect and deep sulfur impurities

Sulfur is often considered to be a deep-level impurity in silicon because many of the electron states it introduces (see Figure 3.5) are deeper than 100 meV below the conduction band edge. In cases where the electrical properties are dominated by deep levels, Hall effect measurements can be used to find the binding energy E_d of the sulfur atoms. By comparing with literature data [129,130], it is possible to identify the particular arrangement of sulfur in the silicon lattice that leads to observed behavior. The first estimates of the energetics of the electron states introduced by sulfur were probed using Hall measurements [38].⁴ We reproduce these results in Figure 3.5 to give the reader a sense of the temperature-dependence that such states introduce into transport quantities such as the carrier concentration.

⁴Interestingly, these studies were published by Hall himself.

Chapter 4

Doping silicon beyond equilibrium using a single femtosecond laser pulse

4.1 Chapter abstract

Doping silicon beyond the equilibrium solubility with chalcogens (S, Se, Te) via femtosecond laser irradiation yields remarkable optical properties that are not well understood, such as absorption of photons with energy less than the band gap. We present the first detailed structural and electronic characterization of silicon doped in this manner by studying the result of irradiation with a single femtosecond laser pulse while in an SF₆ environment. We determine that a single laser pulse is capable of implanting a sulfur dose of approximately $(4 \pm 1) \times 10^{13} \text{ cm}^{-2}$ into silicon. The sulfur concentration is nearly 10^{20} cm^{-3} at the surface, remains above 10^{19} cm^{-3} for the first 10 nm, and falls off to our detection limit of $< 10^{17} \text{ cm}^{-3}$ at a depth of 40 – 60 nm. We determine a minimum fluence

between 1.75 and 2 kJ/m² is necessary for implantation, which likely corresponds to the melting threshold of silicon for our experimental conditions. Increasing the fluence has no measurable impact on sulfur concentration, although higher fluences do create a steeper concentration gradient. The sign of the Hall coefficient is negative after irradiation, and we demonstrate the fabrication of a rectifying p-n junction using single laser-pulse doping. Cross-sectional transmission electron microscopy images reveal an amorphous layer near the surface immediately after irradiation. This study yields important information regarding silicon doped with fs-lasers, and offers some insight into non-equilibrium doping of silicon in general. The technique has potential applications as a direct-write doping method for semiconductors.

4.2 Introduction

We have previously reported on a laser-based technique for doping silicon with chalcogens to non-equilibrium levels [53, 66, 68]. By irradiating a silicon wafer with a series of intense, ultrashort ($\tau < 100$ fs) laser pulses in the presence of a solid or gaseous impurity, we implant the impurity into the silicon at concentrations greater than 10^{20} cm⁻³; for chalcogens, this concentration is 3–4 orders of magnitude greater than the solid solubility limit. In addition, when the dopant is chosen from among the heavy chalcogens (S, Se, Te), the resulting doped silicon exhibits remarkable optoelectronic properties, such as strong absorption of photons with energy as low as $E = 0.5$ eV; this value is substantially less than the band gap of silicon ($E_g = 1.1$ eV) [65]. We have also demonstrated that the absorbed sub-band gap photons can generate a photocurrent for photon energies as low as $E = 0.8$ eV [71], suggesting the creation of mobile electron-hole pairs and the potential presence of an impurity band in the energy gap of silicon. Although we have made some

progress in understanding how the system returns to an equilibrium state via diffusion of the dopants during thermal annealing [70], the fundamental processes that govern inclusion of the dopant into the silicon lattice remain unexplored.

Other researchers have reported similar doping concentrations and optical properties [49] in silicon using other techniques, such as ion implantation with high doses followed by crystal regrowth via pulsed laser melting [43]. A great deal of interest has been generated, as well, from proposals that at high concentrations, deep-level impurities in silicon may lead to the formation of an impurity band that could be used for increased photovoltaic efficiencies [12,13]. Additionally, the use of ns and ps lasers for doping has also been explored before [76]. Because fs-second laser doping of silicon has already demonstrated remarkably different results than these other techniques, it is important to understand the structural and electronic properties of silicon doped in this fashion. Such knowledge will shed light on a fascinating non-equilibrium physical phenomena, as well as potentially enable further application of the technique. To our knowledge, there has been no published work regarding such structural and electronic details of doping with ultrashort laser pulses.

Detailed descriptions of our previous work have been summarized elsewhere, [55,63,72], and we review it only briefly to motivate the experiments described herein. By rastering a train of amplified femtosecond laser pulses (pulse length $\tau < 100$ fs, center wavelength $\lambda = 800$ nm, fluence > 4 kJ/m²) across the surface of a silicon wafer in the presence of a gaseous sulfur-containing compound (typically SF₆), we create a polycrystalline layer extending about 100 nm into the substrate. The polycrystalline region is doped with sulfur beyond the equilibrium solubility limit to about 10²⁰ cm⁻³; the equilibrium solubility of sulfur in silicon is about 10¹⁶ cm⁻³ [37,38]. In general, the femtosecond laser pulses alter the morphology of the substrate, creating a quasi-periodic array of bumps or spikes, whose geometry is affected by laser parameters and the ambient environment [53,66,69]. The development of a highly

roughened surface is a result of repeated melting, ablation, and resolidification of the silicon, and is a phenomena that has been described in detail [54–56, 58]. The morphology has several interesting applications [61, 62]. However, it presents many challenges for properly characterizing fs-laser doped silicon, and as we will describe in a later chapter, it is not necessary for the interesting sub-band gap optical properties.

In our previously reported work, we exposed every location on the silicon surface to a plurality of laser pulses above the ablation threshold. As we have mentioned, such treatment – in addition to doping the silicon – results in the development of a complex, quasi-periodic surface structure. Not only does this surface morphology present difficulties in quantifying the concentration and distribution of dopants, it also makes it impossible to determine which stage of laser irradiation is responsible for doping of the silicon substrate. For example, doping could occur as a result of the initial melting of the flat surface layer, or a subsequent melting of more complex morphology. Also, because surface morphology has the effect of preferentially focusing the laser beam away from areas of high slope, rough surfaces create local fluence variations that are not measurable. The determination of the threshold fluence, or the fluence-dependence of laser doping, is thus difficult. Such information is crucial to understand the dynamics of the laser-doping process.

This chapter addresses these problems, and reports a thorough investigation of irradiating a silicon surface with a single femtosecond laser pulse while in an SF₆ ambient environment. We find a laser fluence threshold for inclusion of the sulfur dopant, and that increasing beyond that threshold does not increase the total sulfur dose. Hall measurements show that the irradiated surface exhibits a significant change in the Hall coefficient, potentially from sulfur electron donors. The Hall coefficient is also independent of incident fluence above the threshold for doping, just as total dose is. Carrier mobility is not substantially degraded from that of the original crystalline substrate. We also demonstrate the

rectifying properties of the junction between a laser-doped region and a silicon substrate. We conclude with a discussion of what we can learn from these data regarding the dynamics of ultrashort-pulse laser doping.

4.3 Experimental setup

Except as noted, our sample preparation is as follows. We prepare a (100) silicon wafer (boron doped, $\rho = 1 - 20 \text{ } \Omega\cdot\text{cm}$) using the standard RCA clean [104]. Following the clean, we strip the native oxide in a dilute (5%) HF solution, and immediately transfer the wafer to a vacuum chamber. The chamber is evacuated to high vacuum ($p < 10^{-4}$ Pa), and subsequently backfilled with 6.7×10^4 Pa of SF₆ gas. The wafer is placed in front of the focus of an amplified femtosecond laser pulse, oriented with the wafer surface perpendicular to the laser beam. The laser pulses are produced by a regeneratively amplified titanium:sapphire femtosecond laser system with an average pulse energy of 2.5 mJ, center wavelength of 800 nm, and pulse duration 75 fs. We measure the spatial profile at the sample surface by deflecting the beam into a CCD camera, and calculate laser pulse fluence by dividing pulse energy by the area of the pulse (defined as the area of the pulse with intensity greater than $1/e$ of the maximum). The full-width at half-maximum of the laser spot was $700 \pm 10 \text{ } \mu\text{m}$. We manually trigger the laser cavity optics to produce a single laser pulse with fluence between 2 and 4 kJ/m². In some experiments described below, we study the effect of changing the laser fluence or number of laser pulses. Where this is the case, we note it below.

Following irradiation, secondary ion mass spectroscopy (SIMS) was performed to measure the dopant profile as a function of distance from the surface. For SIMS measurements, samples were prepared in the above-described fashion using single pulses of fluence

1.75, 2, 3, and 4 kJ/m². Also, for samples irradiated with a fluence of 2 kJ/m², we thermally anneal a sample at 775 K for 30 minutes prior to measurement to determine the extent, if any, of dopant redistribution with thermal treatment. The SIMS signal was collected from a square region 15 μm \times 15 μm near the center of the irradiated region, using a 7 keV Cs ion beam; an ion beam current between 10 – 200 nA was used depending on measurement conditions. Because the most abundant isotopes of oxygen and sulfur have atomic weights of 16 and 32, respectively, there is potential ambiguity over which species we are counting when we monitor the atomic mass 32 signal (assuming singly ionized masses are being measured). To ensure we are measuring sulfur, we pre-etch the native oxide using a low current exposure to the ion beam for 15 s; we also monitor the ratio of atomic mass 32 to 34 coming from the sample. By comparing the ratio of these signals to known values for sulfur’s isotopic abundance ($^{32}\text{S} : ^{34}\text{S} \approx 22$), we ensure that we are measuring sulfur rather than oxygen in the SIMS signal. Count profiles are calibrated against a known ion implanted sample to generate concentration versus depth. Additionally, by comparing discrepancies between low- and high-count data obtained from the calibration samples, we corrected for non-linear detector errors (*N.B.*, see acknowledgements)

We probe the electronic nature of the sulfur-implanted silicon using Hall effect measurements. To isolate the doped layer, silicon-on-insulator (SOI) wafers are used, with a device layer thickness of 220 nm that was lightly n-doped. The samples are prepared and exposed as described above. Subsequently, we mask a 100 μm \times 100 μm area at the center of the laser-irradiated areas using standard positive photolithography. The surrounding silicon area is etched down to the buried oxide using a reactive ion etch. Using another positive photoresist mask, we remove the native oxide using a dilute HF (5%) solution and thermally evaporate Ti/Ni/Ag contacts (20/20/500 nm) on each of the four corners of the mesa in a van der Pauw geometry [115]. The contacts extend no farther than 5 μm from

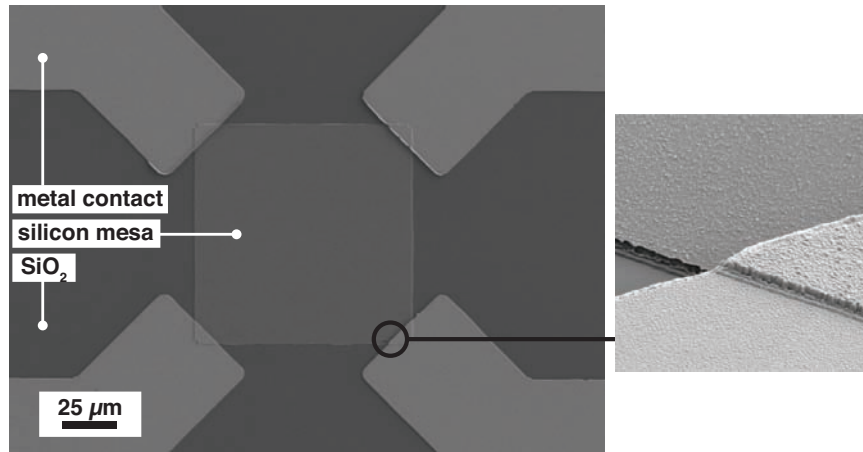


Figure 4.1: Our device geometry for probing the transport properties of the as-implanted silicon layer

each corner, so as to minimize errors in the resistivity and Hall measurements [117]. Using standard measurement procedures [109], we excite the samples with a current of less than 500 nA for both resistivity and Hall measurements, and immerse them in a magnetic field of 0.75 T for the Hall measurement.

We also probe the electronic properties of the junction between the laser-doped region and the substrate, which requires a slight variation to the above-described sample preparation. After the RCA clean, we grow a layer of thermal oxide (thickness 150 nm) atop the silicon wafer, and deposit a layer of Al (thickness 1 μm) on top of the oxide using an electron beam evaporator. Using standard positive photoresists, square openings (dimensions: 100 μm \times 100 μm) are defined, and we subsequently etch the exposed area of the Al layer with a commercial Al etch (nitric/phosphoric/acetic acid mix), and we then etch the newly exposed SiO_2 layer with buffered oxide etch (BOE 5:1 40% NH_4F :49% HF); the remaining photoresist is then removed. The samples are then transferred into a vacuum chamber and we proceed as described above, taking care to expose only the square openings to a single laser pulse. Following laser irradiation, the aluminum layer – which reflects the

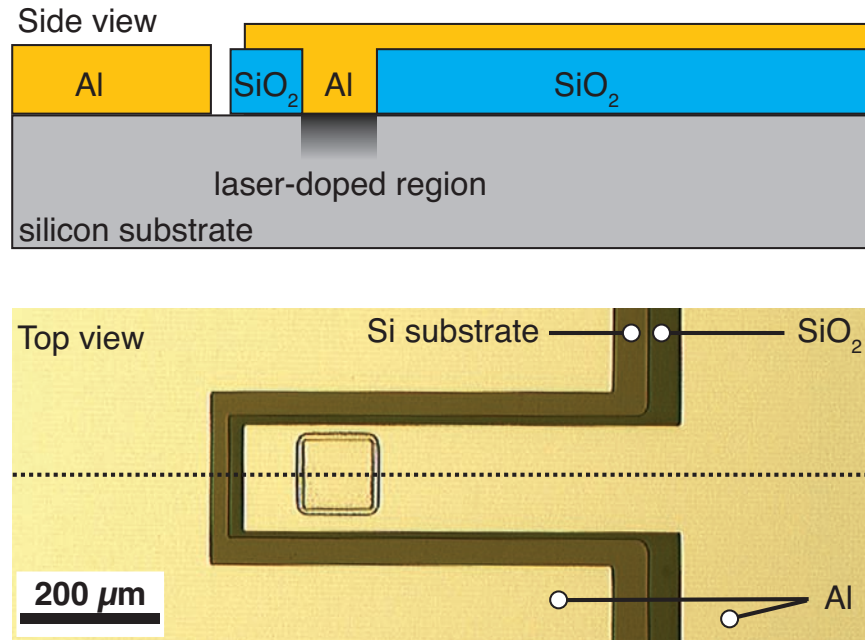


Figure 4.2: Our device geometry for probing the electronic properties of the junction between the laser-doped region and a p-type silicon substrate. *Top*: A cross-sectional view of the device cut along the dotted line in the bottom image. *Bottom*: Overhead optical microscope image of our device geometry.

laser pulse from all areas except the $100 \mu\text{m} \times 100 \mu\text{m}$ opening – is etched away. The remaining oxide is then also etched away (5:1 BOE) from all regions except a narrow strip extending from the laser-exposed area; this strip of oxide provides the insulation necessary to make electrically isolated contact to both the substrate and the laser-doped region (see Figure 4.2). Using a photoresist mask, we remove the native oxide (from the areas we intend to contact) using a dilute HF etch (5%), and electron beam evaporate Al (250 nm) in a geometry suitable for measuring the electronic properties of the junction between the laser-doped region and the substrate (see Figure 4.2). We prepare samples exposed to a single laser pulse of 4 kJ/m^2 laser fluence; and also thermally anneal the some samples before depositing metal contacts. In these cases, thermal anneals are performed in an open-tube furnace with a flow (280 sccm) of forming gas mixture (95 % He, 5% H_2). When testing the

current-voltage ($I - V$) relationship of the junction between the laser-doped region and the substrate, we apply a voltage (over a range of $\pm 1V$) between the substrate contact and the laser-doped region contact and measure the resulting current. Anticipating the p-n junction behavior that we observe, we define as positive a voltage that raises the potential of the substrate contact above that of the laser-doped region contact.

4.4 Results

In the top of Figure 4.3, we plot the sulfur concentration profile as a function of distance from the surface for various fluences. We observe a noticeably deeper implant depth for lower fluences. In the bottom portion of Figure 4.3, we show the total sulfur dose implanted by the laser process, obtained by integrating the concentration profiles of Figure 4.3. The shaded grey area of the figure indicates the limit of our detection; this limit is set by a small amount of oxygen contamination that is sometimes present as a native oxide after our pre-measurement etch. In the figure we observe that fluences of 1.5 and 1.75 kJ/m² are not statistically different from background; while fluences of 2 kJ/m² and larger have sulfur doses an order of magnitude above this background level. However, despite differences in the shape of the sulfur concentration profile, there is no statistically significant differences in total sulfur dose among these samples.

Table 4.1 shows the Hall coefficient, sheet carrier concentration, and Hall mobility for samples irradiated with 3 and 4 kJ/m², as well as a control sample. To calculate sheet carrier concentration from the Hall voltage, we neglect the effect of the Hall scattering factor for reasons we discussed in section 3.2 and use the relationship:

$$n_s = \frac{IB}{qV_{Hall}}. \quad (4.1)$$

Samples with irradiated with fluences less than 3 kJ/m^2 did not provide sufficient optical contrast to perform the photolithography necessary to isolate and contact the sample, so data is not available for those samples. The Hall coefficient changes by four orders of magnitude with laser irradiation, with a sheet carrier density equal to approximately 1% of sulfur dopants for both 3 and 4 kJ/m^2 samples.

In Figure 4.4, we show the current-voltage relationship of the junction between the laser-doped region and the substrate. In addition, we show the $I - V$ relationship for laser-doped samples after thermal annealing. We observe rectifying behavior of the expected polarity for a p-n junction, although only in samples that have been annealed to 975 K.

4.5 Discussion

Of the unanswered questions regarding fs-laser doped silicon, perhaps the most fundamental regards the mechanism of inclusion of the dopant. Specifically, when doping with sulfur from a gaseous SF_6 ambient environment prior to this work, we have been unable to determine which laser-induced process initiated the dopant inclusion. Because our previous work employed the use of a plurality of pulses above the ablation threshold, surface texture developed over the course of doping. This surface texture preferentially focuses light away from areas of high slope, making the actual distribution of laser fluence

Laser Fluence (kJ/m^2)	Sulfur dose ($\times 10^{13} \text{ cm}^{-2}$)	Sheet carrier concentration ($\times 10^{11} \text{ cm}^{-2}$)	Hall mobility ($\text{cm}^2/\text{V} \cdot \text{s}$)	Carrier-to-donor ratio
control	n/a	-1.7×10^{-4}	1450	n/a
3	5 ± 1	-3.0	830	0.006
4	3 ± 1	-3.1	690	.01

Table 4.1: Results of Hall and resistivity measurements on silicon doped with sulfur via a single laser pulse. The 2 kJ/m^2 sample could not be measured because it lacked sufficient optical contrast to align the photomasks for feature isolation and contact deposition

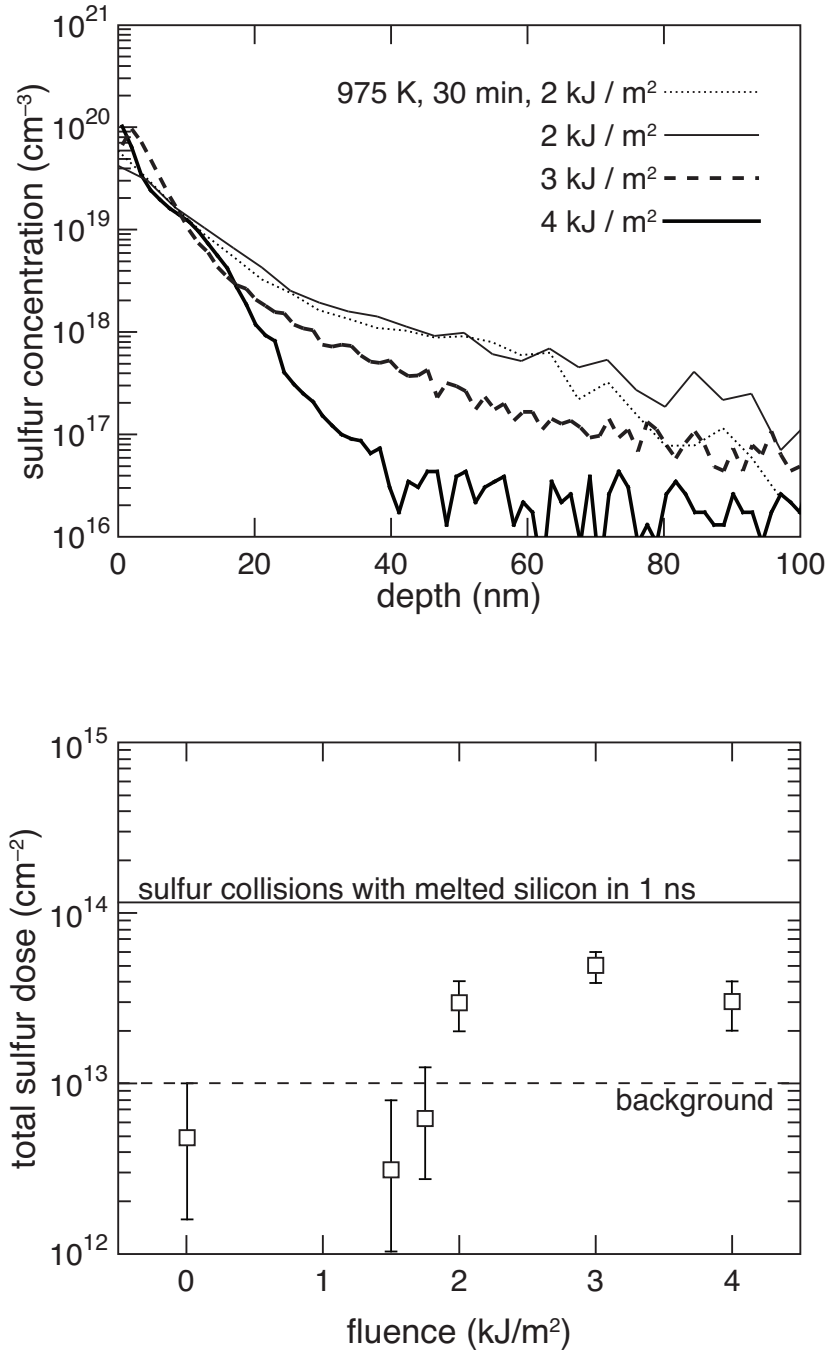


Figure 4.3: Results of SIMS measurements. *Top*: the depth dependence of the sulfur concentration, and *bottom*: by integrating the curves in the top figure, we obtain a total dose. Also shown is the limit of our detection due to oxygen contamination.

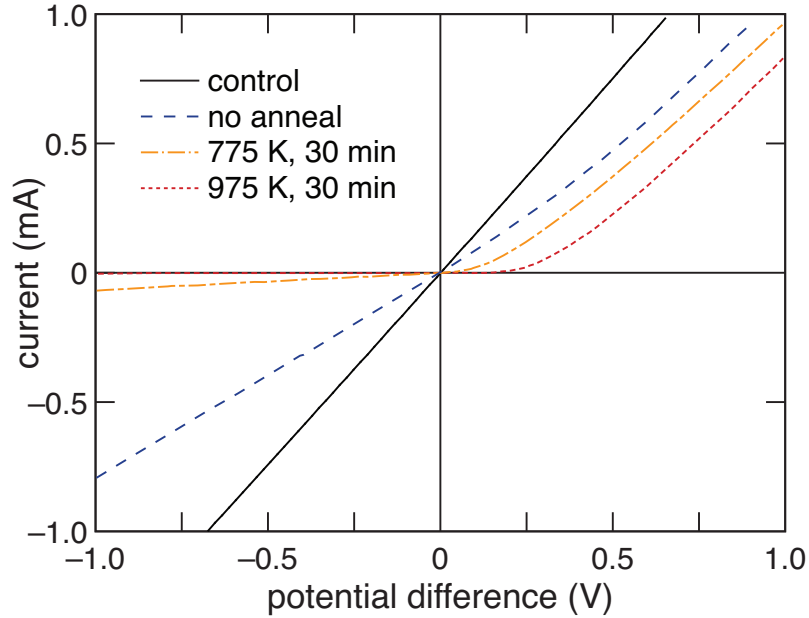


Figure 4.4: The $I - V$ properties of the junction between silicon doped with sulfur using a single fs-laser pulse and the p-type silicon substrate.

across the surface quite complex and impossible to measure. As a result, it was not clear if melting of the surface was sufficient for inclusion of the dopant, or if substantially higher fluences – such as those necessary for ablation, or plasma formation – were required.

This work answers that question definitively: sulfur dopants are included as a result of melting. The melting threshold for silicon irradiated by fs-laser pulses is generally accepted to be 1.5 kJ/m^2 [89], although numbers as high as 2.5 kJ/m^2 have been reported [91]. The discrepancy in the literature arises from different experimental standards, as well as important differences in experimental conditions such as laser wavelength and pulse duration. Regardless, the laser fluence that we observe to be the threshold for dopant inclusion (2 kJ/m^2), falls firmly within the reported thresholds for silicon melting by femtosecond laser pulses, and well below any higher fluence phenomena such as ablation.

Additionally, we can speculate as to the mechanism of dopant inclusion by consid-

ering the total number of collisions of ambient gas molecules with the molten silicon surface. If the observed sulfur dose exceeds this quantity, sulfur must be actively driven into the melt by, for example, the high local electric fields present in the femtosecond laser pulse, or adsorption of sulfur onto the silicon surface prior to irradiation. Using the kinetic theory of gases, we can estimate the number of gas molecule collisions with the molten silicon surface per unit area as:

$$\sigma = p\Delta t(2\pi mk_b T)^{-1/2}, \quad (4.2)$$

where Δt is the time for which the surface is molten, p is the pressure of the gas, m is the mass of the gas molecule, k_b is the Boltzmann constant, and T the temperature of the gas. We do not know the duration for which our surface is molten, but the timescale for resolidification after irradiation by fs-laser pulses is well known to be on the order of nanoseconds; we estimate $\Delta t = 1$ ns. We approximate the thermal interaction with the gas as adiabatic, as convection should occur more slowly than the conductive cooling responsible for resolidification of the molten silicon; thus $T \approx 300$ K. The result of this crude calculation is shown in Figure 4.3. We see that the the flux of sulfur atoms through the molten surface is sufficient to account for the concentrations we find in our samples. This crude calculation certainly does not rule out more exotic processes, but it shows that they are not necessarily required to explain the presence of sulfur.

The solid solubility limit of sulfur in silicon is about 10^{16} cm⁻³ [38,40], so it remains to be answered how we obtain sulfur concentrations almost four orders of magnitude higher near the surface of the laser-doped region. We believe we can explain this as a result of solute trapping, a process capable of freezing dopant atoms into a re-solidified layer well above the solid solubility limit. After sulfur goes into solution with the molten silicon, the liquid layer will eventually re-solidify as heat diffuses into the substrate. For pulses

just above the melting threshold, the melt duration is not sufficient to allow crystalline regrowth; whereas for higher intensity pulses, the melted layer remains molten long enough for epitaxial growth can occur [77]. We expect resolidification of the melted silicon layer should be amorphous because we employ fluences significantly less than 5.5 kJ/m^2 , the published threshold for re-solidification in a crystalline phase for 100 fs pulses centered at an optical wavelength of 800 nm [91]. Inspection of cross-sectional bright-field TEM images confirms the samples studied here re-solidify in an amorphous phase [131]. The re-growth of the silicon as either amorphous or crystalline is fundamentally governed by the speed of the resolidification front, v_s . If v_s exceeds approximately 15 m/s, the molten silicon will return to the solid state in an amorphous configuration; at slower velocities crystalline regrowth should occur [96]. Because we observe the silicon resolidifies in an amorphous phase, we know that our solidification front must move faster than 15 m/s. This solidification front velocity is well in excess of that necessary for solute trapping of the sulfur atoms. The exact degree of solute trapping depends on details of the diffusive speed of the dopant in the melt and along the solid-melt interface, but generally becomes significant as v_s approaches 1 m/s [45, 46].

There are several elements of the SIMS data that we have no complete explanation for at the present time, however. For example, the shape of the sulfur profiles are steeper with increasing fluence. Such behavior could result from slower crystal re-growth for samples exposed to higher fluence: slower re-growth velocity generally results in a higher degree of segregation of the sulfur across the liquid-solid interface during re-growth [45], thus leading to the steeper profiles we observe. Additionally, to within our experimental error, the total sulfur dose implanted into the silicon appears to be independent of the incident laser intensity, provided we are above the melting threshold. We would expect the melt duration to increase with deposited laser energy; if the sulfur does end up in solution by simply

diffusing into the melt and subsequently being trapped, we would expect deeper melts of longer duration to yield higher sulfur doses. It is possible that the answer to both of these questions could be resolved with a high-atomic resolution SIMS measurement that could help us better distinguish between sulfur and oxygen, which would reduce the error bars in our experiment.

Sulfur is a well-known double donor in silicon [129]. The Hall data we obtain indicates a substantial increase in the density of negative charge carriers immediately following irradiation. However, care must be taken in the interpretation of this measurement, as the surface layer includes a significant fraction of amorphous material. Hall measurements on amorphous silicon are fraught with difficulty, and it is possible to obtain an anomalous sign in the Hall coefficient [132]. However, assuming this negative Hall coefficient arises from sulfur donors, we note that the sheet carrier concentration is identical for both 3- and 4-kJ/m², an observation consistent with the insensitivity of total dose to laser fluence.

To confirm whether sulfur does act as an electron donor, we can turn to Figure 4.4. We see clearly that the junction between the laser doped region and the silicon substrate exhibits rectification, a clear sign of a p-n junction and proof that the sulfur atoms act as electron donors. Thermal annealing was necessary to observe rectification, suggesting that the loss of crystalline order immediately following laser irradiation does prevent the formation of a rectifying junction. Bright-field TEM confirms that samples annealed to 975 K for 30 min have re-crystallized in all regions but the top-most 10 nm [131].

Our demonstration diodes have a high saturation current, or a relatively low shunt resistance, or both. However, our purpose in fabricating these devices was simply to further substantiate our claim that the sulfur does indeed introduce electron donating states at room temperature. It is likely that our final HF etch to remove the native oxide prior to metallization — which necessarily etches away some of the insulating SiO₂ layer around

the doped region — created a non-negligible shunt path. Additionally, our fabrication process creates an inhomogeneous boundary between the doped region and the substrate (*e.g.*, current that flows horizontally rather than vertically through the doped region in Figure 4.2). Both of these issues likely degrade the diode performance, and could be avoided with a fabrication recipe that involved isolating the doped areas as mesas using an etch step after laser-doping. This issue will be addressed in future work.

4.6 Conclusion

After our analysis, we can come to several important conclusions, as well as raise several additional questions. Structurally, our analysis has shown that the interaction of a single laser pulse above the melting threshold implants a non-equilibrium concentration of sulfur from an ambient SF₆ environment. For the fluences we investigated, the surface layer was amorphous following irradiation. The implanted sulfur atoms may serve as electron donors, and a diode can be formed with an appropriate silicon substrate following a brief thermal anneal. We currently have no explanation for the implant mechanism or dopant distribution, but our data is consistent with diffusion from the gas phase into the molten silicon.

These findings are important for several reasons. The fact that the surface layer is amorphous is perhaps predictable given existing literature cited above, but initially surprised us because silicon doped via exposure to hundreds of laser pulses per area is distinctly polycrystalline following laser treatment [66]. One might have expected that additional melting and resolidification of the surface could only lead to additional disordering of the surface layer, but that is clearly not the case. We speculate that the focusing effect of the surface roughness developed on these surfaces must raise the effective fluence above that

necessary for crystallization during resolidification. Additionally, our finding that the surface layer is doped to almost 1% atomic after irradiation with a single laser pulse is a very important finding for the field of femtosecond laser doping. This result reinforces that the formation of these rough surfaces is not co-requisite with fs-laser doping.

In closing, we wish to re-emphasize that femtosecond laser doping should be viewed as distinct technique for including high concentrations of sulfur into a silicon matrix. Other techniques, such as ion-implantation or ns-laser melting have also been used for this purpose. Although re-solidification occurs in an amorphous phase at the laser fluences we explored, we expect that several possibilities exist for regaining crystalline order while maintaining non-equilibrium dopant concentrations, such as ns laser melting and resolidification or the use of higher fs-laser fluences. We have yet to determine the relative advantages and or disadvantages of using femtosecond laser pulses toward this end, and will explore this subject in greater detail in future publications.

4.7 Acknowledgments

Several people contributed to the work described in this paper. The author conceived the experiment, and collected and analyzed the data; Meng-Ju Sher assisted with these efforts. Matthew Smith collected and analyzed the TEM images. Eric Mazur supervised the research and the development of the manuscript. We gratefully acknowledge the assistance of Tom Mates collecting the SIMS data; additionally, Michael Aziz and Brion Bob helped analyze the SIMS data and shared the data necessary to correct for the detector saturation error. The research described in this paper was supported by the National Science Foundation under contract CBET-0754227. The author gratefully acknowledges support from the National Science Foundation Graduate Research Fellowship Program.

Chapter 5

Optical and electronic properties of femtosecond laser-doped silicon

5.1 Abstract

Silicon doped with sulfur beyond the solid solubility limit has many fascinating optical and electronic properties, such as strong absorption of photons with energy less than the band gap of silicon. In this paper, we report new observations that reveal the electronic states that sulfur introduces into the silicon band structure when implanted to concentrations of approximately 10^{20} cm^{-3} using fs-laser irradiation. When experimental conditions are such that we are able to electrically isolate the laser-doped region, temperature-dependent Hall measurements reveal that the free electron concentration is insensitive to temperature. The current-voltage properties of the junction between laser-doped silicon and a variety of silicon substrates confirm the active sulfur donor concentration, and also suggest Fermi-level pinning in the upper third of the band gap. This observation is also consistent with the formation of an impurity band.

5.2 Introduction

Recently, there has been great interest in creating silicon-based opto-electronic devices that operate at photon energies less than the band gap ($E_g = 1.12$ eV) by including a high concentration of deep states in the band gap [14, 49, 71]. We have demonstrated femtosecond laser doping of silicon with sulfur as a route to sub-band gap silicon devices; significant achievements to-date include high absorption for photon energies as low as 0.5 eV [65], and fabrication of photodiodes with significant responsivity to photon energies as low as 0.8 eV [71]. Doping silicon in this fashion introduces greater than 10^{20} cm⁻³ sulfur atoms into the silicon lattice [53], a concentration beyond the critical concentration for Mott transition [13, 19, 125]. Several papers have suggested that such concentrations may lead to impurity bands with potential applications as detectors [71] and photovoltaics [12, 13]. Although we have previously speculated that the high concentration of sulfur introduced via fs-laser doping yields an impurity band somewhere inside the band gap of silicon, we have not had evidence for what electronic states give rise to this potential impurity band. In this chapter, we discuss new results that shed light on the electronic states introduced by the sulfur dopants.

A detailed description of our previous results can be found elsewhere [51, 53, 65, 66, 68, 70, 71]. We provide only a brief summary here: irradiation of silicon with fs-laser pulses above the ablation threshold while in a gaseous or solid chalcogen (S, Se, Te) environment introduces approximately 10^{20} cm⁻³ chalcogen atoms into a thin, approximately 100 nm, polycrystalline layer at the silicon surface. Additionally, the surface of the silicon wafer is transformed from a flat, mirror-like finish to a highly-textured surface covered by a quasi-periodic array of micro- or nano-spikes. A brief thermal anneal improves crystallinity, and yields a rectifying junction between the laser-doped region and the silicon substrate. Room

temperature Hall measurements confirm a significant increase in the concentration of free electrons after laser-doping [71]. We have speculated that chalcogen dopants, which can introduce a variety of electron states deep in the upper half of the band gap of silicon [129, 130], act as electron donors and potentially form an impurity band that gives rise to the optical absorption.

In this letter, we provide additional details of the optical and electronic properties of silicon doped with sulfur using fs-laser pulses. Temperature-dependent Hall measurements reveal that when we can achieve electrical isolation of the fs-laser doped region, the electron concentration is insensitive to temperature. We also show that the integrity of the rectifying junction — essential for layer isolation in our Hall measurements — is a somewhat delicate function of temperature. The dependence of the electrical properties on substrate dopant (type and concentration) suggests that the Fermi level E_F is pinned approximately 300 meV below the conduction band edge ($E_C - E_F \approx 300$ meV). These observations are all consistent with the formation of an impurity band centered somewhere near $E_C - E_F \approx 300$ meV.

We conducted two experiments as part of this investigation. Using silicon substrate doped p-type ($\rho = 1 - 20 \Omega\cdot\text{cm}$), we fabricated non-equilibrium sulfur-doped silicon regions that form rectifying junctions with the substrate. Using these samples, we can measure the fs-laser doped surface region, electrically isolated from the substrate by the junction. We use these samples to perform temperature-dependent transport measurements; we confirm the junction properties over the temperature range of interest first, though. Next, we explore the nature of the junction of fs-laser doped silicon with silicon substrates of several doping types and concentrations at room temperature. From these measurements we learn about the location of the Fermi level in the laser doped region.

5.3 Experimental

For all measurements below, we prepare (100) silicon wafers (boron doped, $\rho = 1 - 20 \Omega\cdot\text{cm}$) using the RCA clean [104]; for $I - V$ measurements conducted at room temperature, we prepare additional silicon substrates, one for each row of Table 5.1. After cleaning, we etch the native oxide in a dilute (5%) HF solution, and immediately transfer the wafer to a vacuum chamber. The chamber is evacuated to high vacuum ($p < 10^{-4}$ Pa), and subsequently backfilled with 6.7×10^4 Pa of SF_6 gas. The wafers are placed in front of the focus an amplified femtosecond laser pulse, oriented with the wafer surface perpendicular to the laser beam. The laser pulses are produced by a regeneratively amplified titanium:sapphire femtosecond laser system, center wavelength of 800 nm, pulse duration of 75 fs, and repetition rate f . We measure the spatial profile at the sample surface by deflecting the beam into a CCD camera, and calculate laser pulse fluence by dividing pulse energy by the area of the pulse (defined as the area of the pulse with intensity greater than $1/e$ of the maximum). Using stepper motors, we translate the silicon wafer in raster scan pattern that achieves a uniform distribution of laser pulses across the area to be doped. Translation parameters are chosen such that the distance between any two laser pulses is $\Delta_x = v/f$ in the x-direction, and $\Delta_y = \Delta_x$ in the y-direction. We choose the spatial extent of the laser intensity profile and stepping distances (Δ_y, Δ_x) such that $\pi w^2/\Delta_y\Delta_x = 100$; where w is the full-width at half-maximum of the laser intensity profile, and all other parameters are defined above. Specific parameters are approximately: $f = 25$ Hz, $v = 1400 \mu\text{m/s}$, $w = 590 \mu\text{m}$, and pulse energy 1.6 mJ. The laser fluence is 4 kJ/m^2 . Following laser-irradiation, we thermally anneal the doped wafer at 975 K for 30 min in an open tube furnace, while flowing 300 sccm (5×10^{-2} standard l/s) forming gas (95 % He, 5% H_2).

After irradiation, we prepare samples appropriate for Hall and $I - V$ measure-

Type / Dopant	Resistivity ($\Omega\text{-cm}$)	Carrier concentration (cm^{-3})	$E_c - E_f$ (meV)
p/B	0.015	$+5.5 \times 10^{18}$	1075
p/B	10	$+1.5 \times 10^{15}$	862
p/B	100	$+1.4 \times 10^{14}$	801
p/B	5000	$+2.2 \times 10^{12}$	694
n/P	5000	-1.0×10^{12}	444
n/P	100	-4.9×10^{13}	343
n/P	10	-5.0×10^{14}	283

Table 5.1: Selected properties of silicon substrates laser-doped with sulfur

ments. We etch the native oxide from the surface using a dilute (5%) solution of HF, and evaporate aluminum contacts on both the laser-exposed and substrate surfaces using an electron beam evaporator. For $I - V$ measurements, we then isolate the edges and define approximately square areas with sides $L \approx 5$ mm by cleaving the wafer. We proceed to measure the current-voltage properties of the junction between the laser-doped region and the substrate by applying a bias between the front and back contact and measuring the resulting current. The voltage is defined positive when the p-type substrate is raised to a higher potential than the laser-doped region. We perform the $I - V$ measurements in a closed-cycle He cryostat, and measure the $I - V$ properties over a sample temperature range $20 \text{ K} < T < 800 \text{ K}$. Temperature steps are taken to be either $\Delta T = 10 \text{ K}$ or $\Delta(1000/T) = 2 \text{ K}^{-1}$, whichever corresponds to a smaller temperature change. We repeated the sample preparation procedure just described for the silicon substrates detailed in Table 5.1. However, for these samples we collected only room-temperature $I - V$ data.

For Hall and resistivity measurements, we take the metallized sample and mask circles of diameter 1.5 mm located on a 1 cm grid on the doped surface using standard positive photoresist. We etch the unmasked Al layer using a commercial Al etch, and cleave the waver such that we form square van der Pauw samples with dimensions $1 \text{ cm} \times 1$

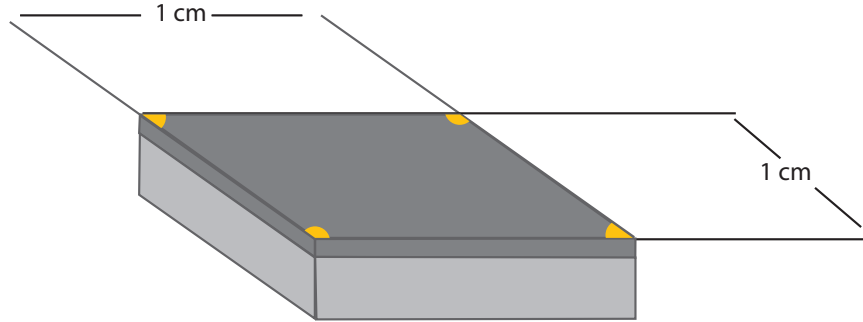


Figure 5.1: Van der Pauw sample geometry for Hall measurements.

cm, and semi-circular contacts that extend 0.75 mm from each corner. Sample geometry is shown in Figure 5.1. We load the Hall samples into the cryostat described above and measure the resistivity and Hall effect using standard techniques (described in Chapter 3 and reference [109]). Our setup includes signal multiplexing that allows us to correct for standard errors by collecting redundant measurements of the Hall voltage. We collect resistivity and Hall effect data over a temperature range $20 \text{ K} < T < 800 \text{ K}$. The samples are immersed in a magnetic field of approximately 0.75 T (data are collected for positive and negative fields), and excited with the lowest possible current to generate a Hall voltage of approximately $10 \mu\text{V}$. We observe no self-heating effects. Temperature steps are taken as described above for $I - V$ measurements.

5.4 Results

The structural and morphological properties of the laser-irradiated substrates have been explored in detail for similar exposure conditions [55], and are similar to those shown in Figures 2.2 and 2.4, and a brief description of the structure of the resulting laser-doped layer was given above in section 5.2. For the purposes of this chapter, the critical data are that a sulfur-doped polycrystalline layer extends approximately 100 nm into the silicon

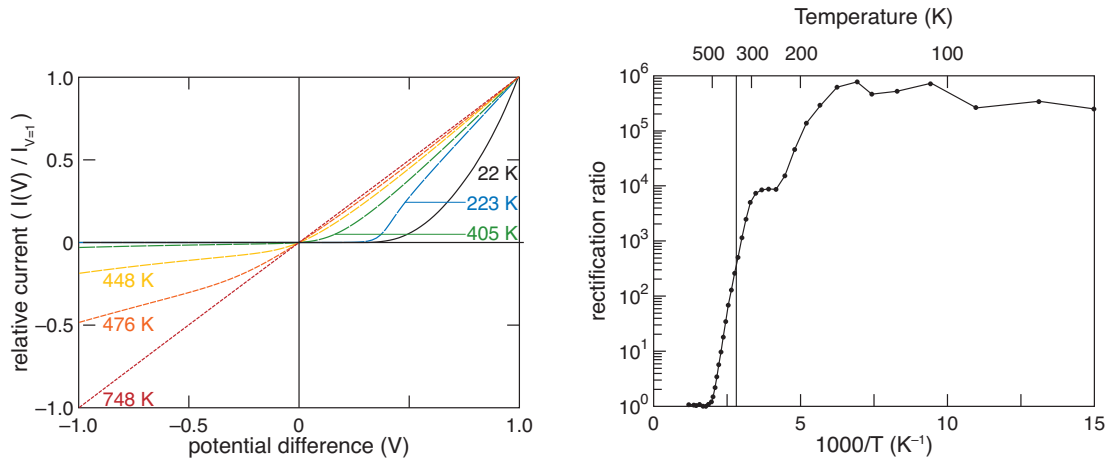


Figure 5.2: *Left:* Selected $I - V$ curves for various temperatures; to show them on the same scale we have normalized such that $I(V = 1) = 1$. *Right:* The “rectification ratio,” defined here as $I(V = 1)/I(V = -1)$, gives us a semi-quantitative impression of the nature of the junction. The vertical line marks $T = 355$ K for comparison with Figure 5.3

wafer from the roughened surface. The junction between that layer and the substrate can, given appropriate preparation that we describe below, exhibit rectifying properties.

Figure 5.2 shows the temperature dependent current-voltage relationship of the junction between the fs-laser doped silicon and the p-type ($1 - 20 \Omega\text{-cm}$) substrate. For the temperature range we measure, the junction rectifies near and below room temperature, but has linear $I - V$ properties at higher temperatures. The magnitude of the current changes by several orders of magnitude over the temperature range probed. In order to more easily compare the qualitative nature of the junction (*i.e.*, whether it rectifies or not), we normalize each data set: for each temperature, we divide the current at each voltage by the current at a potential difference of $+1$ V. Six representative temperatures have been chosen. We observe significant deviations from rectification above approximately $T = 400$ K. In Figure 5.2, we plot as a function of reciprocal temperature the ratio of current through the forward-biased junction (potential difference $+1$ V) to current through the reverse-biased junction (potential difference of -1 V). This ratio is a semi-quantitative metric of the quality or

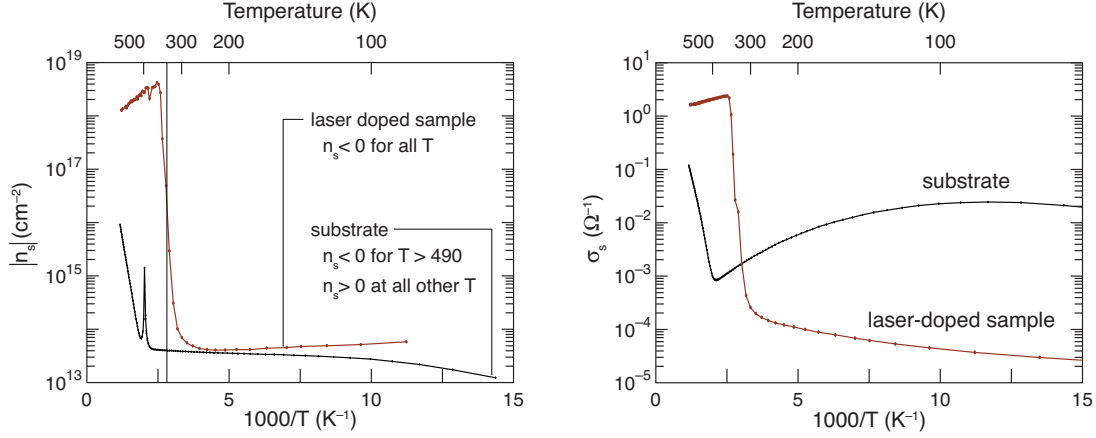


Figure 5.3: *Left*: Magnitude of the sheet carrier concentration n_s versus $1000/\text{Temperature}$. The charge carrier sign is noted in the plot; note the substrate's charge carrier changes sign at the spike just below 500 K. *Right*: The sheet conductance of both samples σ_s versus $1000/T$. The vertical line marks $T = 355$ K for comparison with Figure 5.2, and the lines connecting data points are only to guide the eye.

degree of rectification. A vertical line corresponding to $T = 355$ K is drawn on the plot for comparison with the Hall effect data; heating to this temperature does not change the data obtained at lower temperatures.

Figure 5.3 shows the temperature dependence of the sheet conductivity σ_s and sheet carrier density n_s plotted against reciprocal temperature. The conductivity is measured using the standard van der Pauw technique [115]. We calculate n_s from the Hall voltage using the relationship

$$n_s = r_H \frac{I_e B}{q V_{Hall}}, \quad (5.1)$$

where I_e is the excitation current, B is the applied magnetic field, q is the elementary charge, V_{Hall} is the measured Hall voltage, and r_H is the Hall scattering factor. We make the approximation that $r_H = 1$, an approximation that we expect will introduce an error of order unity [107], but does not materially affect our conclusions. We use an un-irradiated p-type substrate of nominal resistivity $1 - 20 \Omega\text{-cm}$ as a control sample. The control sample

exhibits a positive charge carrier at temperatures below $T \approx 490$ K; above this temperature, we observe a transition to the intrinsic excitation regime, in which we observe a negative charge carrier. We measured the control sample thickness to be $d = 320 \pm 5 \mu\text{m}$, which we used to calculate the carrier concentration and resistivity. At room temperature, we measure a resistivity of $15 \Omega\cdot\text{cm}$, a carrier concentration of $n = 1.2 \times 10^{15} \text{ cm}^{-3}$, and a Hall mobility of $344 \text{ cm}^2 / \text{V}\cdot\text{s}$. Additionally, if we fit the temperature dependence of the control sample using the techniques described in Chapter 3, we obtain an ionization energy for the boron acceptors of $E_A = 47 \pm 2 \text{ meV}$. All of these values are within 5% of published values [32, 33, 133].

We also plot the magnitude of n_s for the fs-laser doped sample in Figure 5.3; the sign of the charge carrier is negative for the laser-doped sample at all temperatures. We observe a sharp transition in the value of n_s near $T = 355$ K: at temperatures below this transition, n_s changes by less than 15% around a mean value of $n_s \approx 5 \times 10^{13} \text{ cm}^{-2}$, slightly increasing as we cool. The Hall voltage was not measurable below $T_{min} = 90$ K due to excessive noise in the measurement; we suspect the contacts are to blame. Above this transition, the sheet carrier concentration changes rapidly, increasing to $n_s \approx 5 \times 10^{18} \text{ cm}^{-2}$, and then falling briskly with increasing temperature. The vertical line at the $T = 355$ K designates the approximate temperature of the transition, and can be compared to a marker at the same temperature in Figure 5.2. We observe that the transition in junction behavior (from rectifying to non-rectifying) occurs at the same temperature as the large change in sheet carrier concentration.

In Figure 5.4 we plot the room temperature current-voltage properties of the junction between fs-laser doped silicon and wide variety of silicon substrates (properties in Table 5.1). Once again, because of the large range of forward bias currents, we normalize the current values at each measurement temperature to the current value through the junction

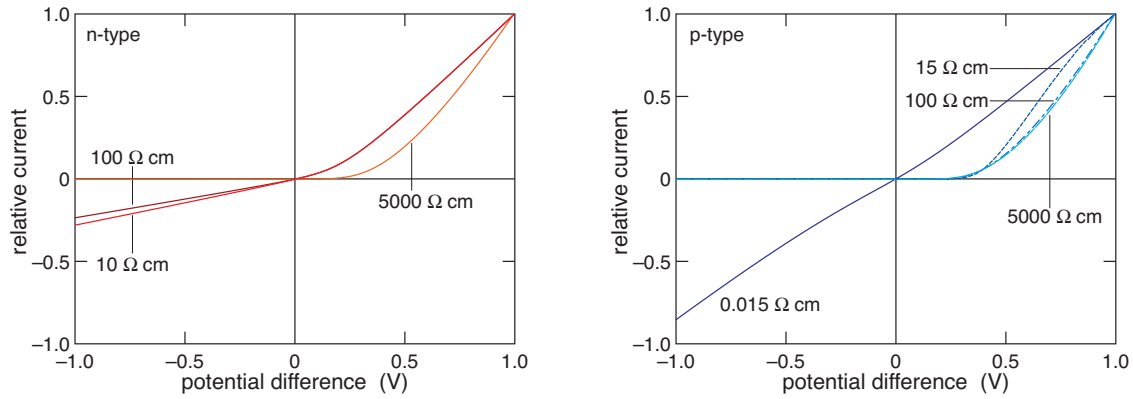


Figure 5.4: Current-voltage properties of the junction between fs-laser doped silicon and silicon of various resistivities; we plot separately the data for both n-type (left) and p-type (right) substrates. More details of substrate properties can be found in Table 5.1

under a forward bias of +1 V. We observe that all substrates exhibit rectification except the highly doped p-type substrate ($\rho = 0.015 \text{ } \Omega\cdot\text{cm}$) and the more heavily doped n-type substrates ($\rho = 100 \text{ } \Omega\cdot\text{cm}$, $10 \text{ } \Omega\cdot\text{cm}$). This information is shown in Figure 5.5, where we again show the ratio of current through the forward-biased junction (+1 V) to the current through the reverse-biased junction (-1 V).

5.5 Discussion

5.5.1 Electrical measurements on p-type 1—20 $\Omega\cdot\text{cm}$ silicon

We begin our analysis with Figures 5.2 and 5.3. We use Figure 5.2 as a diagnostic tool in determining the temperature regime over which we can assume the laser-doped region is electrically isolated from the substrate. When we observe rectifying behavior at the junction between the laser-doped region and the substrate, we will assume that the current that we use to excite the Hall voltage is constrained to the surface layer. We will discuss issues that can arise from this assumption in section 5.5.3. We will also discuss reasons for this change in junction behavior at the end of this section.

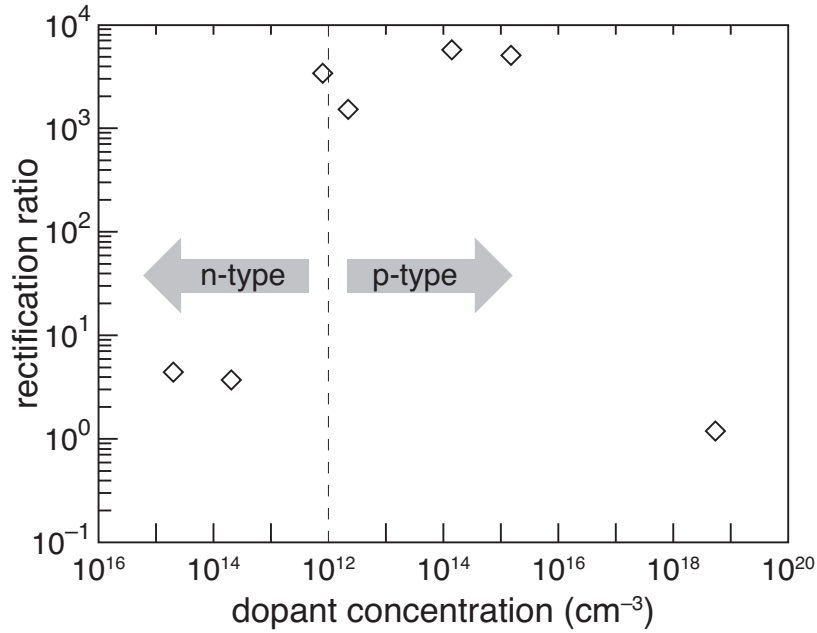


Figure 5.5: A plot of the rectification ratio ($I_{V=+1}/I_{V=-1}$) for the range of substrate dopant type and concentrations (see Table 5.1 for more details). We observe rectification only for a range of substrates.

Upon inspection of Figure 5.2, we divide the Hall data into a high and low temperature regime separated at approximately $T_{sep} = 355$ K (marked as vertical line on both graphs). Below T_{sep} , the junction between the laser doped layer and the substrate is strongly rectifying, exhibiting leakage currents of $I_{leak} \leq 1 \mu\text{A}$ at room temperature and which decrease exponentially as we cool the sample. As we will discuss in detail below (Section 5.5.3), in this regime, we believe the sheet carrier concentration accurately reflects the properties of the crystalline grains in the laser-doped region layer. Our first observation from the temperature dependence of the Hall data is that the majority carrier are electrons. Because we began with a p-type substrate which shows the expected p-type conduction in this temperature regime, we conclude that the sulfur is acting as an electron donor. Of course, the presence of a rectifying junction between the laser-doped region and the substrate also indicates this fact.

Perhaps more interestingly, the carrier concentration shows no significant temperature dependence. There is a slight increase in carrier concentration from $4.2 \times 10^{13} \text{ cm}^{-3}$ to about $5.5 \times 10^{13} \text{ cm}^{-3}$ as we cool from 250 K to 90 K. One characteristic sign of impurity band conduction in Hall effect data is a local minimum in carrier concentration during cooling [19,24]. The behavior we observe could correspond to such a minimum, although an increase of this amount could stem from several other factors that we are neglecting in this analysis (such as grain boundary effects or the Hall scattering factor). Thus, linking this behavior to impurity band conduction is not possible. More importantly, we must compare the data in Figure 5.3 to Figure 3.5, in which we plotted the temperature dependence of sulfur ionization for equilibrium sulfur levels at 180 meV and deeper below the conduction band edge. Such states are extremely temperature sensitive in this regime due to the deep binding energy of sulfur electrons. Other than a transition to metallic conduction, we can think of no reason to explain the insensitivity of sulfur donors to temperature. Observations of a temperature independent carrier concentration is one hallmark of the transition to metallic conduction in semiconductors [119].

Indeed, given the high concentration of sulfur (about 1% [53]), we have certainly exceeded the critical concentration for a metal-insulator transition. If we make the rather unlikely assumption that the sulfur donors are distributed uniformly in the top-most 100 nm, we could estimate the free carrier concentration to be:

$$n_s/d = \frac{5 \times 10^{13} \text{ cm}^{-2}}{10^{-5} \text{ cm}} = 5 \times 10^{18} \text{ cm}^{-3}. \quad (5.2)$$

Measurements we consider below will support this estimate of carrier concentration. We note immediately, though, that it is quite unlikely that sulfur atoms are distributed uniformly in the top-most 100-nm. In Chapter 4, we found that for single laser pulse irradiation,

the sulfur concentration is peaked strongly near the surface. If this were also the case in the samples we study here, d in equation 5.2 would be effectively smaller, thus making the estimate of Equation 5.2 a lower bound on carrier concentration. In either case, these concentrations should be compared to the Mott transition critical density: the concentration at which we expect to see metallic conduction due to wave-function overlap. The critical concentration for a Mott transition to metallic conduction for phosphorus-doped silicon has been measured to be $3.74 \times 10^{18} \text{ cm}^{-3}$ [28]. For sulfur, we estimated the critical concentration to be near or above 10^{19} cm^{-3} in Chapter 3; in chapter 6 we will confirm that estimate. Thus, it is quite likely that the sulfur donors are above the critical density for a Mott transition, and we should expect the sulfur electrons to assume delocalized states. Electronic conduction from these states will be metallic and quite insensitive to temperature, just as we observe.

We now consider the temperature regime above $T_{sep} \geq 355 \text{ K}$. Considering Figures 5.2 and 5.3, we were originally tempted to speculate that the transition and accompanying loss of rectification indicated a lack of layer isolation. Thus, our exciting current for both Hall and resistivity measurements would be distributed through both the fs-laser doped region and the substrate according to standard circuit equations. However, a careful inspection of Figure 5.3 reveals that there must be an altogether different phenomenon occurring. The sheet conductivity of the laser doped sample increases over four orders of magnitude between $T = 300 \text{ K}$ and $T = 400 \text{ K}$; however, the sheet conductivity for two parallel layers should simply sum:

$$\sigma_{s,equiv} = \sigma_{s,laser} + \sigma_{s,sub}. \quad (5.3)$$

However, we know precisely how the substrate behaves before and after the transition (shown in Figure 5.3). At $T = 400 \text{ K}$, just above the transition, the substrate's sheet conductivity $\sigma_{s,sub} \approx 10^{-3} \Omega^{-1}$. At temperatures below this transition, the laser-doped

region exhibits comparatively slowly varying behavior; if it were the case that it was only the junction that changed at the transition, we should be able to approximate, to first order, the sheet conductivity of the laser doped region by a value not much larger than its value below the transition ($\sigma_{s,laser} \approx 10^{-4} \Omega^{-1}$). However, the sheet conductivity is four orders of magnitude larger than the sum of $\sigma_{s,laser}$ and $\sigma_{s,sub}$! Thus, it appears that something significant changes in the laser-doped region near $T = 355$ K that changes the nature of the conductivity. It may be that this change is what causes the loss of rectification. However, at the current time, we are unsure what mechanism is responsible for the behavior we observe.

To summarize our analysis of the temperature dependent electrical data shown in Figures 5.2 and 5.3, it appears that below a temperature of $T = 355$ K, we have achieved good layer isolation. In this temperature regime, we observe a carrier concentration and insensitivity to temperature change consistent with the presence of an impurity band. We will see further evidence of this below. Above this temperature, we observe a significant increase in the conductivity in our samples that we have shown must arise in the fs-laser doped region. We are unclear what causes this change, but this change to a highly conducting state is correlated with a loss of rectification at the junction between the fs-laser doped region and the substrate. We do not speculate further on this topic.

We note in closing that the phenomena we observe in the temperature-dependent Hall measurements are not limited to the specific experimental parameters we have chosen. We observe comparable behavior on a variety of silicon substrates and annealing conditions.

5.5.2 Electrical measurements on other silicon substrates

In consideration of the $I - V$ measurements of laser-doped silicon with a variety of silicon substrates, we will introduce several additional concepts into our interpretation of the data. We outline the argument before we begin for clarity. We expect the $I - V$

characteristics of a junction between laser-doped silicon and a crystalline substrate to be of a rectifying nature provided the Fermi level of the laser-doped region is substantially above that of the substrate we choose. If the sulfur-dopants take isolated states, we can calculate that the Fermi level in the laser-doped region should not be much deeper than 100 meV below the conduction band edge, while if they form an impurity band it should be pinned near the impurity states, potentially as deep as 300 meV below the conduction band edge. The substrates for which we observe rectification suggest that the Fermi level is substantially deeper than 100 meV below the conduction band edge, and thus supports the presence of an impurity band.

This argument is complimentary to our interpretation of the Hall data above, which we argued indicated a transition to metallic conduction via a Mott transition driven by a high concentration of sulfur dopants. We will argue in this section that the $I - V$ data presented in Figures 5.4 and 5.5 supports the presence of an impurity band (to explain Fermi level pinning several hundred meV below the conduction band edge). Such an impurity band could be responsible for the metallic conduction we observe in the Hall data.

Background on $I - V$ properties of a semiconductor junction

We begin with a brief review of semiconductor junctions. When two slabs of silicon doped with different types and/or concentrations of dopants are brought together, any concentration gradient of majority charge carriers will drive a diffusion current. For example, at a $p - n$ junction, the holes diffuse from the hole-rich p side to the hole-deficient n side, while electrons diffuse in the opposite direction. We could also consider an $n - n^+$ junction, for which electrons would diffuse from the heavily doped n^+ side to the less-heavily doped n side. In either case, the driving force for diffusion is evidenced by the different values of the chemical potential, or Fermi level, on each side of the junction; the Fermi level

in silicon at room temperature is uniquely determined by dopant type and concentration. The diffusion of charge carriers leads to the creation of an electric field near the junction — arising as charge carriers accumulate in or depart from previously neutral regions — that tends to oppose further diffusion. Diffusion will continue until the resulting electric field exactly cancels the driving force for diffusion — that is, until the *electrochemical* potential is equal on each side. This phenomenon is shown schematically in Figure 5.6.

The internal electric field of the junction can also be described by an internal voltage drop V_{int}^0 across the junction. It should be clear from Figure 5.6 that this voltage drop is given by

$$qV_{int}^0 = E_{f,1} - E_{f,2}, \quad (5.4)$$

where q is the elementary charge, and $E_{f,1}$ and $E_{f,2}$ are the Fermi levels on each side of the junction. The current-voltage properties of a semiconductor homojunction depend dramatically on the size of V_{int}^0 . We will concern ourselves primarily with the reverse bias case — which for a $p - n$ junction is defined as lowering the potential of the p-doped side relative to the n-doped side, and for a $n - n^+$ side is defined as lowering the potential of the n side relative to the n^+ side. Details of the theory of rectification can be found elsewhere [125, 133], and we will not review them in detail. We note, however, that the diffusion current across the junction will scale as $\exp(-V_{int}/k_bT)$; without an applied bias the diffusion current is exactly balanced by the drift current, and the total current is zero. Applying a voltage changes the size of the diffusion barrier presented by the junction, and in general leads to a change in the diffusion current by a factor of $\exp(-\Delta V/k_bT)$, where $\Delta V = V_{int} - V_{int}^0$.¹ In reverse bias, when $\Delta V > 0$ (*i.e.*, the potential drop across the

¹Note that $\Delta V = V_A$ for a $p - n$ junction, but will be slightly less for an $n - n^+$ junction; as shown in Figure 5.6. This arises because the junction between a p- and n-type region is fully depleted of carriers, and has extremely high resistance. For an $n - n^+$ junction, the n-region and the junction may have comparable

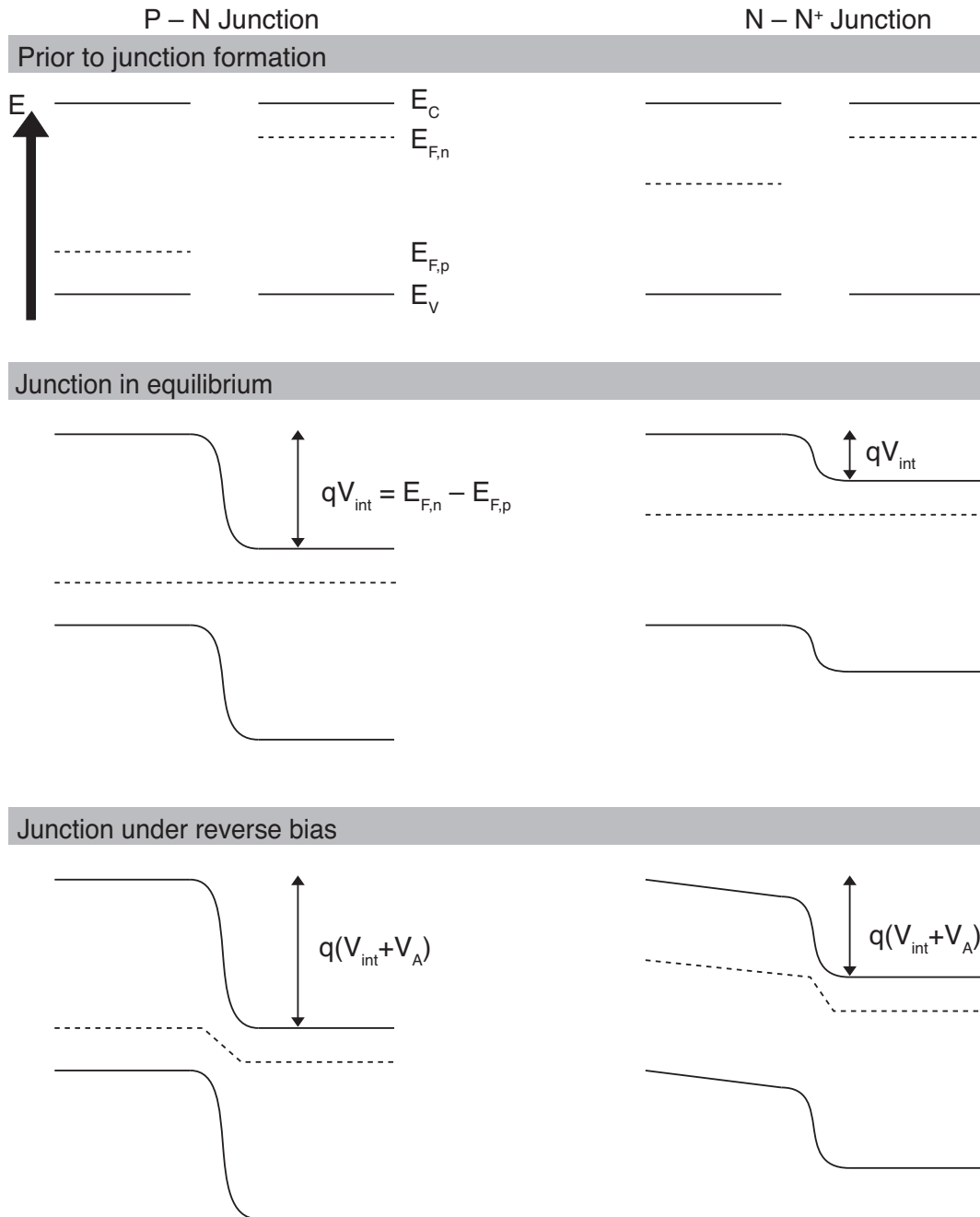


Figure 5.6: A graphic illustration of the behavior of band energies of silicon near the junction between two differently doped regions. The vertical axis is energy, and the horizontal direction is a spatial dimension. *Top*: In isolation at equilibrium, bands are unperturbed. *Middle*: Joined together at equilibrium, an internal potential V_{int}^0 develops at the junction such that the electrochemical potential is constant across the junction. *Bottom*: Disturbed from equilibrium by an externally applied potential, a gradient develops in the quasi-Fermi levels between the two differently doped regions.

junction increases), this leads to very small currents; in forward bias, for which $\Delta V < 0$, this leads to exponentially increasing currents.

Such nonlinear $I - V$ behavior is the essence of rectification, and will be observed provided qV_{int}^0 is significantly larger k_bT . We note before proceeding further that the ideal diode equation, as derived from traditional semiconductor transport theory [125], is of little help in interpreting the results that follow. The diode equation strictly only applies to a $p - n$ junction, for which the applied voltage can be considered to drop entirely across the region near the junction that is entirely depleted of free charge carriers, and thus of extremely high resistance (illustrated graphically in the bottom-left of Figure 5.6). For $n - n^+$ junctions, this is no longer true, as there is no depleted region due to the lack of a p-type region. In this case, an applied voltage V_A can generally be considered to cause a voltage drop across both the low-doped side of the junction, as well as the junction (see the lower-right portion of Figure 5.6). Rectification still occurs in such $n - n^+$ junctions under appropriate conditions [134], but depends on V_{int}^0 being large relative to room temperature.

Specific background for junctions formed with sulfur-doped silicon

We will use equation 5.4, knowledge of the substrate Fermi level, and the observation of whether or not a junction rectifies to estimate the location of the Fermi level in the laser doped region. We do not know the location of the Fermi level in fs-laser doped silicon, which we denote as $E_{F,laser}$, but we can easily calculate the location of the Fermi level in our substrates, which are doped with well characterized shallow donors such as phosphorus and boron. Thus by forming junctions of fs-laser doped silicon with a variety of conventional (boron- or phosphorus-doped) silicon substrates, and observing whether they rectify, we can perform a type of Fermi level “spectroscopy,” exploring the effect of varying resistances, and the voltage drop will occur across both regions.

$qV_{int}^0 = E_{F,laser} - E_{F,sub}$. We expect rectification when:

$$qV_{int}^0 = E_{F,laser} - E_{F,sub} > k_bT = 25 \text{ meV}, \quad (5.5)$$

The transition from linear to rectifying behavior is not an abrupt function of V_{int} .

Further, *in the case* that the sulfur donors act as isolated donors characterized by discrete energy level(s), we can estimate the value of $E_{F,laser}$. Although we do not know if the donors take one or many discrete levels, we will perform this calculation including the possibility that they all assume either the deepest or shallowest possible state, creating upper and lower bounds on our calculation of $E_{F,laser}$. From Figure 3.4, we see that at room temperature, and at donor densities of about 10^{19} , sulfur donor binding energies in the range $50 \text{ meV} \leq E_d \leq 300 \text{ meV}$ yield a Fermi level that is no farther than 140 meV below the conduction band edge. This range of donor energies, as evident from Figure 3.5, encompasses all of the well-noted, singly ionized, sulfur energy levels.² Thus, we can place a lower bound on the Fermi level in the laser doped region in the case that the sulfur atoms are isolated, and introduce discrete states rather than an impurity band:

$$E_{F,laser} \geq E_C - 140 \text{ meV}. \quad (5.6)$$

For the purposes of the experiment described here, this lower bound implies that the junction between the laser doped region and silicon substrates should be rectifying in nature when the substrate Fermi level is several k_bT below $E_{F,laser} \geq E_C - 140 \text{ meV}$. As is clear in Figure 5.5, it is only for a range of substrate choices that we observe rectification. We convey this information graphically, along with the location of the substrate Fermi levels and the (discrete) sulfur states, in 5.7.

²We exclude the doubly ionized levels because the free electron concentration is below the sulfur concentration by at least 1 – 2 orders of magnitude, according to the SIMS data outlined in Chapter 2.

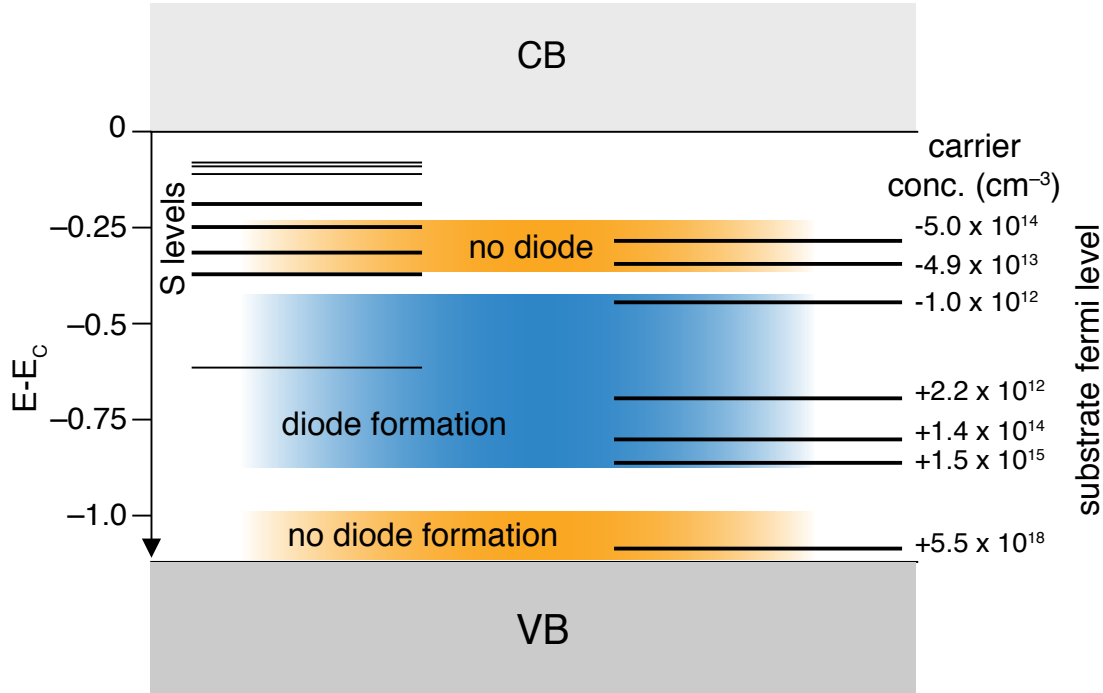


Figure 5.7: A graphic illustration of the location of the room temperature Fermi levels for the substrates used (right side; with the most heavily p-doped at the bottom, proceeding to the most heavily n-doped at the top) relative to the sulfur impurity levels (left side). The inability to achieve rectification for the more heavily doped n-samples indicates a small or non-existent Fermi level offset.

Interpretation of $I - V$ data

We use the above arguments to interpret our $I - V$ data. We first analyze the lack of diode formation when the Fermi level is near the bottom of the band gap. At this dopant concentration, the substrate Fermi level is near the valence band edge; we thus expect $V_{int}^0 \gg k_b T$ and to observe rectification. However, closer consideration reveals that it is unsurprising that we do not observe rectification. At this high p-type doping level, it is likely that the p-type dopant concentration exceeds the free electron concentration due to the sulfur donors. As we can see, the boron concentration is $5.5 \times 10^{18} \text{ cm}^{-3}$; in equation 5.2, we estimated the sulfur concentration to be comparable. If the boron dopant

concentration exceeds that of the sulfur donors, the sulfur donors will merely compensate the positive boron dopants concentration, introducing free electrons that annihilate a fraction of the free holes, but having the net effect of simply reducing the free hole concentration. However, unless the compensation is almost exact, the resulting fs-laser doped region will still have on order 10^{18} cm^{-3} free holes. The Fermi level will thus not be coerced into moving into another region of the band gap, and there will be no significant internal potential to cause rectification. This data point confirms our approximation of the sulfur concentration in the surface region.

For samples with lower concentrations of p-type doping, we do observe rectification. In these samples, the sulfur donors far exceed the background hole concentration, thus we end up with an n-type laser-doped region, with a Fermi level in the upper half of the band gap. This introduces a significant internal potential and yields rectification. Similarly, for our most lightly doped n-type sample, we observe rectification for the same reason.

For n-type substrates with doping concentrations of greater than 10^{13} cm^{-3} ($\rho > 100 \text{ } \Omega\cdot\text{cm}$), we cease to observe rectification between the fs-laser doped region and the substrate. We carefully consider this fact under two possible scenarios: one in which the high density of sulfur levels gives rise to an impurity band in the doped-region, and one in which they remain isolated electron states.

If no impurity band forms, the Fermi level must remain fairly far above the impurity levels introduced, simply to accommodate the fact that a large fraction of these deep levels must be filled at $T = 300 \text{ K}$. As we discussed for equation 5.6, for isolated sulfur states we can place a lower bound on the location of the Fermi level in the laser-doped region:

$E_{F,laser} \geq E_C - 140 \text{ meV}$.³ In this case, we would still expect V_{int}^0 to be fairly large for

³Note that the graphical results we used to generate this estimate can be calculated using the Equation 3.27. For example, for a sulfur concentration of $N_S = 10^{20}$ and $E_d = 300 \text{ meV}$, we calculate a Fermi level located 130 meV below the conduction band edge — a level that remains substantially above the substrate Fermi level in which we cease to observe rectification. Levels lying closer to the conduction band edge would

the junction between laser-doped silicon and n-type, 100 Ω -cm substrate ($V_{int}^0 \geq 200$ meV). However, we do not observe rectification between fs-laser doped silicon and this substrate, suggesting that V_{int}^0 is smaller than this value and that $E_{F,laser}$ is substantially farther from the conduction band than we predicted.

If an impurity band of deep sulfur levels forms, however, the additional empty states that become available after the impurity electrons delocalize will pin the Fermi level approximately at the location of the original impurity level states [13]. We observe rectification to cease once the substrate Fermi level approaches the well-known sulfur impurity levels. Thus, we hypothesize that the Fermi level must be pinned near these states, substantially below the Fermi level that would be enforced by discrete defect levels. This would introduce a V_{int} that is close to zero even for these lightly doped n-type samples, and explain the electrical properties we observe. Thus, we can say that the $I - V$ properties we observe are consistent with the formation of an impurity band near the published sulfur electron levels in silicon. We view this as corroborating evidence of the conclusion of our Hall data: fs-laser doped exhibits electrical characteristics that suggest the high density of sulfur states has driven a transition to a metallic state through delocalization sulfur electron states.

5.5.3 Comments regarding potential errors in the measurement of the Hall effect

There are several potential errors that can be present when performing Hall effect measurements on samples such as the ones on which we report. We believe we have avoided such errors. First, the dopant distribution in the laser-doped region is likely quite inhomogeneous with depth in the laser-doped layer. For this reason we present only the sheet-carrier concentration and sheet conductivity in Figure 5.3.

only yield E_f closer to the conduction band edge.

Second, in the temperature region $T \leq 355$ K, we are relying upon the rectifying junction between the laser-doped region and the substrate to isolate the surface layer. For $T < 355$ K, the junction between the laser-doped region and the p-type substrate rectifies with leakage currents on the order of μA . As has been reviewed before [111], diodes can be used for isolation of surface layer provided care is taken to ensure that the surface layer will always be reverse biased relative to the substrate (in the case of an n-type surface layer). In our case, we ensured this scenario by grounding the negative terminal of the current lead. We investigated the effect of gating the surface region as well (lifting the negative current terminal above ground to further reverse-bias the junction), but saw little effect in our data. Leakage currents can also introduce errors into our data due to our use of diode-isolation. Leakage currents can reduce the real excitation current I_e or shunt the Hall voltage V_{Hall} of equation 5.1. However, by keeping excitation currents significantly larger than the junction leakage current in reverse bias, we minimize such problems.

Errors can also be introduced due to variation in the depletion region width across the device. However, we believe such errors do not effect our data. We can demonstrate this with a simple calculation. For an n-doped layer with a density of approximately $N_D = 5 \times 10^{18} \text{ cm}^{-3}$ free electrons brought into contact with a p-type region with a free hole concentration of $N_A = 10^{15} \text{ cm}^{-3}$, we can calculate the penetration of the depletion region into the n-type layer:

$$d = \sqrt{\frac{2\epsilon\epsilon_0}{q} \frac{N_A}{N_D(N_A + N_D)} V} \quad (5.7)$$

where ϵ is the relative permittivity, ϵ_0 is the permittivity of free space, q is the elementary charge, V is the difference in potential across the junction (including the internal potential of the junction), and N_A and N_D were defined above. For a potential difference on the order of 1 V, we obtain a depletion into the n-doped region of $d \approx 0.2$ nm, or less than

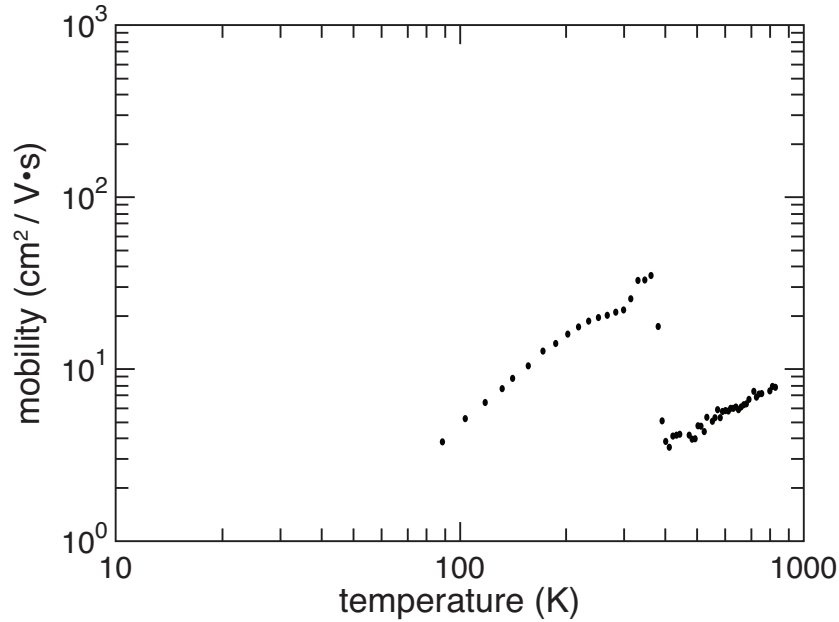


Figure 5.8: Although the Hall mobility demonstrates the same discontinuity in around $T = 355$ K as the conductivity and sheet carrier concentration, it shows that fs-laser doped silicon has a room temperature Hall mobility close to that of a crystalline sample.

one atomic layer. This calculation is valid over the entire measured temperature range for which we observe rectification. Thus we can neglect depletion effects.

Finally, there is the disordered nature of the laser-doped region to consider. Transmission electron microscopy and selected area diffraction indicates that a layer extending 100 nm from the surface of the silicon wafer is highly polycrystalline, with a grain size less than 50 nm [66, 69]. Hall effect data measured in such a polycrystalline system must be considered carefully. As discussed in more detail in references [113] and [132], the grain boundaries in polycrystalline systems can have a significant impact on transport properties. For example, there can be an accumulation of amorphous material, dangling bonds, and trap states in the intergrain region. In the cases of dangling bonds and traps, these can deplete carriers inside the grain and cause a reduction in the measured carrier concentration; this effect has an exponential temperature dependence. If the grains are populated with

a significant fraction of amorphous material, even stranger phenomena can occur, such as anomalous changes in the sign of the Hall coefficient [132]. However, we do not observe any of these types of behavior below the $T_{trans} = 355$ K. There is a small increase in the apparent sheet carrier density as we cool down (from $4.2 \times 10^{13} \text{ cm}^{-3}$ just below room temperature to $5.8 \times 10^{13} \text{ cm}^{-3}$ at $T = 90$ K). There are a number of possible explanations for this, including a change in the Hall scattering factor r_H , or the presence of impurity band conduction [19] yielding a minimum in the carrier concentration. However, all of these imply that, to first order, we are indeed measuring the properties of the crystal grain rather than the properties of the boundary. Additionally, given that there are approximately 10^{20} cm^{-3} sulfur atoms in the laser doped region, the magnitude of the room temperature carrier mobility ($22 \text{ cm}^2/\text{V}\cdot\text{s}$) is comparable to published values of crystalline silicon ($100 \text{ cm}^2/\text{V}\cdot\text{s}$) [133], and much higher than typical microcrystalline films even ($< 2 \text{ cm}^2/\text{V}\cdot\text{s}$ [135]) suggesting grains do not play an overwhelming role in transport.

5.6 Conclusion

We have explored a variety of phenomena in silicon doped with sulfur using femtosecond laser irradiation to a concentration above the critical concentration for a Mott transition. We have demonstrated that a rectifying junction exists for $T \leq 355$ K between the laser-doped region and a p-type substrate that allows us to isolate the laser-doped region for Hall effect measurements. The laser-doped region exhibits n-type conduction, but the carrier concentration is nearly insensitive to changes in temperature. This observation is consistent with a transition to metallic transport. We have investigated the location of the Fermi level by inspecting the current-voltage properties of fs-laser doped silicon with a variety of silicon substrates; results indicate the Fermi level is pinned in the same vicinity as

many of the well-known sulfur states. These observations are consistent with the formation of an metallic-like impurity band, but further work, especially information regarding optical absorption at sub-band gap photon energies, should be considered in the future.

5.7 Acknowledgements

Several people contributed to the work described in this chapter. The author conceived the experiments, prepared many of the samples, conducted the temperature dependent measurements, and analyzed the data. Meng-Ju Sher prepared many samples as well, performed the room temperature $I - V$ measurements, and contributed to the analysis. A. Asenbaum of the University of Salzburg performed the FTIR measurements that follow at the end of the chapter. The work was funded under the NSF-CBET program (contract CBET-0754227). The author acknowledges support from the NSF Graduate Research Fellowship program.

5.8 Layer isolation using Silicon-On-Insulator (SOI) wafers

Hall measurements that employ a rectifying junction for layer isolation have several complications [111]. To get a sense of whether such factors were complicating the measurements described above, in which we employed the rectifying junction between fs-laser doped S:Si and a p-type $1 - 20 \Omega\cdot\text{cm}$ substrate to isolate the laser doped region, we performed the same experiment using SOI wafers. Although the results and the interpretation are the same, likely because of the relatively thick device layer we used ($2 \mu\text{m}$), we accumulated expertise in handling and irradiating such substrates. We document it here for future experimenters.

5.8.1 Structural considerations when fs-laser doping an SOI wafer

The basic structure of an SOI wafer is shown in Figure 5.9. A crystalline layer of thickness d_{dev} , known as the device layer, sits atop a thermal SiO_2 layer of thickness d_{ox} . Underneath this insulating oxide is a bulk crystalline silicon substrate, called the handle, which has a thickness of many hundreds of microns. Also shown in Figure 5.9 is an SEM image of the cross section of such a wafer. We see that it is quite straightforward to use simple SEM imaging to identify the oxide layer. Chemical data from Energy Dispersive X-ray (EDX) spectroscopy (inset) confirms that the contrast in SEM image corresponds to the three layers of the SOI wafer. We obtained SOI wafers⁴ with an undoped device layer ($\rho > 10,000 \Omega\cdot\text{cm}$, thickness $d_{dev} = 2 \mu\text{m}$) and a buried oxide (thickness $d_{ox} = 0.5 \mu\text{m}$).

Our goal in using an SOI wafer is to more thoroughly isolate the laser-doped region, avoiding reliance on the rectifying junction which may fail at elevated temperatures. Thus,

⁴We used Ultrasil as a vendor; they produce so-called bonded SOI wafers, in which a thermal oxide is grown on two wafers, after which they are pushed together at high temperatures. The oxides fuse, and one of the two wafers is ground, etched, and polished to the desired device layer thickness d_{dev} . These types of SOI wafers are limited to $d_{dev} > 1 \mu\text{m}$. Other SOI technology exists that can get $d_{dev} < 100 \text{ nm}$, but bonded wafers are far less expensive.

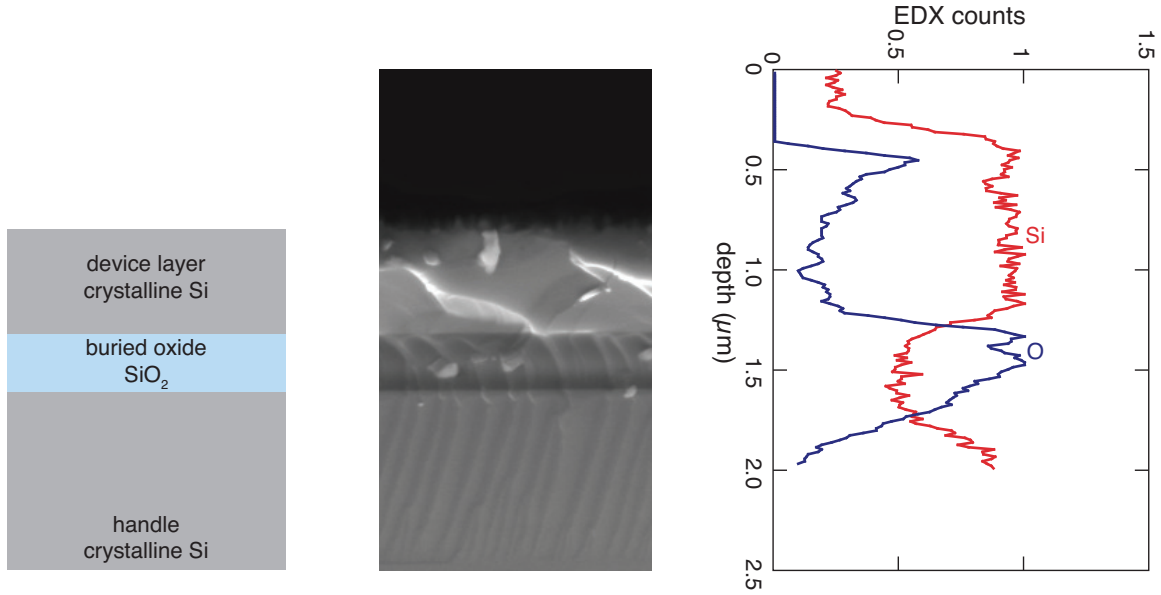


Figure 5.9: *Left:* Silicon-on-insulator wafers are formed with a thin device layer of crystalline silicon, separated from a thick crystalline substrate by a thin buried oxide. *Middle:* Electron microscopy reveals contrast that is indicative of the chemical differences in these three layers. *Right:* Energy dispersive x-ray spectroscopy (EDX) measurements confirm the interpretation of SEM imaging.

we wish to choose d_{dev} such that it is as small as possible. However, because morphology often develops when using many laser pulses to dope, d_{dev} cannot get too small, lest we ablate the device layer all the way to the oxide in certain locations, thus creating “islands” of fs-laser doped silicon. Additionally, the presence of the oxide — especially as d_{dev} approaches the melt depth of the silicon, alters the thermal boundary conditions. The oxide acts as a thermal bottleneck because of its lower thermal conductivity relative to crystalline silicon, and changes the dependence of the morphology on laser parameters. Thus, we begin by determining the laser exposure parameters necessary to ensure the resulting sample has morphology suitable for a Hall measurement of the laser doped region.

We prepared samples in the same fashion as described in section 5.3, but varied the laser fluence and translation parameters to yield different values of $\pi w^2/\Delta_y \Delta_x$. We then diced the SOI wafers by scoring them (on the side opposite of that exposed to the

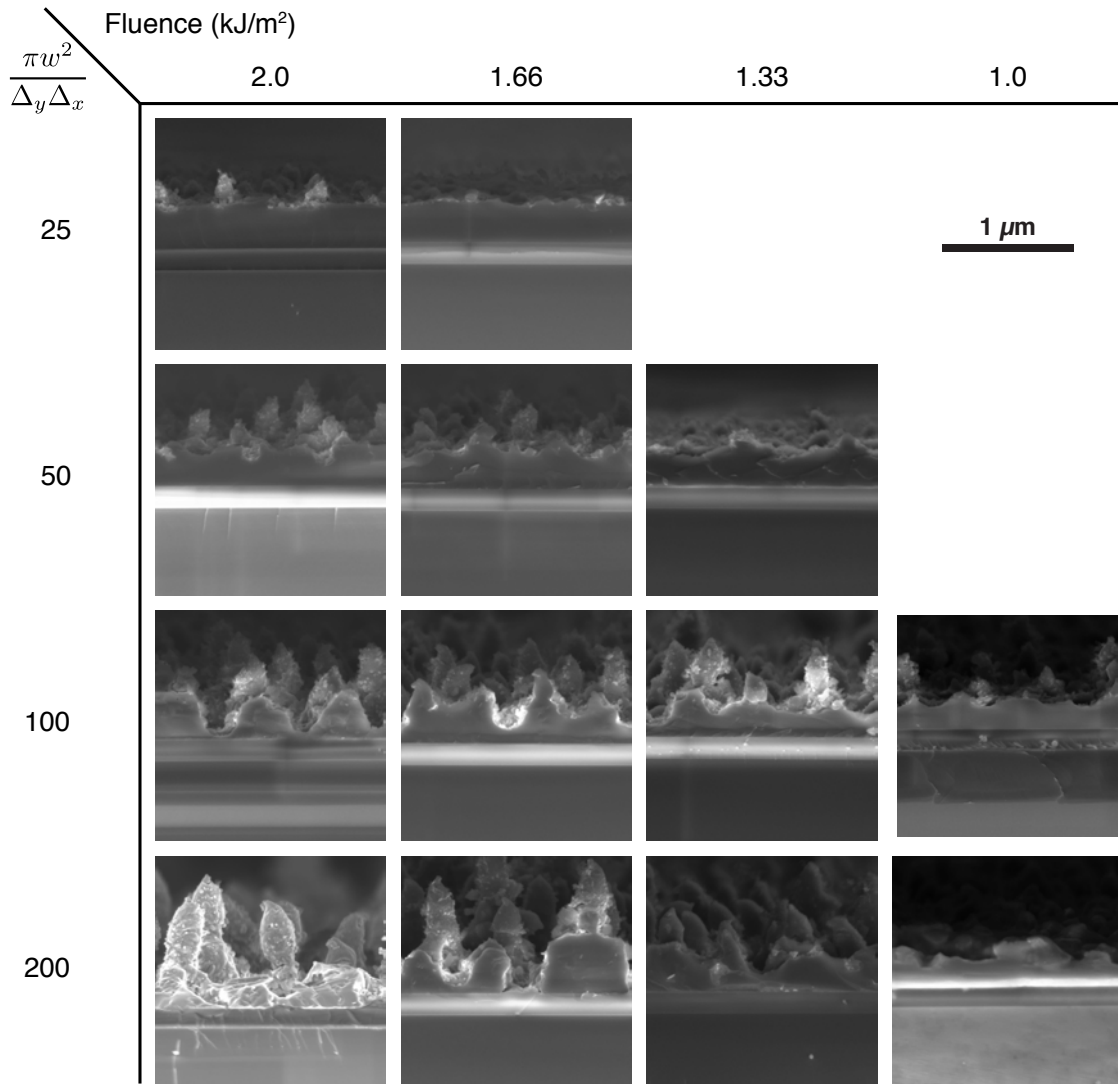


Figure 5.10: A cross-section of a 2 μm device layer doped with sulfur using a fs-laser. In this figure we explore a variety of exposure parameters.

laser) and imaged them in a scanning electron microscope. We used EDX spectroscopy to confirm that the contrast we observed in our images implied the chemical contrast for which we were looking. Figure 5.10 summarizes the results of a basic investigation of the effect of laser parameters on the resulting morphology. We see that even at relatively low intensity laser exposure (2 kJ/m², $\pi w^2/\Delta_y \Delta_x = 100$), we risk creating “islands” in our SOI wafer.

5.9 Extended optical absorption data on un-annealed samples

We close by recording the current status of ongoing optical absorption measurements regarding the low-energy cut-off of the sub-band gap absorption in fs-laser doped silicon. Using Fourier Transform Infrared spectroscopy (FTIR), we find that absorption extends to photon energies lower than 0.3 eV in fs-laser doped S:Si. We have currently only measured samples directly after laser-doping, and prior to thermal annealing. Thus, although this correlates well to the data reported above regarding Fermi-level pinning in the same vicinity, we cannot state with confidence that the two datasets are describing the same sulfur states, and we report it here only as a postscript to the data described above.

Following the same sample preparation outlined in section 5.3, we prepare samples doped to high concentrations of sulfur via fs-laser doping. We measure the optical properties of a non-annealed sample using two instruments. For photon energies between 0.5 – 5.0 eV, we use a UV-VIS-NIR spectrophotometer to measure transmittance and reflectance. The spectrophotometer is equipped with an integrating sphere for measurement of diffuse reflectance. For photon energies between 0.08 and 0.6 eV, we use a Fourier Transform Infrared spectrometer (FTIR), also equipped with an integrating sphere. With both devices, we measure reflectance R and transmittance T . Absorptance is then calculated as $A = 1 - R - T$.

In Figure 5.11 we plot the optical absorptance ($A = 1 - T - R$) of an unannealed, laser-doped silicon wafer. Data at the high energy end of the spectrum are from the UV-VIS-NIR spectrophotometer, while data at the low energy end of the spectrum are from the FTIR. This behavior is roughly independent of the parameters of the substrate. There is an 8% mismatch where the two data overlap, due to the difficulties of calibrating the

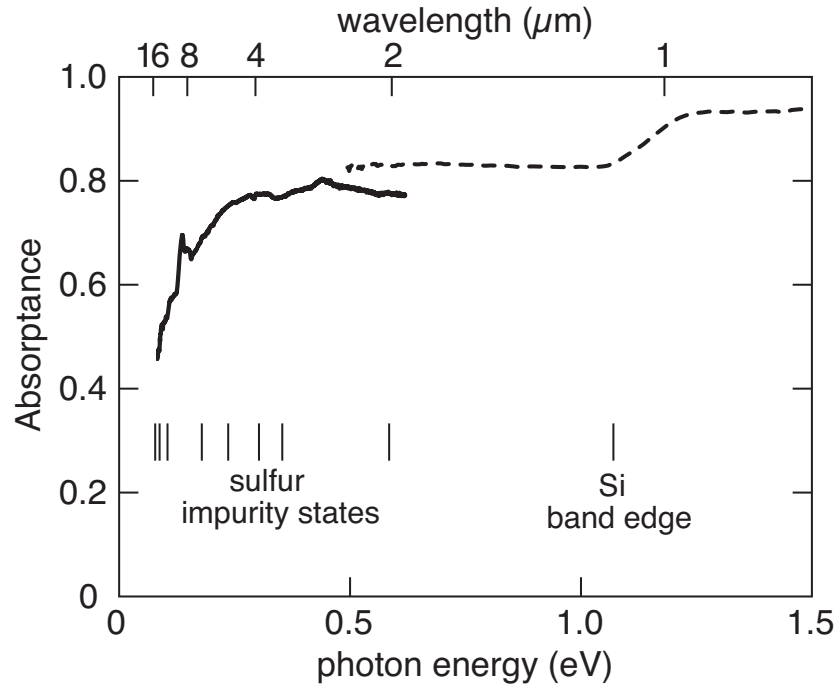


Figure 5.11: The absorption spectrum of black silicon from 0.080 eV to 1.5 eV. Note that the primary x-axis is energy, with wavelength marked on the top axis for reference. The dashed curve is the previous result; solid curve is the new data. Also shown on the plot are the positions of the silicon band gap ($E_g \approx 1.12$ eV), as well as known energy sulfur states in silicon, measured as $E_c - E_S$.

integrated reflectance measurement. The sample exhibits broadband infrared absorptance for photon energies as low as $E = 0.25$ eV; below this energy the absorption rapidly rolls off. We observe a small resonance at 140 meV, which corresponds to the well-known oxygen A-center absorption line [136], and we disregard it for our analysis.

Due to thermal broadening, it is difficult to interpret the absorption data as arising from a particular resonance. We know that the absorption we observe must fundamentally arise from the introduction of available electronic transitions into the silicon band structure that couple to photons with energy as low as 300 meV. Because the band gap of silicon is 1.1 eV, these states must be introduced within the band gap of silicon. Sulfur is known to introduce donor states located in the upper half of silicon's band gap that have energies

appropriate to account for the observed optical absorption; we show these states schematically in Figure 5.11 [129, 130]. We speculate that a high density of such states, present in the laser-doped region, is responsible. In the future, we plan to probe this behavior at low temperature and lower sulfur concentrations in an attempt to reduce thermal broadening and learn more about the specific transition energy for infrared absorption.

The samples shown in Figure 5.11 have not been thermally annealed, whereas the electrical measurements we describe above were carried out on samples annealed to 975 K for 30 min. Thermal annealing reduces the infrared absorption, and is also required for observation of a diode when doping with sulfur. Thus, it is possible that the predominant sulfur state changes during annealing, and the optical data is not directly comparable to the electronic data we report. However, as apparent in Figure 2.11, even at these annealing temperatures, significant sub-bandgap absorption persists to photon energies as low as 0.5 eV. Future measurements are necessary to determine absorptance at lower photon energies also persists, and especially to determine if the low-energy cutoff is the same after annealing. If so, such optical data would strongly support our conclusions above, based entirely on electronic data, that sulfur dopants introduce a high density of states 250–300 meV below the conduction band edge that exhibit behavior consistent with an impurity band.

Chapter 6

Silicon doped with sulfur via laser-induced melting and rapid solidification

In the previous two chapters, we have explored significant new findings regarding silicon doped to non-equilibrium chalcogen concentrations using femtosecond laser pulses. In many regards, however, our analysis has been complicated by the lack of a high degree of crystalline order in the samples. In this chapter we describe measurements made on silicon doped to comparable concentrations using an altogether different technique: ion implantation followed by pulsed laser melting and crystal regrowth. This material system offers the advantages of a highly crystalline and well-studied physical structure; it exhibits similar optical absorption of photons with energy less than the band gap of silicon. In this chapter, we focus on understanding the experimental issues involved with measurement, as well take a first step toward extracting information from temperature-dependent transport data in this rich and complex material system. We identify the ionization energy of the

sulfur donors introduced at low sulfur implant dose to be $E_d = 117 \pm 2$ meV. We also report, to the author's knowledge, the first observation of a sulfur-driven metal-insulator transition in silicon; we find the critical concentration necessary for a sulfur-driven transition to metallic conduction to be $n_{crit} \approx 10^{19}$ cm⁻³.

6.1 Introduction

Silicon manifests several intriguing optoelectronic properties when it is doped with sulfur above the solubility limit, including absorption of photons with energy less than the band gap [49,53,65], donor activity by the sulfur [50,71], and photodiode response at photon energies as low as 0.8 eV [71]. Such effects were first reported as a result of a femtosecond laser implantation process; however, the laser process significantly disrupts the crystal structure in the doped region, resulting in a sub-micron crystalline grain structure [66] that complicates the interpretation of many traditional electronic transport measurements [113].

Ion implantation followed by pulsed laser melting and crystalline re-growth is an established method to obtain dopant concentrations well above the solid solubility limit, while retaining the crystalline order of the pre-implanted substrate [43]. These highly non-equilibrium dopant concentrations are achieved via a process known as solute trapping, a phenomenon in which the resolidification front moves through the molten silicon slow enough for solidification to be epitaxial, but fast enough that the dopant atoms cannot diffuse away from the interface quickly enough to establish equilibrium solid concentrations. Predictive models of this phenomenon exist [45] that have been tested in a number of material systems [46,47,137].

Specifically, ion implantation and pulsed laser melting have been well-studied for sulfur in silicon (S:Si): the implantation parameters [138], the crystal structure [50], and sul-

fur concentration profile [49] are well-documented. In addition, because dose is easily varied using an ion-implantation process, it is possible to study the properties of this material as we transition from equilibrium sulfur concentrations for which no anomalous optical properties are observed, to non-equilibrium concentrations at which the doped layer absorbs photons with energy less than the band gap. In this chapter, we describe temperature-dependent measurements of the Hall effect and resistivity in such systems. Our goal is to characterize the nature of conduction in S:Si, extract information regarding the electronic states that sulfur introduces into the silicon band structure, and speculate on role of metal-insulator transitions in the optical and electronic properties of S:Si.

6.1.1 Details of S:Si

In this section we reproduce, for the readers benefit, previous results by the Aziz group on sulfur in silicon via ion implantation. The purpose of this chapter is not to discuss the ion implantation process or pulsed laser melting process; the reader is referred to references for that information [49, 50]. Here we summarize only the pertinent points for this chapter. After ion-implantation and pulsed laser melting, sulfur is distributed in a relatively uniform fashion in a layer that extends 400 nm from the surface of the wafer. The doped region is a single crystal, free of extended defects. Figure 6.1 illustrates these facts.

At high sulfur doses (10^{16} cm⁻²), the sulfur dopants act as electron donors and form a rectifying junction with the substrate immediately following pulsed laser melting [50]. We will assume that lower doses do the same, an assumption that our experiments with silicon-on-insulator wafers will show are merited. Similar to fs-laser doped silicon, the high sulfur concentration leads to anomalously high infrared absorption, which is characterized by featureless absorption from the band edge to photon energies as low as 0.5 eV. The Aziz

group has estimated the absorption coefficient to be as high as $2.3 \times 10^4 \text{ cm}^{-1}$ at optical wavelengths of 2300 nm. Similar to fs-laser doped silicon, annealing leads to a reduction in the sub-band gap infrared absorption.

6.2 Experimental setup

In all experiments described below, a lightly p-type (boron doped, $\approx 25 \text{ } \Omega \cdot \text{cm}$) silicon region is ion implanted commercially; the specific dose varies for certain experiments. All samples are implanted using a sulfur ion energy of 95 keV; for sulfur doses below $3 \times 10^{15} \text{ cm}^{-2}$, the sulfur implant is preceded by a silicon implant of $3 \times 10^{15} \text{ cm}^{-2}$ at energies of 85 keV so that all samples have similar amorphous regions before laser-exposure. Table 6.1 outlines the doses for the samples on which we report in this chapter. The doped region is amorphized by the implantation, and crystal order is re-established using the pulsed laser melting (PLM) method (performed by the Aziz group). The process is described in detail for this experimental system elsewhere [49, 50]. We prepared a selection of samples representing different dose and annealing conditions. For most of the measurements we report here, a single crystal silicon wafer is used; however, we report on one sample for which the implanted region is the device layer of a silicon-on-insulator (SOI) wafer (device layer depth 260 nm, implantation depth 200 nm, PLM melt depth approximately 230 nm). The parameters of the samples that we measured are represented in Table 6.1

After receiving samples from the Aziz group, they are ultrasonically cleaned in successive solutions of acetone, methanol, and isopropanol. In some cases, a brief etch in dilute (5%) hydrofluoric acid is necessary to remove a surface oxide that prevented adhesion of photoresist. As received, the PLM area is a square with edge lengths of approximately 2.5 mm. In order to create samples of repeatable dimensions, as well as prevent leakage through

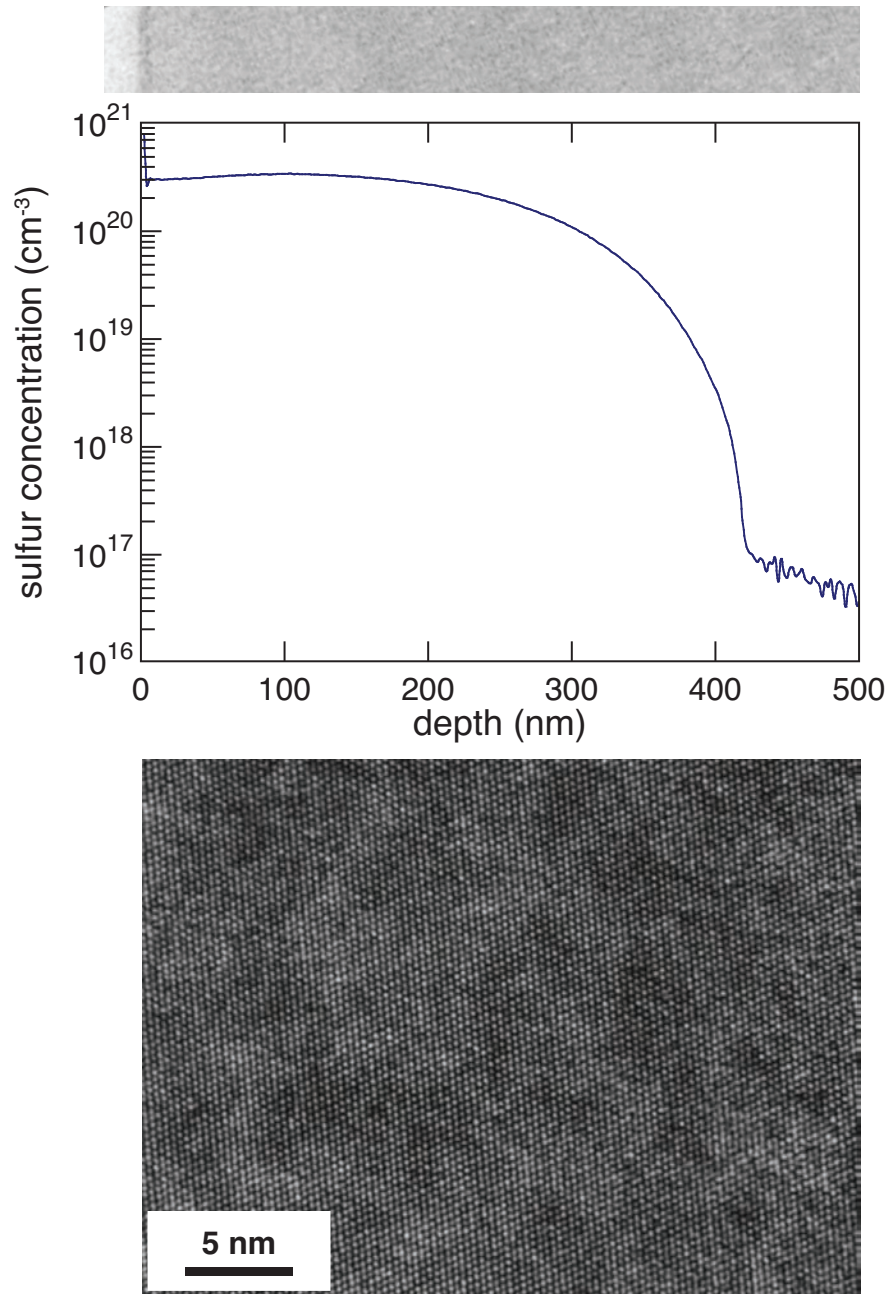


Figure 6.1: Properties of silicon implanted with a sulfur dose of 10^{16} cm^{-2} and subsequently pulsed-laser melted with 4 nanosecond laser pulses. *Top:* Sulfur concentration obtained via SIMS after pulsed-laser melting; bright-field TEM atop the graph demonstrates continuous single crystal into the un-implanted substrate. *Bottom:* High resolution TEM demonstrates the high quality of the implanted region. Data was obtained by the Aziz group; TEM from reference [50], SIMS data via private communication.

Dose (cm^{-2})	Anneal temperature (K)					
	–	425	475	525	575	625
1×10^{13}	×					
3×10^{13}	×					
1×10^{14}	SOI					
3×10^{14}	×					
3×10^{15}	×					
1×10^{16}	×	×	×	×	×	×

Table 6.1: Enumeration of the samples that are reported on in this chapter. Except for the one exception marked as such in the table, all samples were sulfur implanted into a lightly p-type silicon substrate. The “SOI” sample was implanted into an SOI wafer. All samples are implanted using an ion energy of 95 keV; for sulfur doses below $3 \times 10^{15} \text{ cm}^{-2}$, the sulfur implant is preceded by a silicon implant of $3 \times 10^{15} \text{ cm}^{-2}$ at energies of 85 keV.

the surrounding implanted (but still amorphous) regions, a smaller ($2 \times 2 \text{ mm}$) region is masked within the PLM area using standard positive photoresist, and the surrounding area is etched to at least $1 \mu\text{m}$ depth using a reactive ion etch. The masked region is a standard van der Pauw geometry, either square or cloverleaf in shape. Sample geometry is detailed along with specific results in Figures 6.2 and 6.3.

A subsequent photoresist mask is employed for metallization of contacts (Ti–Ni–Ag, 20–20–200 nm) in the corners of the samples. In the case of the square geometry, right-triangular contacts are placed in each corner of the sample (oriented with two edges of the triangular contact parallel with the sample edges); for the clover-leaf geometry, small circular contacts are placed near the edge of each quadrant of the cloverleaf. In the case of the square, contacts are placed no farther than $5 \mu\text{m}$ from a side, and extend no farther than $30 \mu\text{m}$ from a corner, in order to minimize errors due to contact placement. We estimate errors from contact placement to be less than 1% for the square samples; such errors are negligible for the clover-leaf samples [117].

The quality of our contacts, combined with the doping level of the samples, de-

termines the minimum measurable temperature. For samples with a sulfur dose of 10^{16} cm^{-2} , the contact metallurgy is sufficient to temperatures as low as $T = 10$ K. However, at lower doses, contact resistance limits the minimum temperature of measurement; in the case of the lowest doses, we can only measure at temperatures $T > 100$ K. Improving the performance of the contacts at low temperature will be a priority in future experiments.

After metallization, samples are mounted onto chip carriers; using Al wire bonds, we connect the sample contacts to large area contacts on the chip carrier. The carriers are mounted on a cold finger in a closed cycle helium cryostat which is capable bringing the sample to temperatures $10 \text{ K} < T < 800 \text{ K}$. Standard techniques are used to measure the resistivity [115] and the Hall effect [109]. The lowest measurable temperature is sometimes higher than 10 K due to the quality of our contacts. We begin measurements at the lowest measurable temperature, and proceed with measurements at progressively higher sample temperatures. We calculate the sheet carrier concentration and Hall mobility using:

$$n_s = r_H \frac{I_e B}{q V_{Hall}} \quad (6.1)$$

$$\mu_{Hall} = (q \rho_s n_s)^{-1}, \quad (6.2)$$

where I_e is the exciting current, B is the magnetic field, q is the elementary charge, and V_{Hall} is the measured Hall voltage. We make the approximation that the Hall scattering factor $r_H = 1$, which we expect introduces an error on order unity [107]; this error was discussed in detail in chapter 3. For Hall effect measurements, the samples are immersed in a magnetic field of 0.65 T; we excite samples with the minimum current necessary to achieve signals greater than $10 \mu\text{V}$. We observe no self-heating effects.

6.3 Results

In Figure 6.2, we show the sheet carrier concentration n_s , Hall mobility μ_H , sheet resistivity ρ_s , and sample geometry for PLM samples of increasing dose; we did not anneal these sample. We observe that n_s , which has a negative sign at all temperatures, generally increases monotonically for all samples with increasing temperature. The sample with the highest sulfur dose (10^{16} cm^{-2}), however, goes through a soft minimum near room temperature. In general, higher doses yield a larger n_s at all temperatures, although the samples implanted with a sulfur dose of $3 \times 10^{14} \text{ cm}^{-2}$ exhibits comparable behavior to the sample with the sample with dose $3 \times 10^{13} \text{ cm}^{-2}$. Below $1000T^{-1} \approx 2.5 \text{ K}^{-1}$, n_s exhibits an identical and significantly increased slope with decreasing T^{-1} for all samples. As we will show below, careful analysis of this behavior indicates that we are measuring the intrinsic carrier concentration in this regime, and that the data are probably contaminated by the substrate. Thus, we cut off all other data sets below $1000T^{-1} \approx 2.5 \text{ K}^{-1}$ ($T > 400 \text{ K}$). Also in Figure 6.2, the sheet resistivity indicates a steep increase in resistivity with decreasing temperature for samples with low sulfur doses. At a dose of $3 \times 10^{15} \text{ cm}^{-2}$ this slope is much more gradual, and at a higher dose of 10^{16} cm^{-2} the resistivity shows very little slope with decreasing temperature. Resistivity decreases monotonically with dose at all temperatures.

In Figure 6.3, we show the sheet carrier concentration n_s , Hall mobility μ_H , sheet resistivity ρ_s , and sample geometry for PLM samples of increasing anneal temperature (all with a sulfur dose of 10^{16} cm^{-2}). We note here that all samples are effectively annealed to 425 K during the fabrication process due to exposure to hot plates and etching processes. We observe that n_s , which has a negative sign at all temperatures, is relatively insensitive to temperature. All samples, though, do show a soft minimum near room temperature. With increasing anneal temperature, n_s increases at all measured temperatures. Sheet

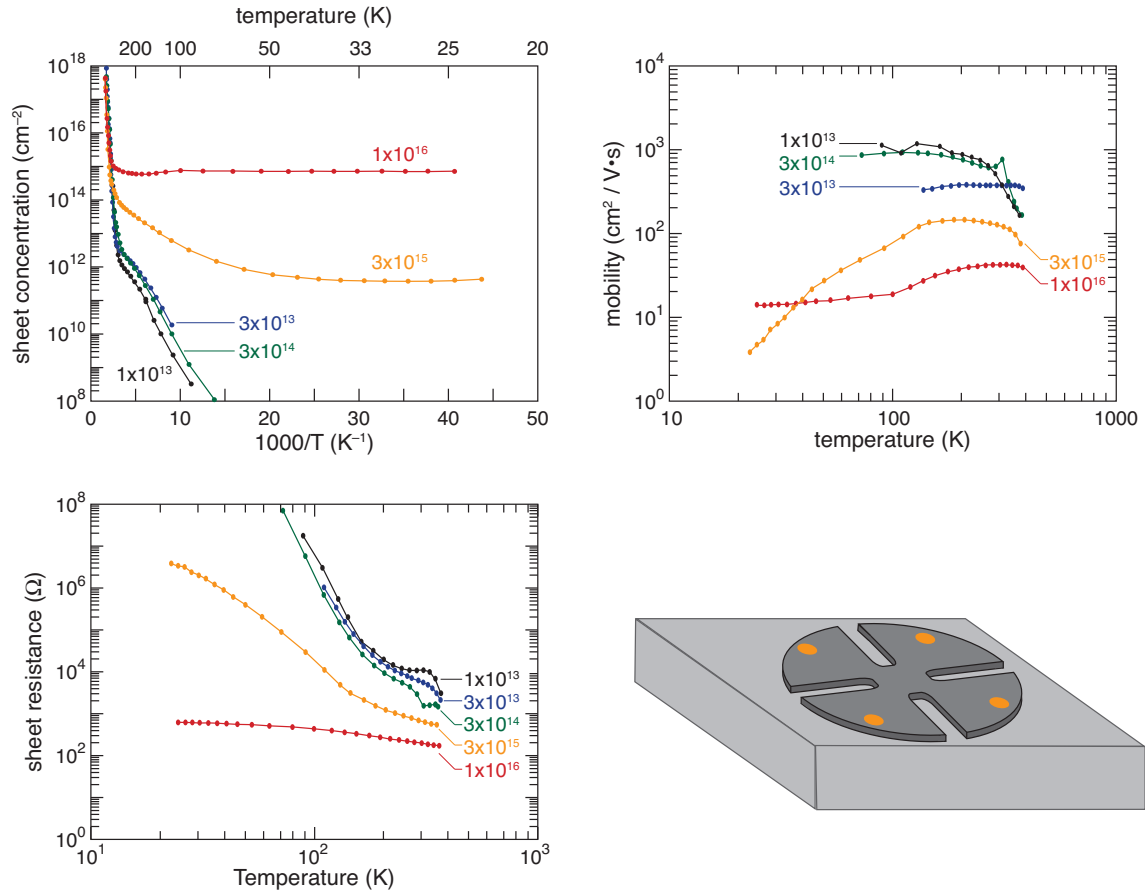


Figure 6.2: Temperature dependence of electronic transport properties for un-annealed samples of increasing sulfur dose. We show (*top left*) sheet carrier concentration versus inverse temperature, the sign of the charge carrier is negative at all temperatures; (*top right*) Hall mobility versus temperature; (*bottom right*) sample geometry; and (*bottom left*) sheet resistivity versus temperature. Lines are only to guide the eye.

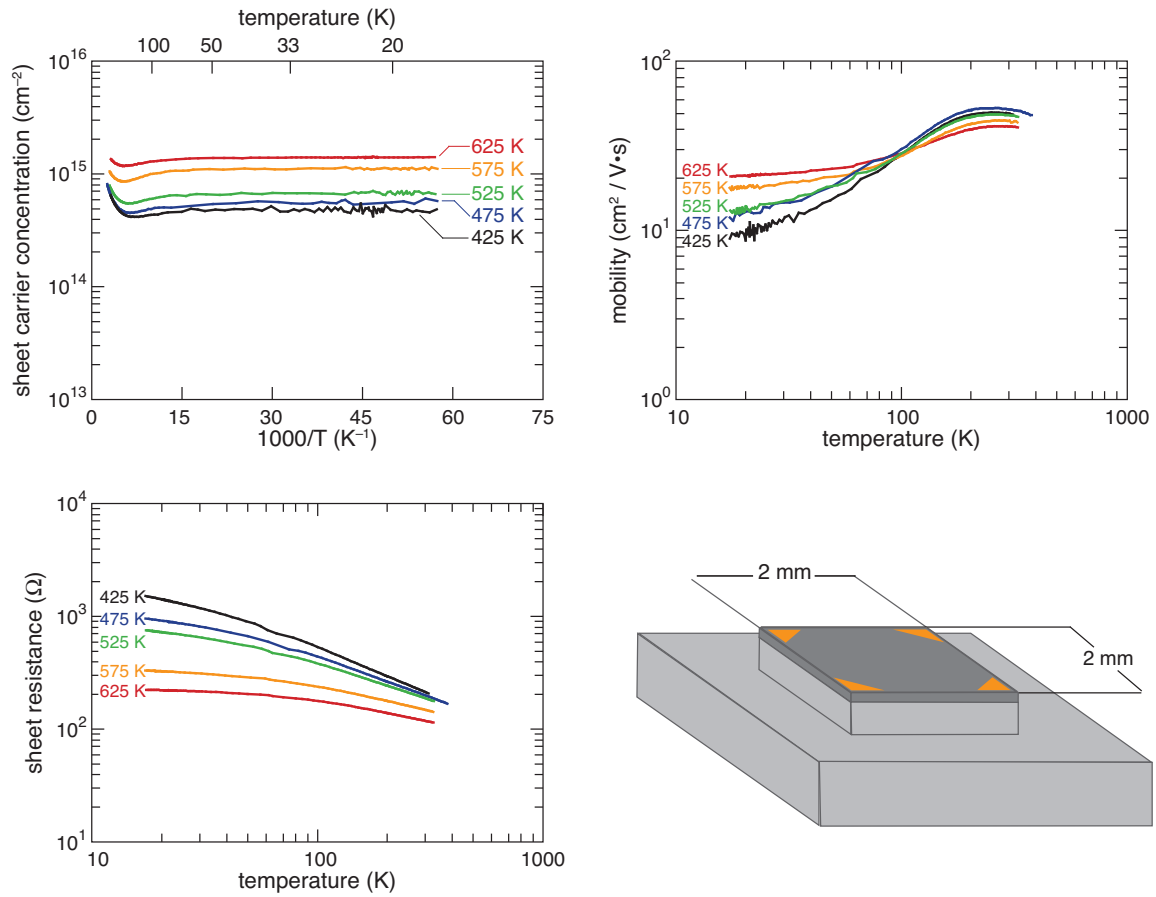


Figure 6.3: Temperature dependence of electronic transport properties with sample annealing for sulfur dose of 10^{16} cm^{-2} ; here we show (*top left*) sheet carrier concentration versus inverse temperature, the sign of the charge carrier is negative at all temperatures; (*top right*) Hall mobility versus temperature; (*bottom right*) sample geometry; and (*bottom left*) sheet resistivity versus temperature. For these plots, sampling was fine enough that plotted points merged into lines in almost all temperature regimes.

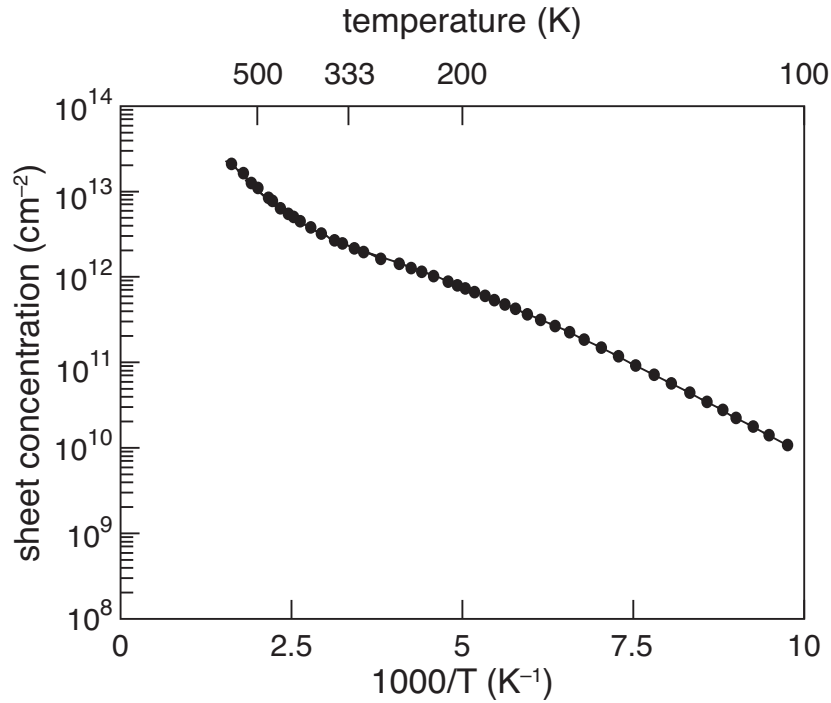


Figure 6.4: Temperature dependence of sheet carrier concentration for a silicon on insulator (SOI) silicon wafer implanted with 10^{14} cm^{-2} sulfur atoms. The sign of the charge carrier is negative at all temperatures. Line is to guide the eye.

resistivity ρ_s exhibits slightly more temperature dependence, with a slight and monotonic decrease as temperature increases. Additionally, resistivity decreases with higher annealing temperature at all measured sample temperatures. The Hall mobility, also shown in Figure 6.3, increases with increasing measurement temperature until going through a maximum near room temperature for all samples. Interestingly, mobility *decreases* in samples annealed at higher temperatures when we measure it at room temperature, but *increases* for the samples annealed at higher temperatures when we measure it near $T = 10 \text{ K}$.

Finally, in Figure 6.4, we plot the sheet carrier concentration of an SOI wafer implanted with a 10^{14} cm^{-2} dose of sulfur. We observe that the sheet carrier concentration n_s increases monotonically with decreasing T^{-1} . Two distinct slopes are evident, one each in the high and low temperature regimes.

6.4 Discussion

Three aspects of the data will be discussed in detail in this chapter. We will first discuss the impact of the sample structure on the result of transport measurements. Second, we will discuss what we can learn from the samples we have measured regarding the energy states introduced by the implanted sulfur. Finally, we will speculate to the extent that the data allow us on the nature of charge transport and discuss what conclusions we can draw, if any, regarding the presence of an impurity band.

6.4.1 Diode-isolation of the implanted layer

For all data presented in Figures 6.2 and 6.3, we are relying upon the rectifying junction between sulfur implanted layer and the p-type substrate to electrically isolate the sulfur-doped region. A pre-requisite to any discussion of experimental data is to determine the extent to which this condition obtains in our experimental measurements. We begin with a discussion of where it demonstrably does not.

High temperature isolation

Perhaps the most striking feature in the behavior of n_s for all the samples represented in Figures 6.2 and 6.3 is the sharp increase in slope with decreasing T^{-1} near $1000T^{-1} \approx 2 - 2.5 \text{ K}^{-1}$ (temperatures $T > 400 \text{ K}$). This slope is less obvious for the samples represented in Figure 6.3, as the highest temperature measured was $T = 500 \text{ K}$, but it is still apparent. We will argue that this region of increased slope arises due to an unavoidable breakdown in the isolating junction as the substrate enters an intrinsic conduction regime. This transition introduces large errors into the measurement of the Hall voltage, and the subsequent calculation of the sheet carrier concentration. Because of these errors, we will neglect this high-temperature data.

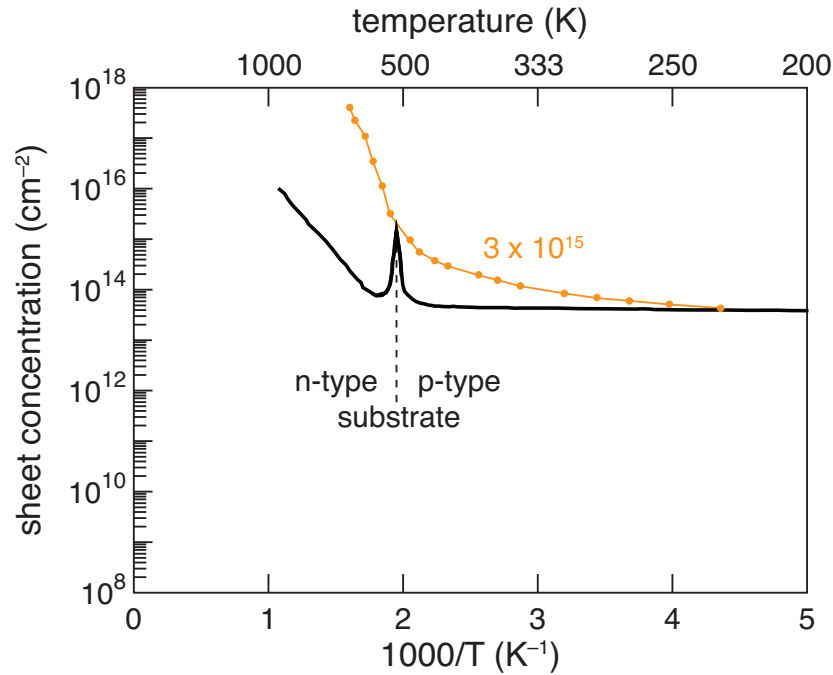


Figure 6.5: A detailed view of the sheet carrier for one of the samples shown in Figure 6.2 along with a wafer comparable the substrate on which it was fabricated.

In Figure 6.5, we show in detail what occurs near this transition, and we also show the behavior of a similar p-type $1 - 20 \Omega\text{-cm}$ substrate. For the substrate, we observe a small singularity in the sheet carrier concentration near $T = 500 \text{ K}$; for lower temperatures the sign of the majority charge carrier is positive, as expected for a p-type substrate. For higher temperatures (smaller T^{-1}), the majority carrier is of a negative sign and the carrier concentration is steeply dependent on T^{-1} . These observations indicate a transition to intrinsic conduction; indeed, the slope in this regime can be analyzed to yield the band gap of the material, as predicted by crystalline semiconductor statistics [114]. With this transition to intrinsic conduction, the Fermi level moves into the upper half of the conduction band and into the vicinity of the Fermi level in the sulfur doped layer. As we discussed in detail in section 5.5, as the difference in Fermi level on opposite sides of a junction becomes small, rectification is no longer possible.

As the junction between the sulfur-doped region and the p-type substrate ceases to rectify, the current with which we excite the sample will begin to distribute itself between the sulfur-rich region and the substrate. The distribution of current will occur according to simple circuit laws, with the sulfur-doped region in parallel with the substrate. As we mentioned above, the breakdown of the rectifying junction arises from a transition to intrinsic carrier excitation; in this regime, the sulfur-doped region and the substrate will possess carrier concentrations that grow exponentially similar with increasing temperature. Because the substrate is substantially thicker than the sulfur-rich region ($d_{substrate} \approx 1000d_{sulfur}$), its resistance at these temperature will be lower and the current will be distributed with increasing preference to the substrate. Because of this transition, the sheet carrier density — the product of carrier density in the measured region with layer thickness of the measured region — will increase even faster than we might expect as we begin to probe the substantially thicker substrate region. The resistance of the junction, however, does not abruptly go to zero at a particular temperature, and thus the precise calculation of the current distribution is not practical — as it requires a detailed knowledge of the exact degree of isolation that the diode is providing, as well as the electrical characteristics that these measurements are designed to probe. We thus conclude only that the data in this high-temperature regime is not useful for the purposes of this chapter, and we neglect it in future considerations.

For the lower dose samples, the transition to this steep slope occurs at slightly lower temperatures ($T \approx 400$ K). Recalling section 3.3.4, this behavior should not surprise us. As we showed there, for a given temperature and donor level, decreasing the number of donors N_d forces the Fermi level to decrease as well in order to account for a greater fraction (of fewer donor electrons) to ionize. This lowering of the Fermi level means that the internal potential V_{int} will go to zero more quickly, keeping in mind that the substrate

Fermi level is increasing with temperature. Moreover, even in lieu of such arguments, we can determine that the steep slope of the carrier concentration with T^{-1} in this high temperature regime is not physical. Fitting n_s according to a simple formula for dopant activation:

$$n \propto e^{E_a/k_b T}, \quad (6.3)$$

yields an activation energy E_a of approximately 1 eV. This observation is actually apparent in Figure 6.5 without doing the fitting; the slope is obviously steeper than that of the intrinsic excitation of carriers in the substrate, which has an activation energy $E_a = E_g/2 \approx 0.55$ eV. The relationship between such activation energies and a donor energy is generally of the form $E_a \leq E_d$, implying that a potential donor binding energy E_d would have to be as large or larger than this value. Such deep donors are highly unlikely, as they have never been documented for sulfur; and even if they did exist, they should have an activation dependence of $E_d \geq 2E_a$, as is typical when compensating impurities do not play a role (the presence of a significant number of compensating impurities between such a deep level and the valence band is also unlikely). The failure of our rectifying junction is the only reasonable conclusion for this steep temperature dependence; thus we neglect any data near or above the temperatures of these steep slopes. We can thus conclude that rectification will not be a viable route of isolation for exploring the high temperature regime above $T \approx 400$ K. Low temperature measurements appear to achieve far superior isolation.

Although we have addressed the high temperature performance of the diode isolated samples, we must approach transport measurements performed on an SOI device layer with a critical eye as well. The structure of the SOI still includes a layer of undoped crystalline silicon underneath the sulfur-rich region that is approximately 20 – 40 nm thick. As a result, we are still relying on a rectifying diode to isolate the sulfur-rich region from

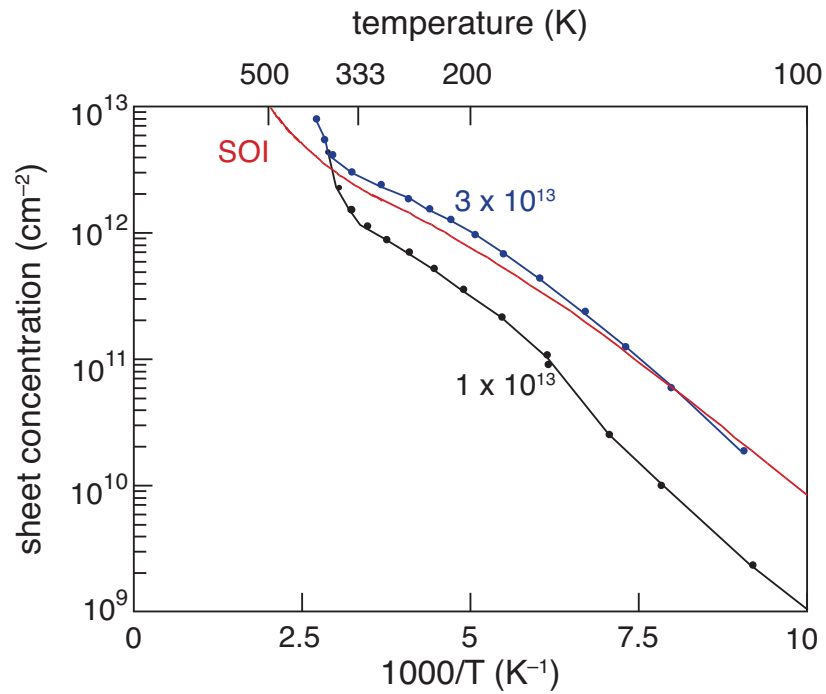


Figure 6.6: Detailed view of the sheet carrier concentration of an SOI wafer implanted with 10^{14} cm^{-2} along with comparable doses isolated via diodes.

this layer. As we can see in Figure 6.6, the behavior of n_s for the SOI implanted layer exhibits a significant change in curvature at precisely the temperature where the low-dose diode-isolated samples shift to the steep slope that we attribute to loss of the diode. The same arguments we made above regarding contamination by the substrate apply, and we must regard these data with equal skepticism.

Low temperature isolation

In Figure 6.6, we can inspect in detail the low temperature behavior of samples with a low sulfur dose compared to an SOI wafer with a comparable dose. Although these data appear to be in relatively good agreement, we can see that around $T = 200 \text{ K}$ there is a noticeable shift to lower concentrations that occurs in the diode-isolated samples but not in the SOI sample. This is far from the drastic deviations that occur at high

temperature (visible in the upper left of Figure 6.6), but are still of concern if our interest is in a high-resolution fit for the carrier binding energy. Because the samples have different substrate doping, the degree of compensation is likely different, which would explain the differences in this temperature range. Additionally, the implantation and laser exposure parameters are slightly different among these samples; thus it is also possible that the sulfur introduces different states, or different amounts of similar states. It is not possible to determine for certain the reason for the deviation based on these data alone. Indeed, it is possible that all of the samples, including the SOI, suffers from some contamination from the undoped crystalline region below the sulfur-rich region. As a result, we must approach the fitting we discuss below with caution. In the future, experiments must confirm the fit in an experimental geometry that entirely avoids the ambiguity introduced by an undoped crystalline layer adjacent to the sulfur-rich region. We will discuss the appropriate experimental approach for such confirmation below.

Contacts

We close our discussion of experimental concerns with a brief mention of contacts. To a great degree, measurements of the lower dose samples were hindered by the poor quality of the contacts. The high contact resistance lead to noisy measurements at all temperatures, and severely limited the most interesting low temperature measurement regime. In the future, either a better contact metallurgy, or a means to locally dope the surface in an n^+ fashion will be required.

6.4.2 Determining the binding energy of implanted sulfur at low doses

Given the ambiguities present in interpreting the carrier concentration data from diode-isolated samples, we will only attempt to analyze in detail the carrier concentration

data for the SOI implanted wafer. We view this fit as a first step, and as a reference point for future efforts with this material.

Beginning our fit, we must determine the degree, if any, of degeneracy in our measurements. As discussed in Chapter 3, the statistical description of charge carriers in semiconductors is made considerably easier if the Fermi level E_f remains far from the conduction band E_c throughout the temperature range of interest. As we discussed then, we can make this determination quite simply by ensuring the condition of equation 3.22 is met:

$$\frac{n(T)}{N_c(T)} \leq \mathcal{F}(\eta = -2) \approx 0.13.$$

The maximum value that we observe occurs near room temperature, where $n/N_c \approx 0.01$. This value corresponds to a reduced Fermi level $\eta \leq -4$. Thus, our system resides safely in the regime for which the non-degenerate approximation is valid. We can thus write $\mathcal{F}(\eta) \approx \exp(\eta)$, and the calculations required for fitting are made substantially less complex. Recalling the equations of section 3.3.3, our approach is made easier by the fact that we know a great deal about our samples: the electron effective mass m_e^* is known, and we can make an educated guess regarding the compensating impurity density N_A , as it should not differ significantly from the background boron concentration in the originally p-type SOI wafer. There is some ambiguity regarding the value that β , the spin degeneracy of the impurity level, but it can take only a limited number of values, as we also discussed in section 3.3.3. These considerations leave only N_d , and E_d as unknowns, although we leave N_A as a fitting variable. We will later consider the fitted value in comparison to the known substrate acceptor concentration as a indication of the quality of our fit.

We begin with a simple model for our system, in which we attempt to fit only the low temperature data. We will model the system as made of a single, monovalent species

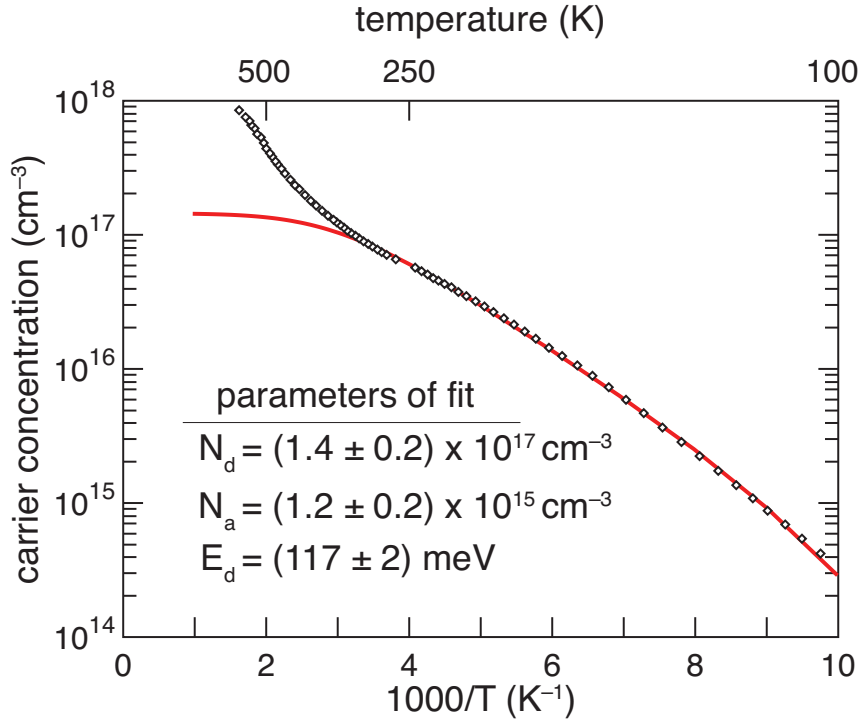


Figure 6.7: The data of Figure 6.4, shown with a fit to the data below room temperature. The fit is performed to equation 3.29. Uncertainties are derived by analyzing the sensitivity of the fit to the assumed layer thickness ($200 \text{ nm} < d < 250 \text{ nm}$) and upper temperature cutoff ($275 \text{ K} < T_{cutoff} < 325 \text{ K}$)

of electron donor. We approximate the sulfur dopants as being homogeneously distributed in the upper 240 nm of the SOI layer, and also assume that the doped region is perfectly isolated below $T = 400 \text{ K}$. We will address the impact of these assumptions below. Under this approximation scheme, our system is comfortably over-determined, and we can proceed to find a best fit (in a least-squares sense) for equation 3.29 to the data in Figure 6.4. The fit and its parameters are shown in Figure 6.7.

The quality of the fit is quite good. In addition to minimal deviation from the measured data in the temperature region of interest, we can compare the value of N_A generated by the best fit to the known boron acceptor density in the device layer prior to sulfur implantation. These boron dopants introduce compensating states near the valence

band edge, and their concentration N_B should be quite close to the density of compensating centers N_A . For the SOI wafer in this experiment, the device region of the SOI wafer was doped with boron in a range $0.6 \times 10^{15} \text{ cm}^{-3} < N_B < 1.1 \times 10^{15} \text{ cm}^{-3}$. Given that a small concentration of additional compensating impurities likely exist deeper in the gap, the value generated by our fit of $N_a = 1.2 \times 10^{15} \text{ cm}^{-3}$ compares quite well.

The value of N_d is particularly interesting; given a sulfur dose of 10^{14} cm^{-2} , a layer thickness $d = 240 \times 10^{-7} \text{ cm}$, and accounting for about half of the sulfur evaporating during the PLM process, we expect a total sulfur concentration of approximately $N_S = 2 \times 10^{18} \text{ cm}^{-3}$. Thus, our fit for $N_d = 1.4 \times 10^{17} \text{ cm}^{-3}$ indicates that roughly 90% of the sulfur in the device layer occupies a different state than the one we observe ionizing over the temperature range of our fit. If, due to the inhomogeneous sulfur profile, we are actually probing a *far* thinner layer than $d = 240 \text{ nm}$, this could account for the difference. Future work, such as successive Hall measurements interspersed with etching thin layers of the sample, could determine the depth profile of carrier concentration unambiguously [139, 140]. It is also possible, however, that the sulfur is distributed roughly as we have estimated, and the other 95% of sulfur atoms exists in deeper states that we have not excited.

The value for the binding energy of the sulfur electrons, $E_d = 117 \pm 2 \text{ meV}$, needs careful consideration. This value is comparable to the sulfur “A-center” that has previously been reported [127, 141]; some authors attribute this center to a neutral, isolated sulfur impurity of as-yet unknown structural coordination in the lattice. Other authors have argued that this center must be more complicated [129, 130]. Our fit indicates that it has a spin degeneracy $\beta = 1/2$, which is not consistent with an isolated double donor. Further investigation into this issue is merited, and data at lower temperatures – in the regime where $n \ll N_A \ll N_d$ would be particularly helpful. As we discussed in section 3.3.3, the slope of n vs. $1/T$ should change substantially here as we enter the compensation

dominated excitation regime. Our fit, if we extended to these temperatures, would predict a significant increase in the *rate* of donor freeze-out. Confirming this prediction would yield significantly more confidence in the fit.

We note in closing that we can proceed in a similar fashion with a fit that incorporates a second, deeper level that describes the higher temperature behavior. Such a fit can describe our data accurately, and yields a realistic deeper sulfur state with a binding energy near $E_d = 290$ meV, quite close to the well-known substitutional state of sulfur [129]. As we have previously discussed, though, it is unclear whether our data in the high temperature regime is contaminated by the substrate. Thus, at the current time we do not pursue a more sophisticated fit.

Impact of model assumptions

We now discuss the assumptions present in our model. First, we address the assumption that the sulfur is uniformly distributed in a layer of thickness 240 nm. The fit is not particularly sensitive to the thickness that we choose, with changes of $\pm 10\%$ yielding comparable changes in the fitted values for N_A and N_d , but changes of less than 1% in the fitted value of E_d . Thus, our assumption of layer thickness is not particularly important to the fit. The assumption of uniformity is difficult to address without further experimental efforts, involving repeated Hall measurements interspersed with etching of thin (≈ 5 nm) layers of the samples. Unfortunately, not even depth dependent structural and electrical measurements, such as SIMS and spreading resistance profiling, respectively, can resolve the depth dependence of carrier concentration and mobility unambiguously. Although the dopant distribution is not precisely known in the SOI device layer, we assume it does not differ significantly in character from the SIMS profile shown in Figure 6.1, in which we observe a fairly uniform profile for $> 80\%$ of the doped region thickness. Thus, we do not

expect substantial variations due to dopant inhomogeneity, but we must acknowledge that the actual value we report as n is actually a weighted average of the carrier concentration in infinitesimal slabs (weighted by the conductivity of that slab). We proceed with that in mind, but neglect such effects, regarding them as secondary at this point to the larger uncertainties introduced by a potential lack of isolation from the substrate.

Our assumption that the donor state is monovalent is likely suspect, but does not necessarily impact accuracy. The energies required to ionize subsequent levels in a multivalent sulfur impurity typically differ by > 100 meV due to the large Coulomb attraction on the electrons that remain bound to an ionized impurity [129]. Given that ionization of the level we are observing will not be complete until the Fermi level moves several k_bT below it, deeper levels should remain un-ionized until the level we observe is empty. Thus, our approximation of a monovalent impurity likely has negligible impact on the statistics of ionization. However, we have also neglected the excitation spectrum of the impurity we predict; this spectrum contributes to the temperature dependence of the ionization to a small degree. However, incorporating such higher order aspects of the sulfur energetics requires specific knowledge of the sulfur complex we have introduced. We see no evidence in the current data that the excitation spectra of the sulfur state we are measuring significantly impacts the data, at least when considering only in the low-temperature regime in which we have confidence in the layer isolation. Collecting data at lower temperatures would help clarify this large uncertainty, and we do not speculate further on this issue.

6.4.3 High dose samples and impurity band conduction

We also consider behavior of the electrical properties as we increase the sulfur dose. It is at these high doses that we observe the interesting sub-band gap absorption. The highest sulfur dose we study is 10^{16} cm⁻³. At this dose, sulfur concentrations will

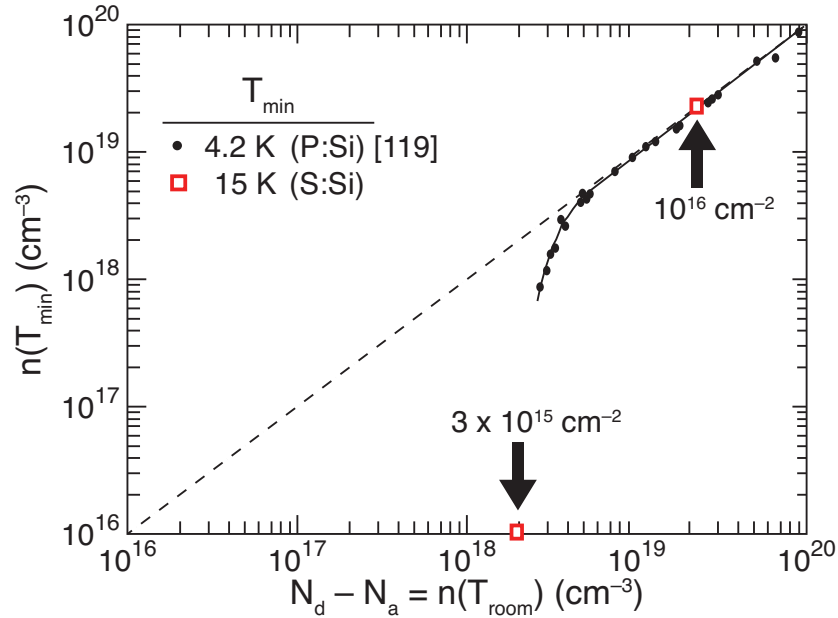


Figure 6.8: A plot of the concentration of ionized impurities at the minimum measurable temperature versus the concentration at room temperature. The black circles represent the data from reference [119], and are the prototypical example of identifying a metal-insulator transition in a doped semiconductor (phosphorus dopants in silicon). We identify the critical concentration as the concentration at which $n(T_{low}) = n(T_{room})$. For P:Si, this concentration is approximately $3.7 \times 10^{18} \text{ cm}^{-3}$. For the sulfur-implanted samples that we measure, we calculate the concentration by dividing the sheet carrier concentration (from Figure 6.2) by $d = 400 \text{ nm}$ (note that the original sulfur dose is labeled on plot). We estimate that the metal-insulator transition occurs at $\text{Log}_{10}(n_{crit} \times \text{cm}^3) = 18.7 \pm 0.5$.

exceed 10^{20} cm^{-3} throughout much of the 400 nm implanted depth. This is well above the concentrations necessary for delocalization of the electrons associated with these deep states [13, 19, 23]. We discussed the semiconductor-to-metal transition in chapter 1, and estimated the critical concentration for common sulfur states in chapter 3. As we mentioned then, at impurity densities near or above 10^{19} cm^{-3} , we predict that the electrons associated with sulfur donors will delocalize and form an impurity metal. As we will see below, our data indicate such a transition to metallic conduction at the highest sulfur doses we measure.

Effect of increasing the dose

The rigorous definition of the transition from impurity states to an impurity band, in the sense of metallic electron transport, is finite conductivity at $T = 0$. In the resistivity data of Figure 6.2, we can immediately observe that at the highest dose of 10^{16} cm^{-2} , the resistivity appears insensitive to temperature as we cool as low as $T = 10 \text{ K}$. Such performance is the hallmark of metallic conduction. A better way to quantify this is to compare the low-temperature carrier concentration to that at room temperature [20, 119]. For metals, a plot of $n(T_{low})$ versus $n(T_{room})$ should form a straight line of $n(T_{low}) = n(T_{room})$; *i.e.*, gold has as many conduction electrons at low temperature as it does at high temperature. In Figure 6.8, we reproduce data from reference [119] for phosphorus dopants in silicon; from this plot, researchers have previously identified the critical concentration of phosphorus for a metal-insulator transition to be $n_{crit} = 3.7 \times 10^{18} \text{ cm}^{-3}$. We plot the data for our sulfur-implanted samples on this same plot by using the sheet carrier concentration of Figure 6.2, and estimating the carrier concentration by dividing by an approximate layer thickness of $d = 400 \text{ nm}$. The only two data points that fall inside our plot correspond to sulfur doses of $3 \times 10^{15} \text{ cm}^{-2}$ and 10^{16} cm^{-2} ; lower doses fall too far below this line to be plotted. We see that the highest sulfur dose sample does indeed fall on the “metal-line”, while the lower dose is substantially below it. Thus, we identify a sulfur-driven metal-insulator transition to occur at $\text{Log}_{10}(n_{crit} \times \text{cm}^3) = 18.7 \pm 0.5$, or approximately $n_{crit} \approx 10^{19} \text{ cm}^{-3}$. Another remarkable observation regards the high dose (10^{16} cm^{-2}) anneal series. Annealing has the effect of increasing the carrier concentration at all temperatures. We will not speculate on the nature of the change in sulfur state that causes this behavior. Rather, we will focus on the result this increase in ionized impurities has on the mobility. At room temperature, an increase in the ionized impurity concentration lowers the mobility. This result is in accord with standard results for semiconductors, which predicts that an increase

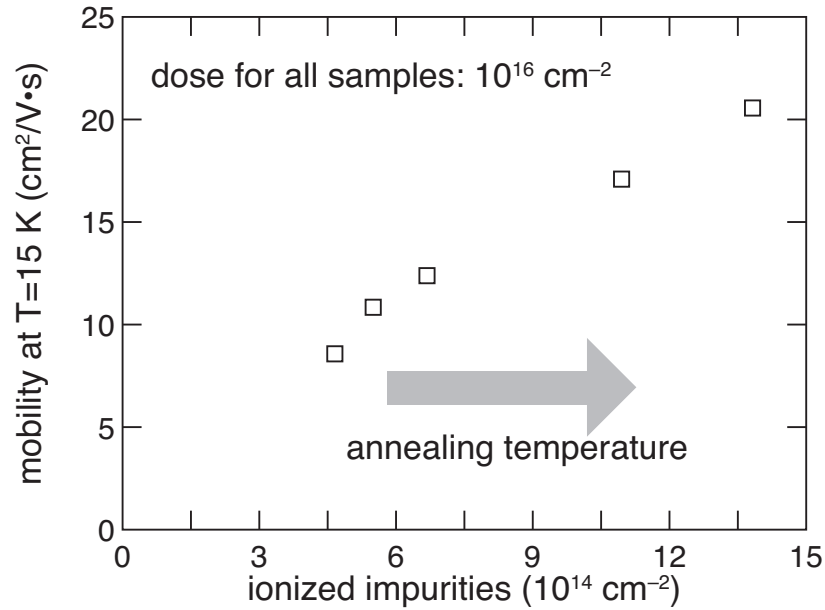


Figure 6.9: The mobility at $T = 15 \text{ K}$ as a function of ionized impurity concentration for the samples implanted with a sulfur dose of 10^{16} cm^{-2} ; moving from left to right the data points represent samples annealed to temperatures of (425, 475, 525, 575, 625) K. General results are shown in Figure 6.3; note that the ionized impurity concentration increases monotonically with annealing temperature. The low temperature mobility increases with the concentration of impurities, which is the signature of impurity-mediated conduction.

in ionized impurities results in an increase in scattering centers and a decrease in mobility at all temperatures [142]. However, in Figure 6.9 we plot the low temperature behavior of the mobility. We observe a significant increase in mobility at $T = 15 \text{ K}$ as ionized impurity concentration increases. Such behavior has been observed before in silicon [20, 143], and is an element of hopping theories of transport [144]. The temperature range we probe does not allow us to distinguish between hopping and true impurity band conduction, but the behavior we observe in the mobility unambiguously supports an impurity-mediated form of transport at low temperature. By “impurity mediated” we mean that conduction occurs among impurities rather than strictly within the conduction band; charge-hopping or conduction within a metallic impurity band are examples of such conduction.

6.5 Conclusion

We have discussed a wide range of data in this chapter, and learned a great deal about the electronic transport properties of silicon implanted with sulfur and processed using pulsed-laser melting. We have seen that transport measurements in the sulfur implanted region cannot be carried out at temperatures much higher than room temperature due to contamination of the signal from the substrate. Because of this possible ambiguity, we considered Hall effect measurements performed on an SOI implanted layer. A fit of the carrier concentration to a monovalent impurity yields an ionization energy of $E_d = 117 \pm 2$ meV of the sulfur donor active in this region; this value corresponds to a well-known sulfur complex in silicon. Our measurements, though, were hindered by poor contacts to samples with low implant density; for some samples the minimum measurable temperature was $T = 100$ K. Additionally, future measurements must include a detailed characterization of the depth-dependence of transport properties, obtained by successive transport measurements interspersed with etching of the active layer to unambiguously determine the true active layer depth.

By considering the low temperature data in samples of increasing dose, we have identified the critical concentration of sulfur dopants for a transition to metallic conductivity to be $\text{Log}_{10}(n_{crit} \times \text{cm}^3) = 18.7 \pm 0.5$, or $n_{crit} \approx 10^{19} \text{ cm}^{-3}$. We wish to emphasize that, to the author's knowledge, this is the first identification of the critical concentration for a metal-insulator transition for such deep states in silicon. This conclusion is supported by high dose samples that have been annealed. In these samples, annealing yields higher free electron concentrations; strikingly, the low temperature mobility *increases* with ionized impurity concentration. This result unambiguously supports the conclusion of impurity dominated conduction.

Additional work must be done at lower temperatures. Such work would confirm the nature of transport (*i.e.* hopping versus free-electron transport), and a wider temperature range would clarify if other sulfur states are present. However, Hall measurements will be of no use in determining impurity energy states at the high concentrations at which we see evidence of impurity based conduction. Thus infrared optical spectroscopy is imperative; such measurements would both confirm the results of the value of E_d that we extracted on low-dose samples, and also yield information on the presence (or lack thereof) of this state in samples of higher dopant densities. Hall measurements, however, still have an important role in telling us about these metallic-like samples, as they can provide crucial insight into the *nature* of transport by revealing the behavior of the electron mobility.

We have yet to address the fascinating issue of the infrared absorption. The measurements presented in this chapter do not directly address optical sensitivity of an impurity band formed by sulfur dopants. Other researchers have reported that high densities of indium dopants (which introduce p-type states state of an ionization energy similar to our findings with sulfur) may improve long-wavelength response of crystalline silicon solar cells [145]. However, we are unable to conclude if the optical absorption does indeed arise from sulfur states centered at these this level, so such speculation is likely premature. A particularly confusing issue – assuming our ignorance of the impact of the sulfur profile on transport data did not lead us significantly astray – is that over 90% of the sulfur impurities appear to reside in a different state than the one we identified in our fit. It remains to be seen if the sulfur state we observe in this work represent clusters, or if a significant fraction of sulfur atoms reside in a much deeper state; alternatively, a fraction of the sulfur atoms in the implanted region could have somehow “deactivated” electronically through a structural rearrangement such as precipitation. Temperature-dependent measurements of electronic transport will surely play a significant role in answering these questions.

Chapter 7

Summary and future directions

We conclude with a brief, critical analysis of the work documented in this thesis, and commentary on the future directions of this field. The sub-band gap optical absorption exhibited by silicon doped with chalcogens beyond the equilibrium solubility limit motivated this thesis. As we discussed in chapter 1, doping semiconductors beyond the critical concentration for the metal-insulator transition is a potential route to realizing improved photovoltaic efficiencies via the impurity band photovoltaic effect. We presented the background of non-equilibrium chalcogen concentrations in silicon in chapter 2: whether via ion implantation or fs-laser implantation, high concentrations of S, Se, or Te in silicon yield significant sub-band gap absorption. We argued then that critical, fundamental information is missing in our understanding of these materials: primarily the energy states introduced into the silicon band structure by the dopants, and the existence or lack thereof of an impurity band.

Although previous researchers have probably made this realization, the author's view is that it is often overlooked that "black silicon" is a result of two unique fs-laser effects. The first is the capability of fs-laser irradiation to implant high concentrations of impurities

into a silicon substrate. The second is that given proper laser exposure and post-exposure annealing parameters, the laser-doped silicon has a physical and electronic structure appropriate for optoelectronic devices (*e.g.* high gain photodiodes). Chapter 4 explored this distinction, proving that irradiation of silicon (while in an SF₆ environment) just above the melting threshold yields a non-equilibrium sulfur concentration. It is the author's view that this is a critical area for continued study: other means are available for regaining crystal structure of a shallow amorphous layer, such as ns-laser melting. However, a more rigorous understanding of the mechanism and limits of laser-implantation may establish it as a method for achieving repeatable, predictable dopant distributions. Critical areas of future study in this area will be the time-resolved melting and resolidification dynamics, with the eventual goal of elucidating the implantation mechanism. Future investigations should also explore the effect of varying laser fluence as a potential means to change the phase of the re-solidified silicon layer, and partial pressure of the sulfur bearing gas as a means to effect the resulting laser-implanted dose.

Our study of electronic transport in silicon doped beyond equilibrium limits with chalcogens had some striking successes. In samples doped via ion implantation, described in chapter 6, we successfully determined one of the sulfur states introduced at low dose, and provided strong evidence of a metal-insulator transition at high doses. Future steps in this area are quite clear: transport information at lower temperatures must be obtained to rigorously show that the samples we study exhibit metallic conduction, as well as determine the nature of electron transport. Both of these will demand measurements at lower temperatures. Additionally, successive transport measurements should be carried out interspersed with shallow etching to determine the depth dependence of these transport properties.

Our study of transport properties in silicon doped with sulfur using many fs-laser pulses above the ablation threshold had successes, but also areas for improvement.

In chapter 5, we presented new evidence for the formation of an impurity band using arguments of Fermi level pinning, lack of temperature sensitivity in the Hall coefficient, and new extended optical absorptance data. However, our efforts were complicated by lack of layer isolation at high temperatures, and an inability to vary the sulfur dose. Future efforts in this area should certainly explore methods to lower the sulfur dose by, for example, lowering the partial pressure of SF_6 during laser exposure. It may be that photoconductivity could better show the existence and characteristics of an impurity band, and this technique should be aggressively pursued in the future. However, the lack of detailed information regarding the depth profile of sulfur dopants will significantly hinder the ability of any future researcher to make rigorous conclusions based on such transport data.

The final issue we address here is that of layer isolation. For all the experiments discussed in this thesis, the issue of layer isolation proved particularly vexing, and — although it may not be apparent in these pages — the author expended substantial time on this issue. For fs-laser doping, one potential route for layer isolation is to perform single-shot studies on SOI wafers with a device-layer thickness tuned to be approximately equal to the laser interaction depth. Chapter 4 provides all the information necessary to move forward in this fashion. The author's efforts in this regard were hindered by a lack of structural knowledge in the resulting doped layer. As we found in Chapter 4, there is an amorphous layer near the surface following irradiation just above the melting threshold. This layer probably contaminated transport measurements, and efforts to thermally anneal the laser-implanted layer were misguided, as the sulfur dopants will simply precipitate out in equilibrium configurations. Thus, the PLM technique must be employed with such samples such that solute trapping can guarantee both high chalcogen concentration as well as crystallinity; alternatively, higher laser fluences during the initial fs-laser process may yield re-solidification in a crystalline phase. For both the fs- and ns-laser doping processes,

transport measurements interspersed with successive shallow etching will clarify the need for further layer isolation.

We wish to close with a few final thoughts regarding the motivation behind this entire thesis: impurity band photovoltaics. Femtosecond laser doping of silicon is but a small piece of this emerging and exciting field. By providing the first evidence of a chalcogen-driven transition to metal-like conduction in silicon, this thesis provides abundant justification for further study of high chalcogen concentrations in silicon. As we have described above, there is substantial work remaining to be done. With specific regard to the fs-laser process: this thesis has tried to address both the fs-laser doping *process*, as well as the resulting *properties* and *structure* as they are potentially relevant to impurity band devices. Because impurity band devices are an emerging field on their own, it is challenging — and perhaps even ill-advised — to attempt addressing both the laser-doping technique and its photovoltaic applications simultaneously. However, fs-laser doped silicon has already demonstrated its capacity for unique technological applications. Thus, even with the risks of addressing a new technology with a new technique in mind, I am hopeful that future researchers continue to study this field and its enormous potential in the field of photovoltaics.

Appendix A

Controlling surface morphology in fs-laser doped silicon

We demonstrate a large area ($> 1 \text{ cm}^2$) of silicon implanted with a sulfur dose of $3 \times 10^{14} \text{ cm}^{-2}$ via femtosecond laser irradiation in a gaseous SF_6 environment. Unlike previous reports of fs-laser doping, the resulting surface is specular. Near the surface, concentrations are as high as 10^{20} cm^{-3} , nearly four orders of magnitude above the solid solubility limit. Scanning and transmission electron microscopy indicate a surface with roughness well below the Rayleigh roughness criterion for specular reflection of visible light. The doped region is amorphized, and demonstrates anomalously high levels of absorption for photons with energy less than the band gap of silicon or optical gap of amorphous silicon.

A.1 Introduction

We have previously demonstrated that fs-laser pulses above the ablation threshold can be used to dope silicon with an ambient gaseous or solid dopant beyond the solid solubility limit [53,68]. When the dopant is chosen from among the heavy chalcogens (S, Se,

Te), the resulting doped silicon exhibits remarkable optical properties, such as absorption of photons with energy less than the band gap of silicon, to energies as low as 0.5 eV [53, 65, 68]. We have also shown that these unique optical properties can be incorporated into novel optoelectronic devices, such as high gain silicon photodetectors that demonstrate responsivity at photon energies as low as 0.8 eV [71].

However, treatment of a silicon surface with fs-laser pulses above the ablation threshold generates significant changes in the surface morphology [51]. Indeed, a variety of surface morphologies can be developed by adjusting the local chemical environment [54, 60, 61, 66, 69], and several have had interesting biological [146] and sensing [62] applications. The surface roughness has been explained as an evolution of laser-induced periodic surface structures [56]. However, for the purposes of material characterization, and potentially some devices, this surface roughness is an obstacle. In this paper, we describe successful efforts to generate fs-laser doped layers that are optically flat.

A.2 Experimental

We begin by outlining the general principal of generating the specular surface, and then proceed to the experimental particulars of this experiment. The goal of this experiment was to melt all points on the surface without reaching the ablation threshold at any point. We begin with a laser pulse traveling in the z direction, with a Gaussian spatial fluence profile in the x-y plane:

$$F(r) = F_0 \exp\left(-\frac{r^2}{2\sigma^2}\right), \quad (\text{A.1})$$

where $r^2 = x^2 + y^2$; fluence is the energy in a pulse divided by its area. Several important thresholds are traditionally defined in terms of their fluence, such as melting (1.5 kJ/m²) [89] and ablation (3.0 kJ/m²) [90] in silicon. Average fluence, defined such that it is equivalent

to peak fluence, is calculated by dividing the energy in the pulse by the area containing points with local fluence great than $1/e$ of the maximum intensity. To generate a uniformly melted laser area, we seek a peak laser fluence F_0 greater than the melting threshold but less than the ablation threshold. For any choice of F_0 , we find the distance r_{melt} defined as the distance away from the peak fluence of an incident pulse that fluence will fall below the melting threshold:

$$F(r_{melt}) = F_{melt} = F_0 \exp\left(-\frac{r_{melt}^2}{2\sigma^2}\right). \quad (\text{A.2})$$

Our experimental goal is to raster the laser beam such that successive pulses strike the surface of our substrate no farther than r_{melt} from the previous pulse. Indeed, in order to obtain a laser-treated surface with the most uniform characteristics possible, we wish to choose a small value for r . However, our experimental efforts are complicated by the fact that nanoscale capillary waves can be excited on the silicon wafer's surface while it is molten due to laser-melting [54]. These waves can focus the laser beam into the valleys formed by these structures. This effectively increases the fluence, potentially above the ablation threshold. This would result in the creation of large amounts of surface roughness as we have observed in much of our previous work. Thus, it is to our advantage to select the largest r that satisfies $r < r_{melt}$. Experimentally, we will find only a narrow window of laser parameters that meet both requirements.

To test this principle, we prepared a (111) Si wafer, doped n-type with phosphorus to a resistivity of $\rho = 800 - 900 \text{ } \Omega\cdot\text{cm}$. We cleaned the surface using ultrasonic cleaning in baths of acetone, methanol, isopropanol, and deionized water. We etched the wafer in dilute (5%) HF to remove the native oxide, and immediately placed the silicon wafer in a vacuum chamber. We evacuated the chamber to $< 1 \text{ Pa}$, and backfilled the chamber with SF_6 at a pressure of $6.7 \times 10^4 \text{ Pa}$.

Our regeneratively amplified laser system has an average pulse energy of $300 \text{ } \mu\text{J}$ and

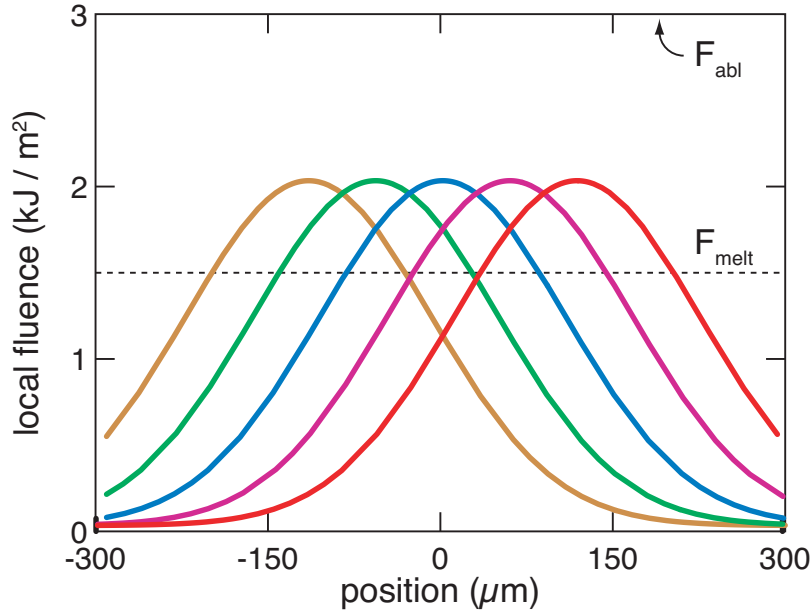


Figure A.1: The calculated fluence exposure on the silicon surface given the laser and rastering parameters we have chosen. We note that all locations are exposed to a laser fluence above the melting threshold.

a repetition rate of 1 kHz. To satisfy the requirements outlined above for silicon ($F_{melt} = 1.5$ kJ/m², $F_{abl} = 3.0$ kJ/m²), we reduce our laser repetition rate to a frequency $f = 11$ Hz using a mechanical shutter, reduce laser pulse energy to 140 μ J, focus the laser beam to a full-width at half-maximum of 250 μ m, and space the laser pulses in the x- and y- directions by 58 μ m. We accomplish this pulse spacing by translating the silicon wafer at a speed $v = 640$ μ m/s in the plane perpendicular to the laser beam using stepper motors. Figure A.1 illustrates the calculated fluence exposure of an arbitrary line on the silicon surface; we see it satisfies the predicted requirements for a flat surface.

After fabrication, we measure the transmittance and reflectance in a UV-VIS-NIR spectrophotometer equipped with an integrating sphere. We imaged the surface in a scanning electron microscope (SEM), and also prepared a cross-sectional sample for transmission electron microscopy (TEM). Secondary ion mass spectroscopy was performed using using

a 7 keV Cs ion beam and an ion current of 200 nA. The SIMS signal was collected from a square region $100 \mu\text{m} \times 200 \mu\text{m}$. Because the most abundant isotopes of oxygen and sulfur have atomic weights of 16 and 32, respectively, there is potential ambiguity over which species we are counting when we monitor the atomic mass 32 signal, assuming singly ionized masses are being measured. To ensure we are measuring sulfur, we monitor the ratio of atomic mass 32 to 34 coming from the sample. By comparing the ratio of these signals to known values for sulfur's isotopic abundance ($^{32}\text{S}:^{34}\text{S} \approx 22$), we ensure that we are measuring sulfur rather than oxygen in the SIMS signal. Count profiles were corrected for a non-linear detector saturation counting error, and calibrated against a known ion implanted sample to generate concentration versus depth.

A.3 Results

After the laser-exposure, the surface appears to remain specular to visible light; we show this in a photograph in Figure A.2 (left, see caption for identification of doped region). Closer inspection under an SEM (Figure A.2, right) also shows no significant surface roughness. A small surface feature, the largest we could find after searching a significant area, is highlighted in the image. No roughness could be observed of significance to visible light ($\lambda > 400 \text{ nm}$).

The bright-field TEM image is shown in Figure A.3. The image confirms that the surface has little or no surface morphology. A selected area diffraction (SAD) pattern is shown inset. The aperture was placed over the surface region; the diffraction pattern indicates amorphous arrangement of the silicon atoms. The amorphous surface layer is $70 \pm 5 \text{ nm}$ thick. A high magnification image is also shown in the figure, in which columns of atoms are evident in the lower layer, but not in the surface region.

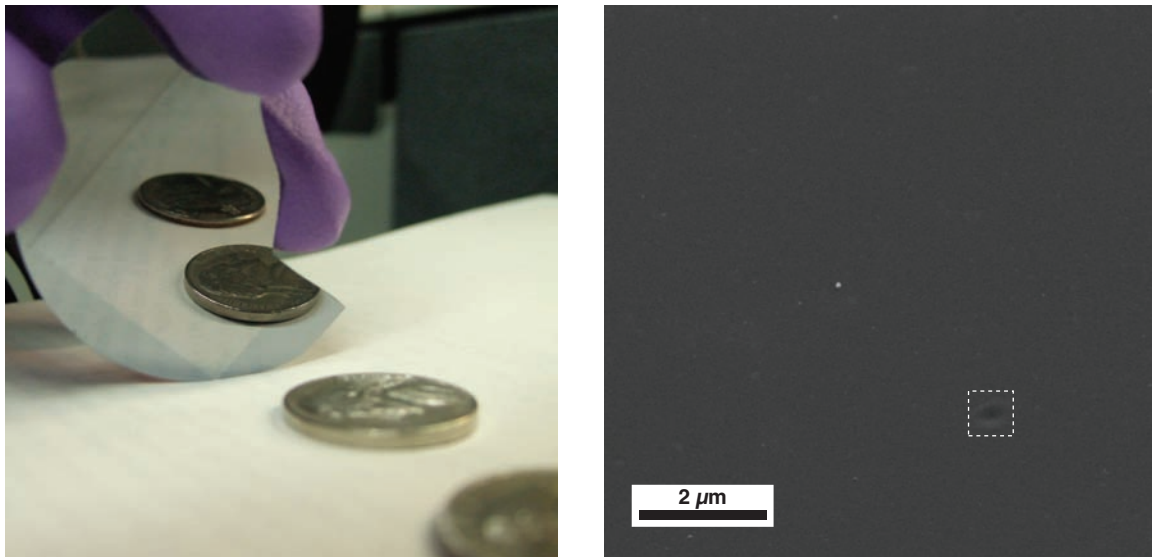


Figure A.2: *Left*: A photograph of the laser-irradiated area, demonstrating specular reflection. *Right*: A high magnification image of the surface; the largest surface feature the author could find is outlined in the white box.

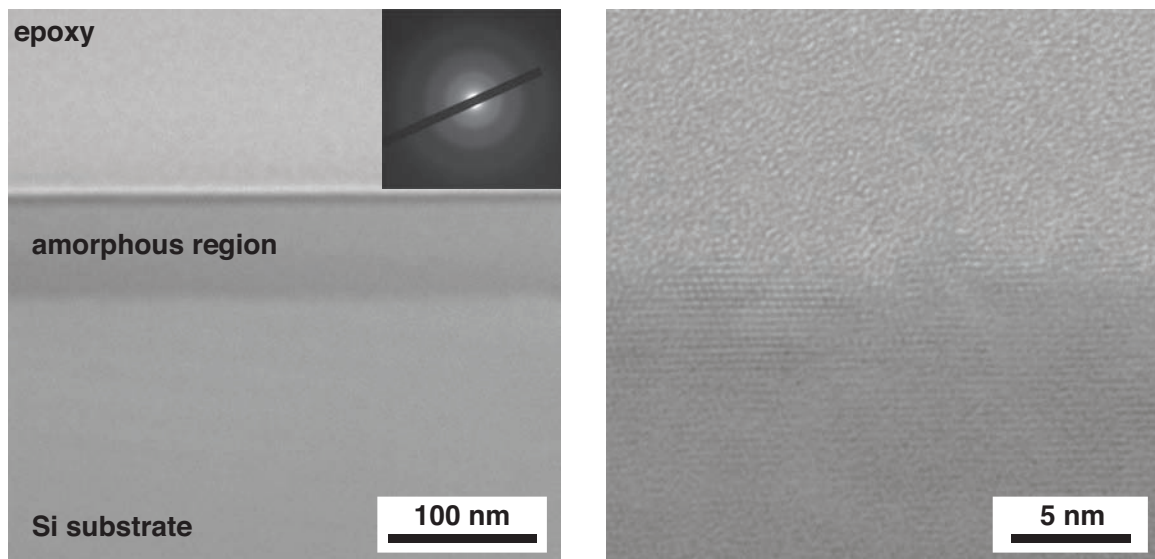


Figure A.3: *Left*: A bright field TEM illustrates two distinct regions with different crystalline structure; the top layer is amorphous (selected area diffraction inset); the layer below is crystalline and of the same orientation as the substrate. *Right*: High magnification view of the interface (note reversed contrast); atomic columns are visible in the crystalline region.

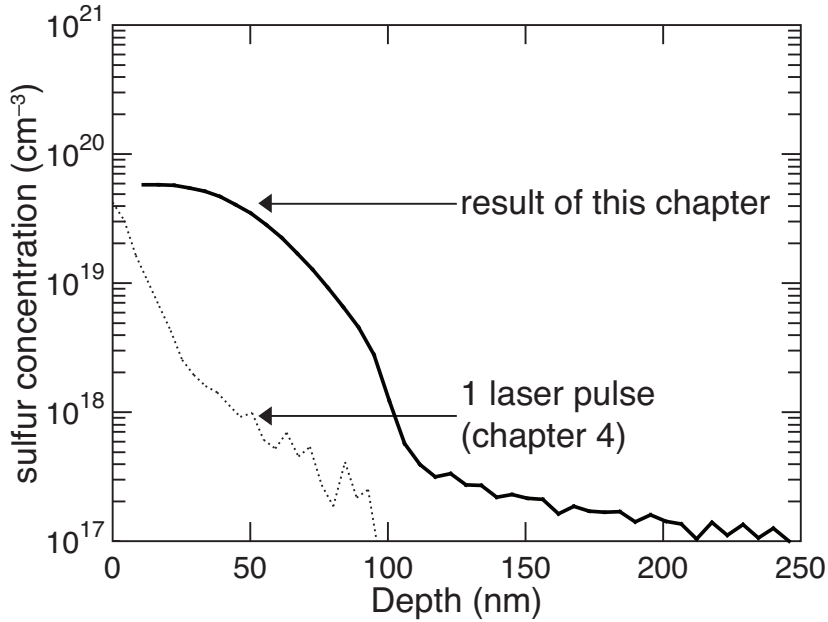


Figure A.4: SIMS reveals a sulfur concentration significantly above the solid solubility limit extends almost 100 nm into the silicon wafer.

The results of SIMS are shown in Figure A.4. The first two data points were contaminated by oxygen from the native oxide and we discard them. The concentration near the surface is at least $6 \times 10^{19} \text{ cm}^{-3}$, and concentrations significantly above the solid solubility limit (10^{16} cm^{-3}) extend at least 100 nm into the material. The detection limit of the measurement, due to oxygen contamination in the chamber is approximately 10^{17} cm^{-3} . The total sulfur dose, obtained by integrating the area under the curve in Figure A.4, is $(2.8 \pm 0.2) \times 10^{14} \text{ cm}^{-2}$.

The normalized absorptance A , calculated from the transmittance T and the reflectance R as $A = (1 - R - T)/(1 - R)$ reflects the fraction of unreflected light that is absorbed in the material. In Figure A.5 we plot this quantity as a function of wavelength.

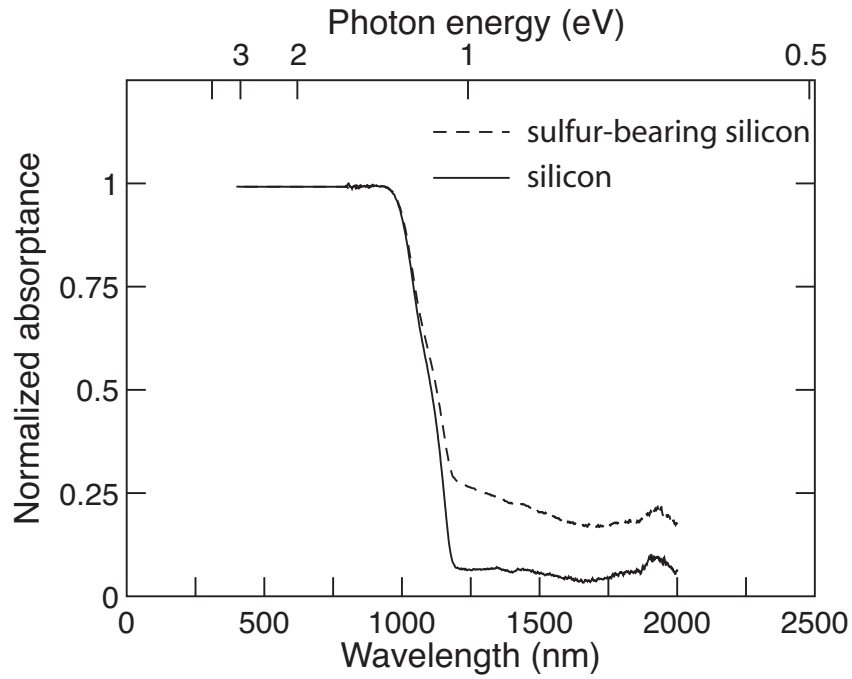


Figure A.5: Sulfur introduced into silicon via femtosecond laser doping yields significant infrared absorption.

A.4 Discussion

As originally pointed out by Lord Rayleigh [147], waves will reflect in a specular fashion when

$$\lambda \ll \sigma_h, \quad (\text{A.3})$$

where λ is the wavelength of a wave incident upon a surface with an average roughness σ_h . By simple inspection of Figure A.2, we can see that we have met this criteria for visible wavelengths. The SEM and TEM both confirm this simple observation. Indeed, the feature highlighted in the box in figure A.2, a feature demonstrating a variation of surface height on order 100 nm, was quite difficult to find, and required searching over a relatively large area.

Consistent with our observations in chapter 4, our TEM image indicates that at least the upper layer of the volume melted by fs-laser irradiation is amorphous. This observation should be contrasted against our previous publications regarding irradiation above the ablation threshold [66, 69], for which we observed significant crystallinity in the laser-doped region. Other authors have previously noted — for both picosecond and femtosecond laser irradiation of silicon — that there is a low fluence regime in which the irradiated silicon resolidifies in an amorphous phase, while at higher fluences there is an “annealed” regime in which crystal order is recovered because the additional energy deposited by the laser pulse leads to a longer cooling period, and sufficient time for crystal regrowth [77]. The threshold for this annealing process has been estimated to be 5.5 kJ/m^2 , significantly above the fluences used in this experiment [91]. It is important to note, however, that the experiments in reference [91] were carried out in air, however, rather than SF_6 .

These published observations regarding the crystal structure of the re-solidified layer are consistent with our observations, as we are operating at a fluence just above the melting threshold ($F = 2 \text{ kJ/m}^2$). It is unknown at the current time if, by increasing fluence into the “annealing” regime, we could fabricate a substrate with both a specular surface, significant doping levels, and crystalline order. However, our experience with this sample suggests it would be difficult, as any increase in fluence above 2 kJ/m^2 generated rough surfaces in our experiments. With this in mind, it is useful to note that the amorphous, sulfur-bearing layer we observe after irradiation is similar to the amorphous layer found after ion-implantation silicon; to regain crystalline order and maintain supersaturated dopant concentrations in those materials, ns-laser melting is used [43]. We anticipate such methods would similarly allow the recovery of crystal order (in samples such as the one we discuss here) while maintaining supersaturated concentration of sulfur. Similar work has already been published for silicon supersaturated with sulfur via ion implantation [49].

The solid-solubility limit of sulfur in crystalline silicon is about 10^{16} cm⁻³ [38–40]. The SIMS data that we report in figure A.4 demonstrates concentrations 3 – 4 orders of magnitude greater than the equilibrium level, extending approximately 100 nm from the surface. As we discussed in chapter 4, the presence of the amorphous layer proves that the velocity of the resolidification front was moving faster than 15 m/s [96]. Such high resolidification front speeds are well in excess of the velocities necessary for solute trapping [45], and we believe this explains the high concentrations of sulfur in our samples. It is interesting, though, to compare the data in this chapter to what we reported in chapter 4 for irradiation with a single shot of the same fluence used here (2 kJ/m²). We immediately observe the following distinctions for the sample on which we report in this chapter:

1. The dose of sulfur is an order of magnitude higher
2. The dose extends almost twice as deep (100 nm *vs* 50 nm)
3. The shape of the sulfur profile is flatter, and a high concentration extends deeper into the sample

We can calculate the number of times an arbitrary area of the sample surface was exposed to laser fluence higher than the melting threshold N_{melt} ; given the exposure parameters described above, we find $N_{melt} \approx 6$. Interestingly, the ratio of the total sulfur dose D implanted into the samples described in this chapter, to those doped using a single laser pulse (chapter 4) is about $D_{N \approx 6} / D_{N=1} \approx 8 \pm 2$. Thus, to first order, the dose of sulfur appears to scale with melt duration. In chapter 4, we speculated that the dose of sulfur was consistent with the kinetic flux of gas particles across the gas-liquid interface over the duration we expect the silicon surface to be molten. The ratio we observe above is consistent with this observation. However, directly comparing the two results is potentially misleading. The result from chapter 4 was obtained using a different laser system and a shorter pulse

duration ($\tau = 75$ fs) than the results reported here. Additionally, the laser exposure is more complicated for the sample on which we currently report: any given location on the surface has an exposure history consisting of several overlapping laser pulses. However, it seems clear that there is a significant range of doping that can be achieved by altering some combination of laser parameters. Future experiments will explore this relationship in more detail.

Finally, from the optical data presented in Figure A.5, we note the presence of a significant increase in absorptance at photon energies below the optical band gap of silicon (crystalline or amorphous). One reason fs-laser doping of silicon with sulfur is interesting is that it demonstrates strong absorption of photons with energy less than the band gap. The absorptance we observe in figure A.5 is significantly lower than what we observe in roughened black silicon [53, 65], but significant nonetheless. Such similar absorption — featureless absorption between 1100 nm and 2500 nm — suggests that similar impurity levels must be available regardless of the lack of longer-range order. The lower value of this absorptance could be due to several reasons, such as the shorter path length through the sulfur rich region due to a lack of surface roughness. Alternatively, the amorphous structure of the doped layer reported here could affect the local coordination and energy states of the implanted sulfur. In silicon ion implanted with sulfur above the solubility limit, other researchers have observed significantly increased sub-band gap absorption when crystal order is restored to an amorphous silicon layer supersaturated with sulfur [49].

A.5 Conclusion

We have demonstrated silicon implanted with sulfur beyond the solid solubility limit using fs-laser irradiation. The resulting surface maintains a highly polished, specular

appearance, an observation maintained under inspection by high magnification electron beam imaging. We have characterized both the sulfur concentration profile, as well as the crystal structure. We find that a sample prepared in this manner also displays currently unexplained absorption photons with energy less than the band gap.

The results described here represent the first successful use of fs-lasers to generate super-saturated concentrations of sulfur in silicon without generating substantial surface roughness. Although ion-implantation techniques are capable of reaching super-saturated concentrations of sulfur in a silicon lattice [49], the use of lasers to these concentrations over a large area is potentially attractive from a manufacturing perspective. Lasers are easily integrated into an in-line process, while ion-implantation is a high-vacuum batch-process. Additionally, the large area of non-equilibrium doped substrate makes available new optical techniques for characterizing this fascinating material.

A.6 Acknowledgements

Several people contributed to this work. The author conceived the experiment, fabricated the samples, analyzed the data, and acquired all the data except the TEM and the SIMS curves, and prepared the manuscript. Haifei Zhang prepared the samples for TEM imaging, and acquired the images. Tom Mates assisted with the SIMS measurements. The authors are indebted to Michael Aziz for helpful discussions.

Appendix B

Femtosecond laser doping of silicon with selenium

In this chapter, we record the current status of investigations currently ongoing regarding femtosecond laser-doping of selenium in silicon. Although we are not ready to draw firm conclusions, we have accumulated significant new results in the last year and it seems appropriate to summarize them here. Recently, collaboration among the Mazur (Harvard), Buonassisi (MIT), and Gradecak (MIT) groups has brought together a new variety of tools, including optical and electronic characterization, x-ray spectroscopy, and high resolution transmission electron microscopy. We choose selenium as a dopant, in part because it provides similar optical properties as fs-laser doping of sulfur, and as such offers a degree of freedom that may shed light on the questions we have posed throughout this thesis regarding the origin of the interesting optical properties in non-equilibrium chalcogen-doped silicon. For more practical reasons, though, selenium is employed in this collaborative effort because it is heavier than sulfur, and offers a larger cross-section for many of the chemically sensitive techniques described in this chapter. As already mentioned, this chapter is not

intended to tell a complete story, but rather place a bookmark in an ongoing and exciting collaborative investigation of non-equilibrium chalcogen-doped silicon.

B.1 Introduction

Although in this thesis we have primarily focused on non-equilibrium concentrations of sulfur in silicon, the Mazur group recognized early on that all of the heavy chalcogens (S, Se, Te), when introduced in comparable concentrations, yield the same sub-band gap optical properties as non-equilibrium concentrations of sulfur [68, 70, 72]. In a sense, this is a powerful observation, as it allows us to explore a family of dopants that introduce similar optical properties, but that differ in important ways. In this way, exploring the effect of changing dopant may allow us to identify common elements or properties that are important to optical or structural properties of fs-laser doped silicon. For example, S, Se, and Te have significantly different diffusivities in a silicon lattice. By exploring the response of infrared absorbance to various thermal treatments, we have previously shown that the de-activation of infrared absorption is fundamentally linked to diffusion of the dopant [70]. We expect similarly powerful insights to result from continued investigation of similarities and differences that result from choosing different chalcogens for the fs-laser doping process.

This chapter mirrors many of the measurements made in Chapter 5. We discuss the optical properties of silicon doped to non-equilibrium concentrations (Se:Si), which primarily confirm previously observed phenomena [68, 70]. We present new data regarding electronic properties of the laser-doped region and the silicon substrate, as well as electronic transport within the laser-doped region. We include key results from our collaborators in the Gradecak and Buonassisi groups. The reader should refer directly to those groups and their publications for detailed exposition regarding these data, and we present them

here simply for completeness. Finally, we also identify some complications that arise when introducing dopants into the laser-silicon interaction via thin-solid films.

B.2 Experimental

The results described in this appendix all regard silicon doped with selenium beyond the solubility limit using femtosecond laser irradiation in the presence of a thin solid film of selenium, which refer to below using the shorthand “Se:Si.” Selenium is introduced via a thin solid film due to the hazards of working with selenium-bearing gases.

For all measurements below, we prepare (100) silicon wafers; for optical, x-ray, and transmission electron microscopy experiments, we study float-zone grown silicon wafers, doped n-type with phosphorus ($\rho = 3000 - 6000 \Omega\cdot\text{cm}$). For temperature dependent electrical measurements we prepare p-type (boron dopant, $1 - 20 \Omega\cdot\text{cm}$) wafers, a choice that we will see later is necessary for diode isolation of the laser-doped region. As in chapter 5, we employ a variety of substrates for room-temperature $I - V$ measurements (see table B.1). For all substrates, we begin by cleaning the wafers using the standard RCA clean [104]. After cleaning, we etch the native oxide in a dilute (5%) HF solution, and immediately transfer the wafer to the vacuum chamber of a thermal evaporator. We deposit $75 \pm 5 \text{ nm}$ of Se at rate of approximately 0.2 nm/s . Following Se deposition, we confirm the thickness using an ellipsometer, and then immediately transfer the wafer to a vacuum chamber in the laser-doping setup. The chamber is evacuated to high vacuum ($p < 10^{-8} \text{ Pa}$), and subsequently backfilled with $6.7 \times 10^4 \text{ Pa}$ N_2 gas. The N_2 gas is used as an inert ambient to keep the hydrodynamics of the melted silicon similar to other experiments; a detailed explanation of this process and the impact of various laser parameters can be found elsewhere [68, 72].

The wafers are placed before the focus of a train of amplified femtosecond laser

Type / Dopant	Resistivity ($\Omega\text{-cm}$)	Carrier concentration (cm^{-3})	$E_c - E_f$ (meV)
p/B	1	$+1.6 \times 10^{16}$	924
p/B	10	$+1.5 \times 10^{15}$	862
p/B	5000	$+2.2 \times 10^{12}$	694
n/P	5000	-1.0×10^{12}	444
n/P	100	-4.9×10^{13}	343
n/P	10	-5.0×10^{14}	283

Table B.1: Selected properties of silicon substrates laser-doped with selenium

pulses, oriented with the wafer surface perpendicular to the laser beam. The laser pulses are produced by a regeneratively amplified Ti:sapphire femtosecond laser system with a center wavelength of 800nm, pulse duration of about 75 fs, and repetition rate f . We measure the spatial profile at the sample surface by deflecting the beam into a CCD camera, and calculate laser pulse fluence by dividing pulse energy by the area of the pulse (defined as the area of the pulse with intensity greater than $1/e$ of the maximum). Using stepper motors, we translate the silicon wafer in raster scan pattern that achieves a uniform distribution of laser pulses across the area to be doped. Translation parameters are chosen such that the distance between any two laser pulses is $\Delta_x = v/f$ in the x-direction, and $\Delta_y = \Delta_x$ in the y-direction. We choose the spatial extent of the laser intensity profile and stepping distances (Δ_y, Δ_x) such that $\pi w^2/\Delta_y \Delta_x = 100$; where w is the full-width at half-maximum of the laser intensity profile, and all other parameters are defined above. Specific parameters are approximately: $f = 25$ Hz, $v = 1500$ $\mu\text{m/s}$, and $w = 875$ μm , and pulse energy 1.7 mJ. The laser fluence is 2 kJ/m^2 , and the attentive reader will note that these parameters correspond to 175 shots per area (see section 2.4).

Following laser-irradiation, we thermally anneal the doped wafer for 30 min in an open tube furnace, while flowing 300 sccm (5×10^{-2} standard l/s) forming gas (95% He, 5% H_2). For all optical, x-ray, and TEM measurements, samples for each measurement are

cleaved from a single doped region to ensure that identical samples are compared between experiments. The set of samples that we studied include a non-annealed sample, as well as wafers annealed at $T = [475, 600, 725, 850, 975, 1100, 1225]$ K. The thermal profile of each anneal was square-wave in shape, with samples placed directly into a preheated oven and quenched in air after 30 minutes of heat treatment.

After irradiation, we prepare samples appropriate for Hall and I-V measurements. We etch the native oxide from the surface using a dilute (5%) solution of hydrofluoric acid, and evaporate aluminum contacts on both sides using an electron beam evaporator. For I-V measurements, we then isolate the edges and define approximately square areas with sides $L \approx 5$ mm by cleaving the wafer. We then measure the current-voltage properties of the junction between the laser-doped region and the substrate by applying a bias between the front and back contact and measuring the resulting current. The voltage is defined positive when the p-type substrate is raised to a higher potential than the laser-doped region. For Hall and resistivity measurements, we take the metallized sample and mask a square array of 1.5 mm diameter circles (array spacing of 1 cm) on the doped surface using positive photoresist. We etch the unmasked Al layer using a commercial Al etch, and cleave the wafer such that we form square van der Pauw samples with dimensions 1 cm x 1 cm and semi-circular contacts that extend 0.75 mm from each corner. We load the Hall samples into a closed-cycle helium cryostat and measure the resistivity and Hall effect using standard techniques [109]. Our setup includes signal multiplexing that allows us to correct for standard errors by collecting redundant measurements of the Hall voltage. We collect resistivity and Hall effect data over a temperature range $20 \text{ K} < T < 800 \text{ K}$. Temperature steps are taken to be either $\Delta T = 10 \text{ K}$ or $\Delta(1000/T) = 2 \text{ K}^{-1}$, whichever corresponds to a smaller temperature change. The samples are immersed in a magnetic field of approximately 0.75 T (data are collected for positive and negative fields), and excited

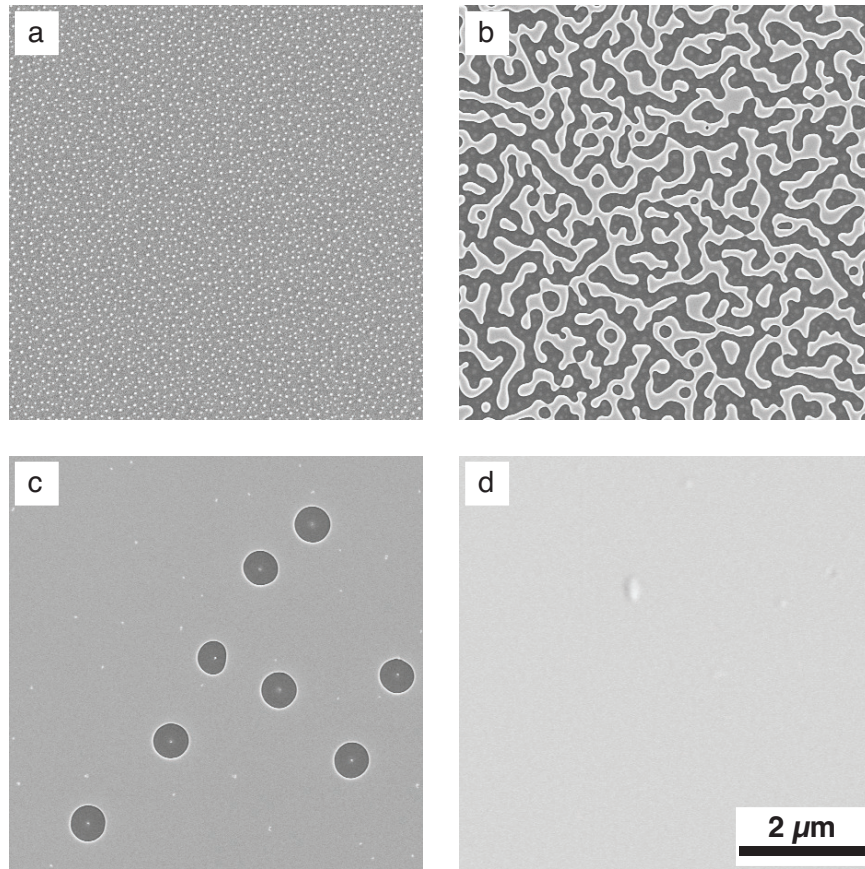


Figure B.1: SEM images of selenium films directly after emerging from a thermal evaporator; films thicknesses shown are *a)* 7.5 nm, *b)* 25 nm, *c)* 38 nm, and *d)* 120 nm.

with the lowest possible current to generate a Hall voltage of approximately $10 \mu\text{V}$. We observe no self-heating effects.

Finally, we measured the optical properties of the samples before and after annealing by measuring the infrared absorptance with a UV-VIS-NIR spectrophotometer equipped with an integrating sphere detector. The diffuse and specular reflectance (R) and transmittance (T) were measured for the wavelength range of $0.4 - 2.5 \mu\text{m}$, in 1 nm increments to determine the absorptance ($A = 1 - R - T$) at each wavelength. One set of samples are delivered to our collaborators are prepared for TEM bright field and dark-field imaging, as well as scanning TEM (STEM) dark-field imaging, which is particularly sensitive to chem-

ical contrast. A second set are prepared for Extended X-ray Absorption Fine Structure (EXAFS) spectroscopy . We will provide an extremely brief overview of this technique later in this appendix.

B.2.1 Special notes regarding selenium doping

We spent considerable time and effort developing techniques for introducing selenium into silicon. We initially observed significant degradation of our selenium films after a few hours: they would transform from sheen, specular, and slightly green in appearance to a distinctly cloudy, smoky appearance. A great deal of time and effort was expended on improving the cleanliness of our sample surface and our thermal evaporator before we noticed that samples kept in a vacuum did not undergo this transformation. Inspection under an SEM (Figure B.1) revealed that the films were degrading over time: collapsing due to what we speculate is a surface tension instability of thin selenium films. We found that films of approximately 75 nm thickness maintain their stability for several hours while also yielding acceptable results for the laser-doping process: high selenium concentrations in the laser-doped region, and no evidence of Se left on the surface after irradiation.

B.3 Results

In Figure B.2, we show an SEM image of the surface morphology that forms as a result of the laser-doping process. Features are larger and blunter than similar structures formed during irradiation in the presence of SF₆ gas; the interested reader should refer to Figure 2.2 and reference [72] for more information and discussion. In Figure B.3, we show the results of the optical absorptance; they are in agreement with previous results [70]. We observe broad, featureless optical absorption from the visible to photon energies as low as 0.5 eV. The average sub-band gap photon absorption decreases with thermal annealing,

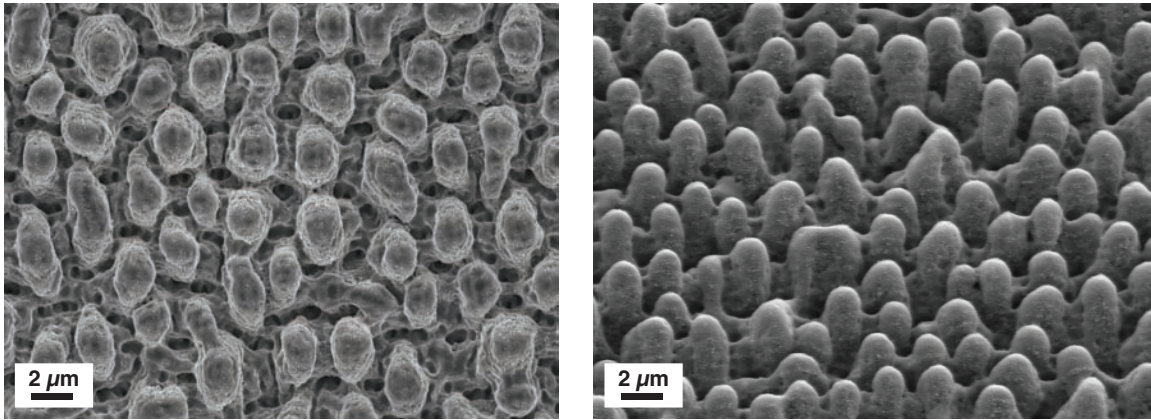


Figure B.2: Scanning electron microscope image of silicon doped with selenium via fs-laser irradiation. *Left*: Top view. *Right*: 45° view.

with higher annealing temperatures yielding lower sub-band gap absorptance.

In Figure B.4, we see the $I - V$ properties of Se:Si for two different experiments. In the top portion of the figure, we see the manner in which $I - V$ properties of the junction between Se:Si and a p-type, $1 - 20 \Omega\text{-cm}$ substrate change with annealing. We observe rectifying behavior for all annealing temperatures except 1100 K. The leakage current is smallest for the highest anneal temperature of 1225 K. In the bottom portion of the figure, we summarize the results of the $I - V$ properties of Se:Si with a variety of silicon substrate doping types and concentrations. This experiment was explained in detail in chapter 5. For all of these experiments the laser-doped wafer was annealed at 975 K for 30 min following laser exposure. In the figure we show the rectification ratio, which expresses the ratio of current through the junction at a forward bias of +1 V to that at a reverse bias of -1 V. This offers us a semi-quantitative picture of the “quality” or existence of rectification at a junction. In the figure, we see that only a narrow range of substrate types yield rectification: p-type substrates with a dopant concentration of less than about 10^{16} cm^{-3} . Dopant concentration is simply found from resistivity using standard tables [133].

Low resolution temperature-dependent $I - V$ measurements were conducted to get

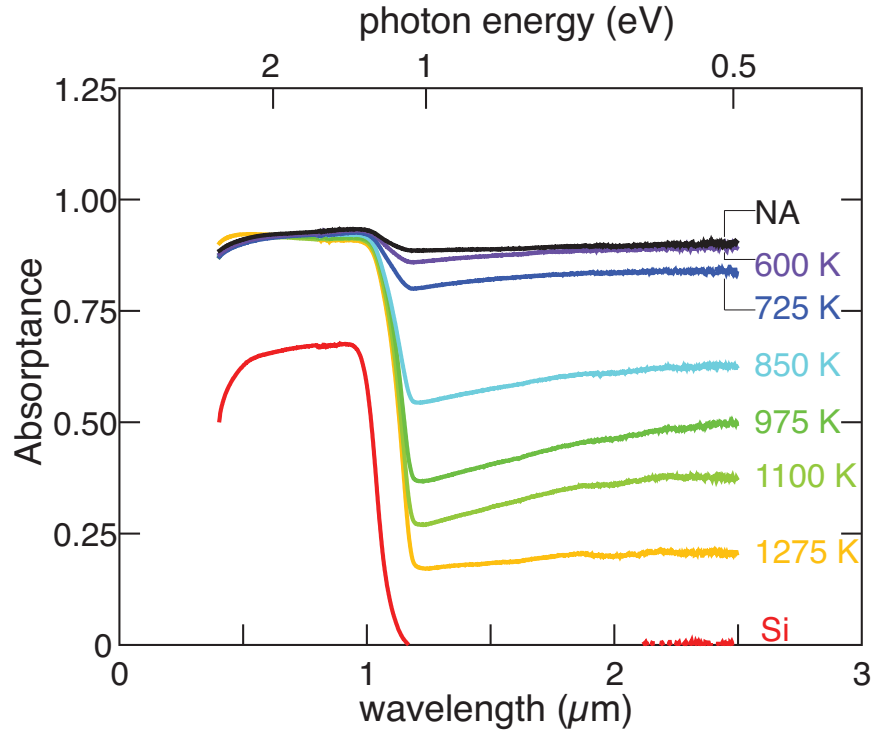


Figure B.3: Optical absorptance ($A = 1 - R - T$) for silicon doped with Se using fs-laser irradiation, subjected to 30 min thermal anneals of various temperatures.

a crude sense of whether we could expect diode-isolation of the laser-doped region. These measurements indicated that rectification at the junction between the laser-doped region and a p-type ($1 - 20 \Omega\cdot\text{cm}$) substrate only occurred below room temperature for samples annealed to 975 K. Keeping this in mind, we plot the results of temperature-dependent transport measurements for the substrate and Se:Si in Figure B.5 (Se:Si formed on a p-type $1 - 20 \Omega\cdot\text{cm}$ substrate, annealing temperature labeled in plot). We plot the magnitude of sheet carrier concentration n_s , sheet resistivity r_s , and calculate the mobility $\mu = (qr_s n_s)^{-1}$.

We calculate n_s as

$$n_s = r_H \frac{I_e B}{q V_{Hall}}, \quad (\text{B.1})$$

where I_e is the excitation current, B is the applied magnetic field, q is the elementary charge,

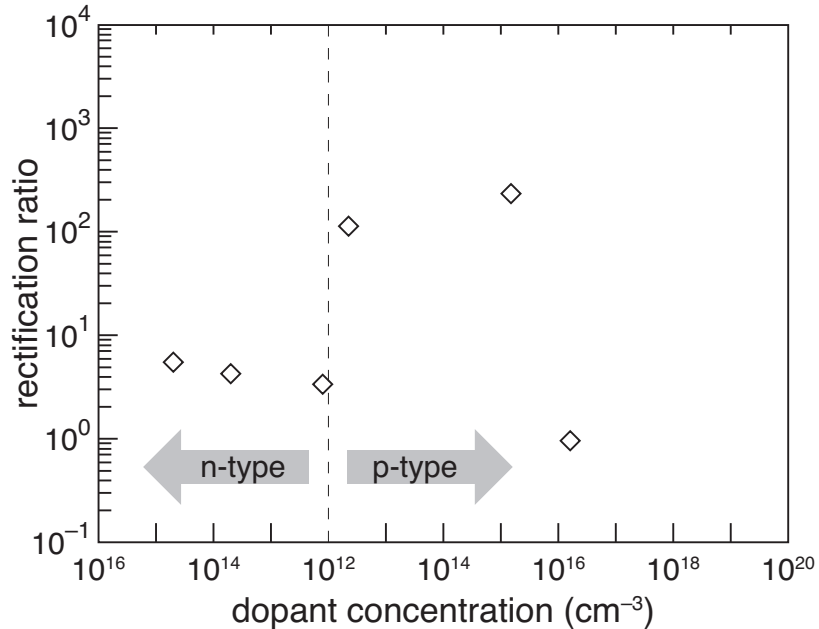
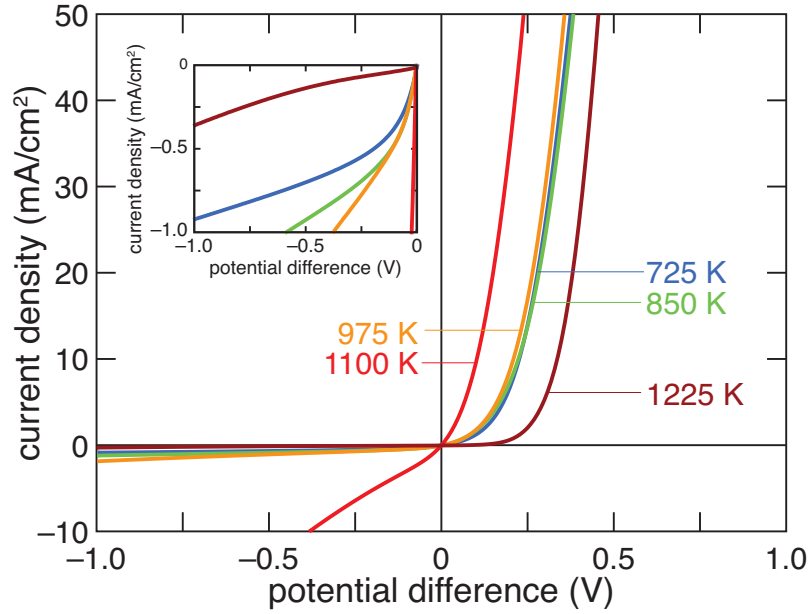


Figure B.4: *Top*: $I - V$ properties of the junction between Se:Si and a p-type $1 - 20 \Omega\text{-cm}$ substrate as a function of annealing. *Bottom*: The rectification ratio (current at forward bias of +1 V divided by current at back bias current at -1 V), calculated from the the room temperature $I - V$ properties of the junction between Se:Si and silicon substrates of various doping concentrations and types. We see behavior similar to that shown in Figure 5.5, for which we performed the same experiment using sulfur-doped silicon.

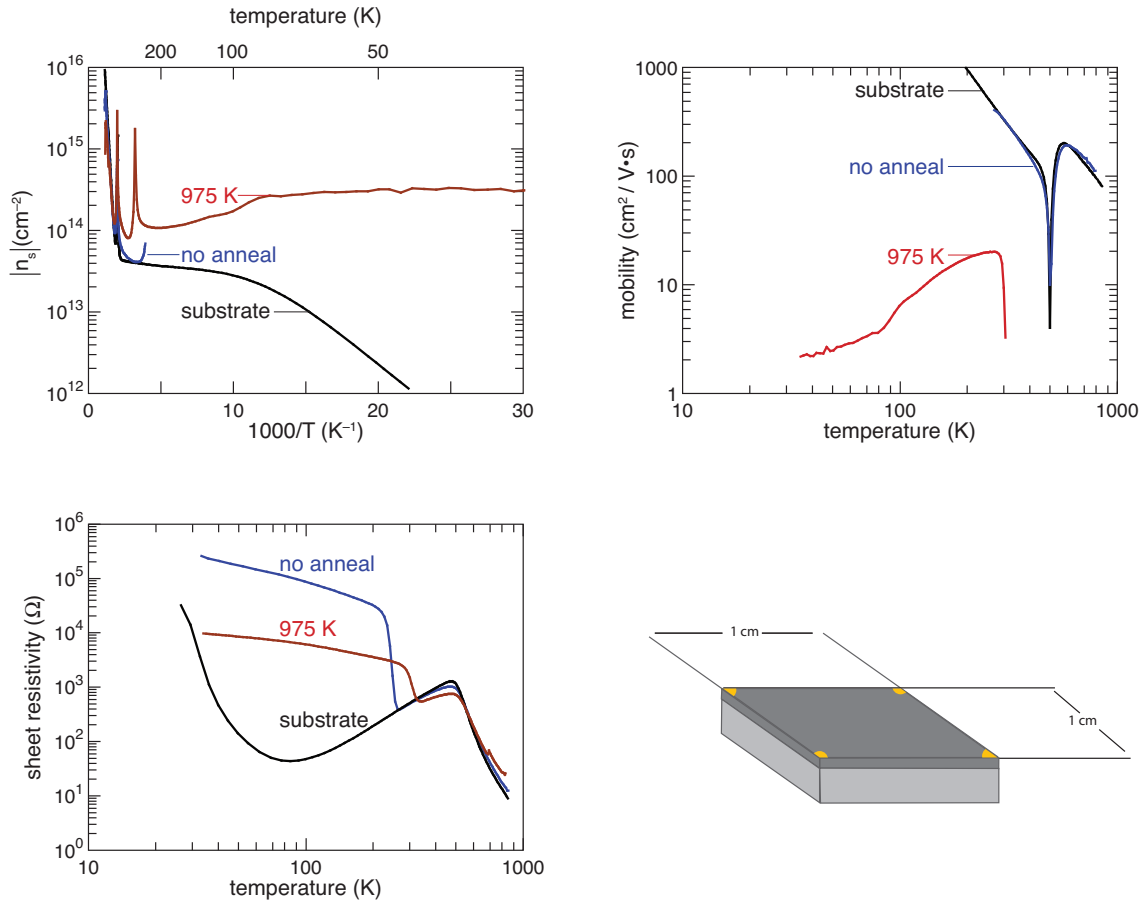


Figure B.5: Temperature-dependent electric transport properties of silicon doped with selenium using fs-laser exposure; here we show (*top left*) sheet carrier concentration versus inverse temperature, the sign of the charge carrier specified in Figure B.6; (*top right*) Hall mobility versus temperature; (*bottom right*) sample geometry (dark grey area represents laser-doped region, light grey represents the substrate); and (*bottom left*) sheet resistivity versus temperature. For these plots, sampling was fine enough that plotted points merge into lines.

V_{Hall} is the measured Hall voltage, and r_H is the Hall scattering factor. We approximate $r_H = 1$, which we expect introduces an error of order unity, but is unimportant to our conclusions here. The sign of the carrier concentration is somewhat complicated to represent. The p-type substrate exhibits the expected behavior, with a positive charge carrier at all temperature below $T \approx 500$ K, above which it transitions to intrinsic conduction and a negative charge carrier. The unannealed Se:Si sample exhibits the same behavior, and

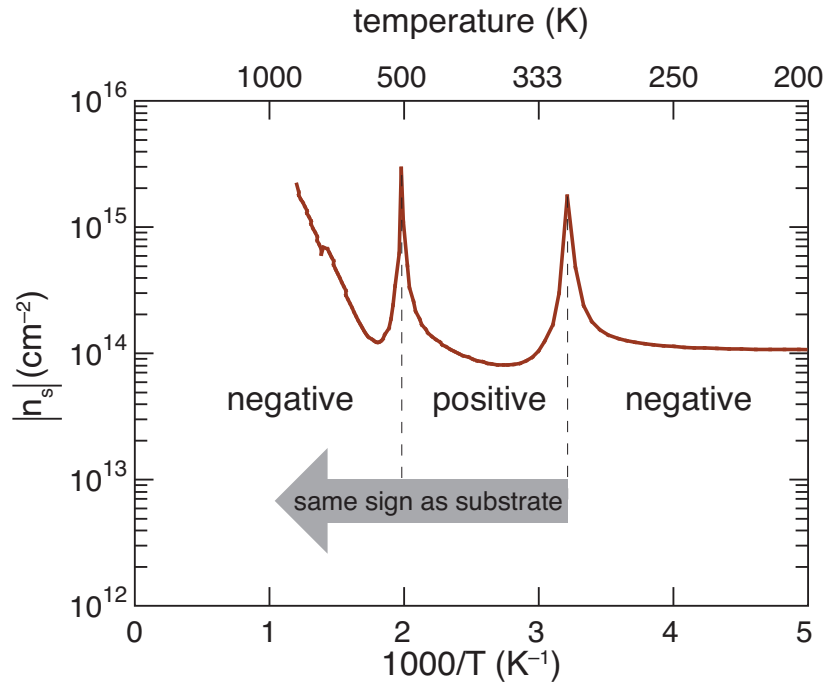


Figure B.6: A detailed view of the high temperature behavior of the sheet carrier concentration for the Se:Si sample annealed to 975 K for 30 min. The spikes in the data represent temperatures at which the Hall voltage changes sign, going through zero and causing large anomalies in n_s .

nearly the same values, as the substrate at all measurable temperatures. The Hall voltage in the unannealed Se:Si sample is only measurable for $T > 250$ K. The sign of the charge carrier in the annealed Se:Si sample is complicated, and we show the behavior of n_s in detail in Figure B.6. For temperatures $T < 300$ K, the sign of the charge carrier is negative. Above 300 K, the Hall voltage goes rapidly through zero as the sign of the charge carrier changes to positive, and n_s appears to have the same or similar values as the substrate for all temperature above this point. This reflects the loss of diode-isolation of the Se:Si region; this loss of isolation is also evident in the sheet resistivity (shown in Figure B.5, where we see that for temperatures above $T = 300$ K, this samples exhibits nearly identical values as the substrate. Thus, we do not consider any data above $T = 300$ K.

B.3.1 Collaborative results

In this section, we briefly highlight some key findings of the Gradecak and Buonassisi groups. In Figure B.7, we show a bright-field TEM image obtained by the Gradecak group of an unannealed Se:Si sample. The image shows a single crystal substrate with a region of differing crystal structure extending throughout the depth of the laser-formed surface features (*i.e.* spikes and ripples). Selected area diffraction reveals that the spike is highly polycrystalline, and chemically sensitive x-ray spectroscopy, conducted during imaging, shows that the entire spike is rich with selenium (the ability to detect it using the EDX tool indicates the selenium is of a concentration on the order of 1%). There are a variety of additional features observable in TEM, such as an oxygen rich surface region approximately 50 nm thick, and as well as a variety of as-yet unidentified structural features within the polycrystalline region.

The Buonassisi group performed Extended X-ray Absorption Fine Structure (EXAFS) spectroscopy on Se:Si on series of samples annealed to different temperatures (the same group of samples represented in Figure B.3). EXAFS is an x-ray technique that carefully examines oscillations in the x-ray fluorescence just above resonance for a particular element; in this case, the spectral region in the vicinity of the selenium absorption edge (12.6 keV) line was examined. The average local environment (structural and chemical) of the selenium impurities imparts small features (or fine structure) to the behavior of this fluorescence signal. When examining a series of samples in which the state of the impurity is expected to change — as we expect selenium changes from an absorbing to non-absorbing state with annealing — principal component analysis can be used to estimate the fraction and spectrum of individual states that add together to create the overall result. The Buonassisi group has published their findings in this area [148], but we summarize one of the most interesting findings in Figure B.8. In this figure, we show the combined results of principal component

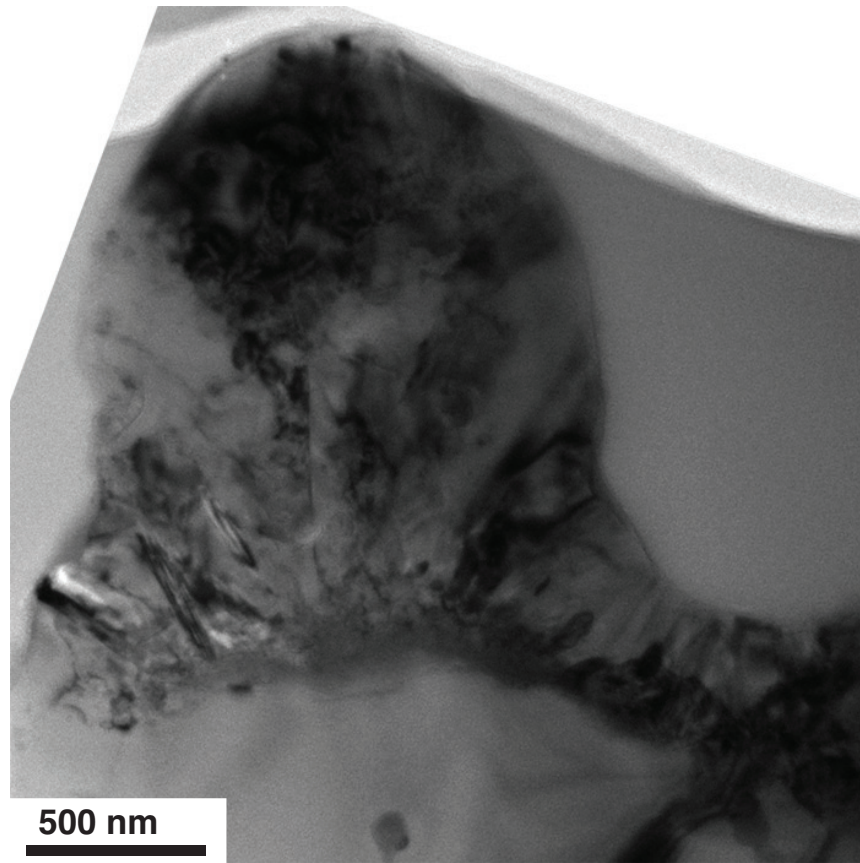


Figure B.7: Bright-field TEM image of silicon doped with selenium via fs-laser exposure. The TEM image reveals a polycrystalline region extending throughout the entire depth ($\approx 1 \mu\text{m}$) of the laser-formed surface morphology, while x-ray spectroscopy reveals about 1% Se throughout the polycrystalline region. Results should be compared to Figure 2.4. TEM imaging performed by Matt Smith of the Gradecak group at MIT.

analysis (PCA) of the x-ray fluorescence spectra, and the infrared optical absorption data of Figure B.3. We see that the average sub-band gap absorptance scales almost monotonically with the fractional presence of a unique chemical state identified in the EXAFS spectra.

B.4 Discussion

The purpose of this appendix is *not* to offer a full interpretation of these results; we cannot resist the opportunity to comment briefly, though. We begin by noting that

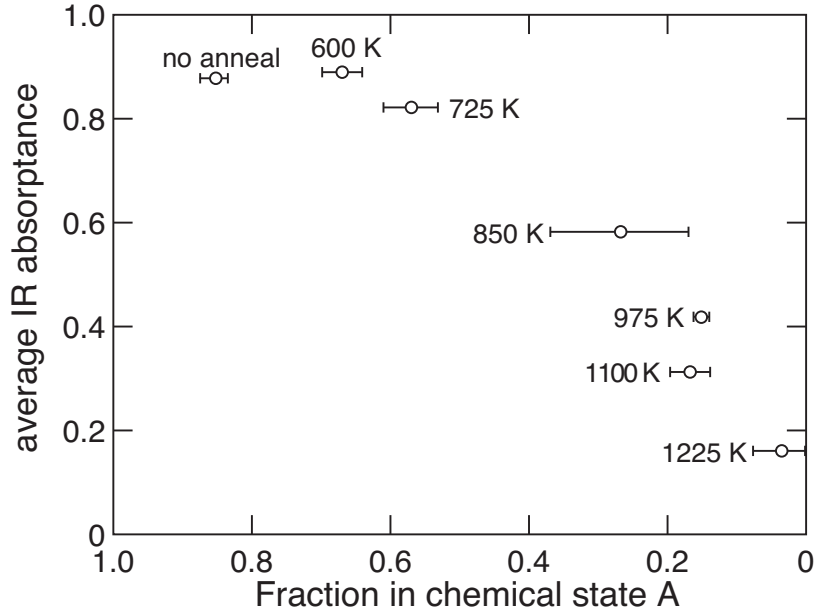


Figure B.8: EXAFS performed by Bonna Newman and Joe Sullivan of the Buonassisi group at MIT; figure adapted from reference [148]

the optical data of Figure B.3 are consistent with previous experiments, in which we have shown that the deactivation of optical is strongly linked with diffusion of the dopant on a length scale of 20 – 40 nm [70]. We will not address this data further.

Next, we consider the data $I - V$ data of Figure B.4. This figure represents, in a semi-quantitative fashion, the nature of the junction between the selenium-doped region and silicon substrate of varying doping type and concentration. As we discussed in detail in section 5.5.2, this experiment represents a type of spectroscopy that yields information regarding the location of the Fermi level. In comparison to Figure 5.5, in which we plot the same data for a fs-laser doping with sulfur, we can make several immediate observations.

1. The sulfur doped substrates provide a higher quality rectifying junction, with larger rectification ratios *in the case* of a rectifying junction. Rectification ratios approached 10^4 for sulfur doped layers, whereas they hardly exceed 10^2 with selenium.

2. The selenium doped layers do not form rectifying junctions with *any* n-type substrate, whereas sulfur-doped layers would form rectifying junctions with lightly-doped n-type substrates.

We can draw two conclusions from these observations. First, the lower value of the rectification ratio for selenium-doped layers indicates a lower quality junction between Se:Si and the substrates relative to the same junctions formed with S:Si. This leakier junction is somewhat surprising given the apparently thicker, and more highly crystalline selenium doped regions apparent in Figure B.7. From the TEM images, we initially supposed that higher crystallinity in the laser-doped region would lead to lower leakage through the junction and a higher “quality” of rectification. The fact that rectification is of lower quality could stem from a more conductive (and thus leaky) inter-grain region. Currently, TEM imaging has not identified specific differences in the inter-grain region, so at this point we cannot draw firm conclusions regarding potential differences between sulfur- and selenium-doped inter-grain regions. The laser-exposure process is dramatically different: selenium doping occurs in an ambient environment of N_2 with an optically thick (75 nm) film of Se atop the silicon, whereas sulfur doping occurs in an ambient environment of SF_6 in which the laser interacts directly with the silicon surface. Thus, it would be unsurprising if the differing laser-exposure yields a different net energy deposition and cooling rate — and thus resulting crystal structure — in the laser-doped region. Second, comparison of Figures B.4 and 5.5 indicates that the Fermi level in Se:Si is pinned slightly lower than in S:Si, given the lack of rectification for junctions formed with *any* n-type substrates. However, as we described in detail in section 5.5.2, the resolution of this type of spectroscopy is limited to a few multiples of k_bT , so it may be misleading to read much into this difference. We do note, however, that many of the Se dimer and complex states introduce energy levels 10 – 30 meV below the comparable centers introduced by sulfur in silicon [129].

The temperature-dependence of important charge transport parameters, such as sheet carrier concentration, mobility, and sheet resistivity, are difficult to interpret. Layer isolation is more difficult to achieve in the selenium doped samples, relative to the sulfur-doped samples that we discussed in chapter 5. As we can see by comparing Figures B.4 and 5.5, this difference clearly stems from the lower quality of the rectifying junction between Se:Si compared to S:Si. Besides the difference in the ability to isolate the doped region, the behavior of selenium- and sulfur-doped samples — both their sheet carrier concentration and sheet resistivity — is quite similar. The lack of temperature sensitivity in the Hall voltage (and thus carrier concentration) is consistent with a transition to metallic-like conduction [119], but without measuring the resistivity at temperature closer to absolute zero, this distinction remains ambiguous.

Finally, we comment briefly on the data obtained by our collaborators, and how they are relevant to previous and current findings regarding Se:Si. As we have already mentioned, the TEM images of Figure B.7 may represent the most puzzling piece of data currently. A polycrystalline region extends as deep as 1 μm , all of which is rich ($\approx 1\%$ atomic) in selenium. We remind the reader that when doping with sulfur from an atmosphere of SF_6 , sulfur is distributed in the region melted by the femtosecond laser pulse; this depth, regardless of laser fluence, is always in the range 50 – 150 nm. We discussed these observations at length in chapter 4 for doping below the ablation threshold, but this behavior is the same for laser-doping with sulfur above the ablation threshold (see Figure 2.4). Thus, this substantially deeper distribution of selenium is quite puzzling. Because the ability to engineer the depth of the dopant implant would be a powerful technological tool, this difference merits significant attention.

At a fundamental level, the EXAFS data is a significant addition to our knowledge regarding the origin of sub-band gap infrared absorption. The PCA analysis indicates that

annealing causes a transition from predominantly one chemical state (which we call “A”) to a second chemical state (which we call “B”). We emphasize to the reader that the PCA analysis *does not assume* this type of behavior (transition from one state to another), nor this number of states. The PCA analysis simply attempts to take the EXAFS fluorescence signal, which for a given state of selenium is akin to fingerprint but changes over the course of annealing, and find the statistically most probable superposition of spectra that will result in the observed behavior. We find it unlikely that the correlation between optical absorption and the chemical states is coincidental. Indeed, it is possible that state A represents the fluorescence signal from the non-equilibrium selenium state that introduces sub-band gap absorption, and which transitions to the equilibrium state B (which is not sensitive to sub-band gap photons) following thermal annealing. Such a relaxation could take the form of dopant precipitation, or something more exotic. Additional analysis of the EXAFS data, in principle, could allow for identification of the atomic arrangements of state A and B. Identification of the chemical and physical structure responsible for sub-band gap absorption is currently the most pressing question regarding non-equilibrium chalcogen doping of silicon. We note in closing, however, that the EXAFS signal is weighted by a chemical state’s concentration. Thus, it is possible that one or both states that the PCA analysis identifies are not responsible for the sub-band gap optical properties but are simply more numerous and react in a similar fashion to annealing. Although we consider this coincidence unlikely — especially given that this would imply that a very small concentration ($\ll 10^{20} \text{ cm}^{-3}$) of dopants are responsible for near-unity sub-band gap absorption in a layer that is less than $1 \mu\text{m}$ thick — we cannot currently rule it out. Addressing this ambiguity must be a priority for future work.

B.5 Conclusion

Our investigation into silicon doped with selenium beyond equilibrium solubility limits via fs-laser irradiation is on-going. The optical and electronic results presented in this chapter paint very similar picture to that which we discussed in chapter 5 for sulfur in silicon. The high selenium concentration yields donor activity and a temperature-insensitive sheet carrier concentration. Although this is suggestive of a metal-insulator transition, the resistivity remains relatively high and we cannot comment rigorously on this topic until data at lower temperatures are available. Fermi level spectroscopy via $I - V$ measurements on a variety of substrates suggest Fermi level pinning at a lower level than in sulfur-doped silicon. Junctions formed between Se:Si and silicon substrates exhibit poorer rectification than S:Si, and they are less stable to temperature increases. This observation is especially puzzling given the higher quality crystal structure resulting from this doping process evidenced in TEM imaging. We are unsure at the present time if the poor rectification is an artifact of laser exposure parameters, or is more intrinsically linked to differences between the selenium and sulfur laser-doping processes.

The preliminary results of a collaborative look into this material are particularly promising. Chemically sensitive TEM has yielded information regarding the distribution of selenium that has been impossible to obtain thus far due to problems introduced by the roughened surface morphology. One particularly poignant question raised by TEM imaging regards the depth of the apparent laser affected region — if the laser-melt depth is on the order of 100 nm, how does doping and poly-crystallinity extend almost 1 μm from the surface? EXAFS measurements have confirmed that the drop in sub-band gap absorptance is inherently linked to a change in chemical state of the selenium dopants. With further (and currently on-going) analysis of the EXAFS spectra, it may be possible to determine the

local chemical coordination of the Se. This is a particularly promising area of research; one which may finally unlock the chemical structure responsible for the fascinating sub-band gap optical properties. Such findings would play a large role in determining the suitability of fs-laser doped silicon for applications such as photovoltaics.

B.6 Acknowledgements

The work in this chapter was highly collaborative. The author, along with Meng-Ju Sher and Eric Mazur, conceived of this experiment together with the entire team of collaborators: Tonio Buonassisi, Silviya Gradecak, Bonna Newman, Joe Sullivan, and Matthew Smith. The author, with abundant assistance from M. Sher, prepared the samples, and performed optical and electronic characterization. B. Newman, J. Sullivan, and T. Buonassisi performed analyzed the EXAFS measurements and prepared the PCA presented in this chapter. M. Smith and S. Gradecak performed and analyzed the microscopy.

References

- [1] S. Carnot, *Reflexions sur la puissance motrice du feu et sur les machines propres a developper cette puissance*. Paris: Bachelier, 1824.
- [2] R. Clausius, “On a modified form of the second fundamental theorem in the mechanical theory of heat,” *Philosophical Magazine and Journals of Science*, vol. 12, no. 77, 1856.
- [3] P. Würfel, *Physics of Solar Cells: From Principles to New Concepts*. Weinheim: Wiley, 2005.
- [4] P. T. Landsberg and G. Tonge, “Thermodynamics of the conversion of diluted radiation,” *Journal of Physics A – Mathematical and General*, vol. 12, no. 4, pp. 551–562, 1979.
- [5] W. Shockley and H. J. Queisser, “Detailed balance limit of efficiency of p-n junction solar cells,” *Journal of Applied Physics*, vol. 32, no. 3, pp. 510–519, 1961.
- [6] C. H. Henry, “Limiting efficiencies of ideal single and multiple energy-gap terrestrial solar-cells,” *Journal of Applied Physics*, vol. 51, no. 8, pp. 4494–4500, 1980.
- [7] M. A. Green, K. Emery, Y. Hishikawa, and W. Warta, “Solar cell efficiency tables (version 34),” *Progress in Photovoltaics*, vol. 17, no. 5, pp. 320–326, 2009.
- [8] A. Feltrin and A. Freundlich, “Material considerations for terawatt level deployment of photovoltaics,” *Renewable Energy*, vol. 33, no. 2, pp. 180–185, 2008.
- [9] M. Wolf, “Limitations and possibilities for improvement of photovoltaic solar energy converters: Considerations for earths surface operation,” *Proceedings of the Institute of Radio Engineers*, vol. 48, no. 7, pp. 1246–1263, 1960.

-
- [10] F. Seitz, "An interpretation of crystal luminescence," *Transactions of the Faraday Society*, vol. 35, no. 1, pp. 74–84, 1939.
- [11] W. Shockley and W. T. Read, "Statistics of the recombinations of holes and electrons," *Physical Review*, vol. 87, no. 5, pp. 835–842, 1952.
- [12] A. Luque and A. Marti, "Increasing the efficiency of ideal solar cells by photon induced transitions at intermediate levels," *Physical Review Letters*, vol. 78, no. 26, pp. 5014–5017, 1997.
- [13] A. Luque, A. Marti, E. Antolin, and C. Tablero, "Intermediate bands versus levels in non-radiative recombination," *Physica B – Condensed Matter*, vol. 382, no. 1-2, pp. 320–327, 2006.
- [14] E. Antolin, A. Marti, J. Olea, D. Pastor, G. Gonzalez-Diaz, I. Martil, and A. Luque, "Lifetime recovery in ultrahighly titanium-doped silicon for the implementation of an intermediate band material," *Applied Physics Letters*, vol. 94, no. 4, p. 3, 2009.
- [15] A. Marti, E. Antolin, C. Stanley, C. Farmer, N. Lopez, P. Diaz, E. Canovas, P. Linares, and A. Luque, "Production of photocurrent due to intermediate-to-conduction-band transitions: A demonstration of a key operating principle of the intermediate-band solar cell," *Physical Review Letters*, vol. 97, p. 247701, 2006.
- [16] K. Yu, W. Walukiewicz, J. Wu, W. Shan, M. Scarpulla, O. Dubon, J. Beeman, and P. Becla, "Diluted ZnMnTe oxide: A multi-band semiconductor for high efficiency solar cells," *Physica Status Solidi B*, vol. 241, p. 660, 2004.
- [17] N. F. Mott, "On the transition to metallic conduction in semiconductors," *Canadian Journal of Physics*, vol. 34, no. 12, pp. 1356–1368, 1956.
- [18] N. F. Mott and W. D. Twose, "The theory of impurity conduction," *Advances in Physics*, vol. 10, no. 38, pp. 107–163, 1961.
- [19] N. F. Mott, "Metal-insulator transition," *Reviews of Modern Physics*, vol. 40, no. 4, p. 677, 1968.
- [20] M. Alexander and D. F. Holcomb, "Semiconductor-to-metal transition in n-type group 4 semiconductors," *Reviews of Modern Physics*, vol. 40, no. 4, p. 815, 1968.
- [21] T. G. Castner, N. K. Lee, G. S. Cieloszyk, and G. L. Salinger, "Dielectric anomaly and metal-insulator transition in n-type silicon," *Physical Review*

- Letters*, vol. 34, no. 26, pp. 1627–1630, 1975.
- [22] P. P. Edwards and M. J. Sienko, “On the occurrence of metallic character in the periodic table of the elements,” *Journal of Chemical Education*, vol. 60, no. 9, pp. 691–696, 1983.
- [23] P. P. Edwards and C. Rao, eds., *Metal-Insulator Transitions Revisited*. Bristol: Taylor Francis, 1995.
- [24] O. Emel’yanenko, T. S. Lagunova, D. N. Nasledov, and Talalaki.Gn, “Formation and properties of an impurity band in n-type GaAs,” *Soviet Physics Solid State, Ussr*, vol. 7, no. 5, p. 1063, 1965.
- [25] H. Neumann, “Influence of impurity band conduction on the electrical characteristics of p-type GaAs,” *Crystal Research and Technology*, vol. 23, no. 10-11, pp. 1377–1383, 1988.
- [26] J. Basinski and R. Olivier, “Ionization energy and impurity band conduction of shallow donors in n-gallium arsenide,” *Canadian Journal of Physics*, vol. 45, no. 1, p. 119, 1967.
- [27] L. Essaleh, S. M. Wasim, and J. Galibert, “Effect of impurity band conduction on the electrical characteristics of n-type CuInSe₂,” *Journal of Applied Physics*, vol. 90, no. 8, pp. 3993–3997, 2001.
- [28] T. F. Rosenbaum, R. F. Milligan, M. A. Paalanen, G. A. Thomas, R. N. Bhatt, and W. Lin, “Metal-insulator-transition in a doped semiconductor,” *Physical Review B*, vol. 27, no. 12, pp. 7509–7523, 1983.
- [29] H. R. Vydyanath, W. J. Helm, J. S. Lorenzo, and S. T. Hoelke, “Development of selenium-doped silicon for 3–5 μm applications,” *Infrared Physics*, vol. 19, no. 1, pp. 93–102, 1979.
- [30] J. Wagner and J. A. Delalano, “Band-gap narrowing in heavily doped silicon - a comparison of optical and electrical data,” *Journal of Applied Physics*, vol. 63, no. 2, pp. 425–429, 1988.
- [31] A. H. Wilson, “The theory of electronic semi-conductors,” *Proceedings of the Royal Society of London Series a-Containing Papers of a Mathematical and Physical Character*, vol. 133, no. 822, pp. 458–491, 1931.
- [32] F. J. Morin and J. P. Maita, “Electrical properties of silicon containing arsenic and boron,” *Physical Review*, vol. 96, no. 1, pp. 28–35, 1954.

- [33] G. L. Pearson and J. Bardeen, "Electrical properties of pure silicon and silicon alloys containing boron and phosphorus," *Physical Review*, vol. 75, no. 5, pp. 865–883, 1949.
- [34] R. Behrensmeier, M. Brede, and P. Haasen, "The influence of precipitated oxygen on the brittle-ductile transition of silicon," *Scripta Metallurgica*, vol. 21, no. 11, pp. 1581–1585, 1987.
- [35] P. M. Fahey, P. B. Griffin, and J. D. Plummer, "Point-defects and dopant diffusion in silicon," *Reviews of Modern Physics*, vol. 61, no. 2, pp. 289–384, 1989.
- [36] P. Pichler, *Intrinsic Point Defects, Impurities, and Their Diffusion in Silicon*. New York: Springer-Verlag Wien, 2004.
- [37] H. Okamoto, *Phase Diagrams for Binary Alloys*. Materials Park: ASM International, 2000.
- [38] R. O. Carlson, R. N. Hall, and E. M. Pell, "Sulfur in silicon," *Journal of Physics and Chemistry of Solids*, vol. 8, pp. 81–83, 1959.
- [39] H. R. Vydyanath, J. S. Lorenzo, and F. A. Kroger, "Defect pairing diffusion, and solubility studies in selenium-doped silicon," *Journal of Applied Physics*, vol. 49, no. 12, pp. 5928–5937, 1978.
- [40] F. Rollert, N. A. Stolwijk, and H. Mehrer, "Diffusion of s-35 into silicon using an elemental vapor source," *Applied Physics Letters*, vol. 63, no. 4, pp. 506–508, 1993.
- [41] J. W. Mayer, L. Eriksson, and J. Davies, *Ion Implantation in Semiconductors*. Academic Press, 1970.
- [42] S. Ferris, H. Leamy, and J. Poate, eds., *Laser-Solid Interactions and Laser Processing - 1978*. New York: American Institute of Physics, 1978.
- [43] C. W. White, S. R. Wilson, B. R. Appleton, and F. W. Young, "Supersaturated substitutional alloys formed by ion-implantation and pulsed laser annealing of group-iii and group-v dopants in silicon," *Journal Of Applied Physics*, vol. 51, no. 1, pp. 738–749, 1980.
- [44] F. Spaepen and D. Turnbull, "Kinetics of motion of crystal-melt interfaces," in *Laser-Solid Interactions and Laser Processing* (S. Ferris, ed.), (Boston), pp. 73–83, American Institute of Physics, 1978.

- [45] M. J. Aziz, "Modeling and measurement of solute trapping," in *Laser Surface Treatment of Metals* (D. C.W. and P. Mazzoldi, eds.), pp. 649–661, Marinus Nijhoff Publishers, 1986.
- [46] R. Reitano, P. M. Smith, and M. J. Aziz, "Solute trapping of group III, IV, and V elements in silicon by an aperiodic stepwise growth-mechanism," *Journal of Applied Physics*, vol. 76, no. 3, pp. 1518–1529, 1994.
- [47] J. A. Kittl, P. G. Sanders, M. J. Aziz, D. P. Brunco, and M. O. Thompson, "Complete experimental test of kinetic models for rapid alloy solidification," *Acta Materialia*, vol. 48, no. 20, pp. 4797–4811, 2000.
- [48] S. Fischler, "Correlation between maximum solid solubility and distribution coefficient for impurities in Ge and Si," *Journal of Applied Physics*, vol. 33, no. 4, p. 1615, 1962.
- [49] T. G. Kim, J. M. Warrender, and M. J. Aziz, "Strong sub-band-gap infrared absorption in silicon supersaturated with sulfur," *Applied Physics Letters*, vol. 88, no. 24, 2006.
- [50] M. Tabbal, T. Kim, J. M. Warrender, M. J. Aziz, B. L. Cardozo, and R. S. Goldman, "Formation of single crystal sulfur supersaturated silicon based junctions by pulsed laser melting," *Journal of Vacuum Science Technology B*, vol. 25, no. 6, pp. 1847–1852, 2007.
- [51] T. H. Her, R. J. Finlay, C. Wu, S. Deliwala, and E. Mazur, "Microstructuring of silicon with femtosecond laser pulses," *Applied Physics Letters*, vol. 73, no. 12, pp. 1673–1675, 1998.
- [52] T. H. Her, R. J. Finlay, C. Wu, and E. Mazur, "Femtosecond laser-induced formation of spikes on silicon," *Applied Physics A – Materials Science Processing*, vol. 70, no. 4, pp. 383–385, 2000.
- [53] R. Younkin, J. E. Carey, E. Mazur, J. A. Levinson, and C. M. Friend, "Infrared absorption by conical silicon microstructures made in a variety of background gases using femtosecond-laser pulses," *Journal of Applied Physics*, vol. 93, no. 5, pp. 2626–2629, 2003.
- [54] M. Y. Shen, C. H. Crouch, J. E. Carey, and E. Mazur, "Femtosecond laser-induced formation of submicrometer spikes on silicon in water," *Applied Physics Letters*, vol. 85, no. 23, pp. 5694–5696, 2004.
- [55] J. E. Carey, *Femtosecond-laser Microstructuring of Silicon for Novel Optoelectronic Devices*. PhD thesis, Harvard University, 2004.

- [56] H. M. Vandriel, J. E. Sipe, and J. F. Young, "Laser-induced periodic surface-structure on solids - a universal phenomenon," *Physical Review Letters*, vol. 49, no. 26, pp. 1955–1958, 1982.
- [57] J. E. Sipe, J. F. Young, J. S. Preston, and H. M. Vandriel, "Laser-induced periodic surface-structure 1 – Theory," *Physical Review B*, vol. 27, no. 2, pp. 1141–1154, 1983.
- [58] J. F. Young, J. S. Preston, H. M. Vandriel, and J. E. Sipe, "Laser-induced periodic surface-structure 2 – Experiments on Ge, Si, Al, and brass," *Physical Review B*, vol. 27, no. 2, pp. 1155–1172, 1983.
- [59] J. F. Young, J. E. Sipe, and H. M. Vandriel, "Laser-induced periodic surface-structure 3 – Fluence regimes, the role of feedback, and details of the induced topography in germanium," *Physical Review B*, vol. 30, no. 4, pp. 2001–2015, 1984.
- [60] M. Y. Shen, C. H. Crouch, J. E. Carey, R. Younkin, E. Mazur, M. Sheehy, and C. M. Friend, "Formation of regular arrays of silicon microspikes by femtosecond laser irradiation through a mask," *Applied Physics Letters*, vol. 82, no. 11, pp. 1715–1717, 2003.
- [61] T. Baldacchini, J. E. Carey, M. Zhou, and E. Mazur, "Superhydrophobic surfaces prepared by microstructuring of silicon using a femtosecond laser," *Langmuir*, vol. 22, no. 11, pp. 4917–4919, 2006.
- [62] E. D. Diebold, N. H. Mack, S. K. Doorn, and E. Mazur, "Femtosecond laser-nanostructured substrates for surface-enhanced raman scattering," *Langmuir*, vol. 25, pp. 1790–1794, 2009.
- [63] B. R. Tull, J. E. Carey, E. Mazur, J. P. McDonald, and S. M. Yalisove, "Silicon surface morphologies after femtosecond laser irradiation," *MRS Bulletin*, vol. 31, no. 8, pp. 626–633, 2006.
- [64] B. R. Tull, J. E. Carey, M. A. Sheehy, C. Friend, and E. Mazur, "Formation of silicon nanoparticles and web-like aggregates by femtosecond laser ablation in a background gas," *Applied Physics A – Materials Science Processing*, vol. 83, no. 3, pp. 341–346, 2006.
- [65] C. Wu, C. H. Crouch, L. Zhao, J. E. Carey, R. Younkin, J. A. Levinson, E. Mazur, R. M. Farrell, P. Gothoskar, and A. Karger, "Near-unity below-band-gap absorption by microstructured silicon," *Applied Physics Letters*, vol. 78, no. 13, pp. 1850–1852, 2001.

- [66] C. H. Crouch, J. E. Carey, M. Shen, E. Mazur, and F. Y. Genin, "Infrared absorption by sulfur-doped silicon formed by femtosecond laser irradiation," *Applied Physics A – Materials Science Processing*, vol. 79, no. 7, pp. 1635–1641, 2004.
- [67] M. A. Sheehy, L. Winston, J. E. Carey, C. A. Friend, and E. Mazur, "Role of the background gas in the morphology and optical properties of laser-microstructured silicon," *Chemistry of Materials*, vol. 17, no. 14, pp. 3582–3586, 2005.
- [68] M. A. Sheehy, B. R. Tull, C. M. Friend, and E. Mazur, "Chalcogen doping of silicon via intense femtosecond-laser irradiation," *Materials Science and Engineering B – Solid State Materials for Advanced Technology*, vol. 137, no. 1–3, pp. 289–294, 2007.
- [69] C. H. Crouch, J. E. Carey, J. M. Warrender, M. J. Aziz, E. Mazur, and F. Y. Genin, "Comparison of structure and properties of femtosecond and nanosecond laser-structured silicon," *Applied Physics Letters*, vol. 84, no. 11, pp. 1850–1852, 2004.
- [70] B. R. Tull, M. Winkler, and E. Mazur, "The role of diffusion in broadband infrared absorption in chalcogen-doped silicon," *Applied Physics A – Materials Science Processing*, vol. 96, no. 2, 2009.
- [71] J. E. Carey, C. H. Crouch, M. Y. Shen, and E. Mazur, "Visible and near-infrared responsivity of femtosecond-laser microstructured silicon photodiodes," *Optics Letters*, vol. 30, no. 14, pp. 1773–1775, 2005.
- [72] B. R. Tull, *Femtosecond Laser Ablation of Silicon: Nanoparticles, Doping and Photovoltaics*. PhD thesis, Harvard University, 2007.
- [73] H. G. Grimmeiss, E. Janzen, H. Ennen, O. Schirmer, J. Schneider, R. Worner, C. Holm, E. Sirtl, and P. Wagner, "Tellurium donors in silicon," *Physical Review B*, vol. 24, no. 8, pp. 4571–4586, 1981.
- [74] P. Migliorato, A. W. Vere, and C. T. Elliott, "Sulfur-doped silicon background-limited infrared photodetectors near 77 K," *Applied Physics*, vol. 11, no. 3, pp. 295–297, 1976.
- [75] N. A. Sultanov, "Photoelectric properties of selenium-doped silicon," *Soviet Physics Semiconductors – USSR*, vol. 8, no. 9, pp. 1148–1149, 1975.
- [76] R. Stuck, E. Fogarassy, J. J. Grob, and P. Siffert, "Solubility limit of impurities in silicon after laser-induced melting," *Applied Physics*, vol. 23, no. 1, pp. 15–

- 19, 1980.
- [77] P. L. Liu, R. Yen, N. Bloembergen, and R. T. Hodgson, "Picosecond laser-induced melting and resolidification morphology on Si," *Applied Physics Letters*, vol. 34, no. 12, pp. 864–866, 1979.
- [78] J. M. Liu, R. Yen, H. Kurz, and N. Bloembergen, "Phase-transformation on and charged-particle emission from a silicon crystal-surface, induced by picosecond laser-pulses," *Applied Physics Letters*, vol. 39, no. 9, pp. 755–757, 1981.
- [79] J. M. Liu, H. Kurz, and N. Bloembergen, "Picosecond time-resolved plasma and temperature-induced changes of reflectivity and transmission in silicon," *Applied Physics Letters*, vol. 41, no. 7, pp. 643–646, 1982.
- [80] K. L. Merkle, H. Baumgart, R. H. Uebbing, and F. Phillipp, "Picosecond laser-pulse irradiation of crystalline silicon," *Applied Physics Letters*, vol. 40, no. 8, pp. 729–731, 1982.
- [81] D. Vonderlinde and N. Fabricius, "Observation of an electronic plasma in picosecond laser annealing of silicon," *Applied Physics Letters*, vol. 41, no. 10, pp. 991–993, 1982.
- [82] L. A. Lompre, J. M. Liu, H. Kurz, and N. Bloembergen, "Time-resolved temperature-measurement of picosecond laser irradiated silicon," *Applied Physics Letters*, vol. 43, no. 2, pp. 168–170, 1983.
- [83] C. V. Shank, R. Yen, and C. Hirlimann, "Time-resolved reflectivity measurements of femtosecond-optical-pulse induced phase-transitions in silicon," *Physical Review Letters*, vol. 50, no. 6, pp. 454–457, 1983.
- [84] C. V. Shank, R. Yen, and C. Hirlimann, "Femtosecond-time-resolved surface structural dynamics of optically-excited silicon," *Physical Review Letters*, vol. 51, no. 10, pp. 900–902, 1983.
- [85] D. Hulin, M. Combescot, J. Bok, A. Migus, J. Y. Vinet, and A. Antonetti, "Energy-transfer during silicon irradiation by femtosecond laser-pulse," *Physical Review Letters*, vol. 52, no. 22, pp. 1998–2001, 1984.
- [86] P. Saeta, J. K. Wang, Y. Siegal, N. Bloembergen, and E. Mazur, "Ultrafast electronic disordering during femtosecond laser melting of GaAs," *Physical Review Letters*, vol. 67, no. 8, pp. 1023–1026, 1991.
- [87] P. Stampfli and K. H. Bennemann, "Time-dependence of the laser-induced

- femtosecond lattice instability of Si and GaAs - role of longitudinal optical distortions,” *Physical Review B*, vol. 49, no. 11, pp. 7299–7305, 1994.
- [88] D. von der Linde, K. Sokolowski-Tinten, and J. Bialkowski, “Laser-solid interaction in the femtosecond time regime,” *Applied Surface Science*, vol. 110, pp. 1–10, 1997.
- [89] D. von der Linde and K. Sokolowski-Tinten, “The physical mechanisms of short-pulse laser ablation,” *Applied Surface Science*, vol. 154, pp. 1–10, 2000.
- [90] K. Sokolowski-Tinten, J. Bialkowski, A. Cavalleri, D. von der Linde, A. Oparin, J. Meyer-ter Vehn, and S. I. Anisimov, “Transient states of matter during short pulse laser ablation,” *Physical Review Letters*, vol. 81, no. 1, pp. 224–227, 1998.
- [91] J. Bonse, S. Baudach, J. Kruger, W. Kautek, and M. Lenzner, “Femtosecond laser ablation of silicon-modification thresholds and morphology,” *Applied Physics A – Materials Science Processing*, vol. 74, no. 1, pp. 19–25, 2002.
- [92] J. R. Chelikowsky and M. L. Cohen, “Nonlocal pseudopotential calculations for electronic-structure of 11 diamond and zincblende semiconductors,” *Physical Review B*, vol. 14, no. 2, pp. 556–582, 1976.
- [93] M. A. Green and M. J. Keevers, “Optical-properties of intrinsic silicon at 300 K,” *Progress in Photovoltaics*, vol. 3, no. 3, pp. 189–192, 1995.
- [94] S. Backus, C. G. Durfee, M. M. Murnane, and H. C. Kapteyn, “High power ultrafast lasers,” *Review of Scientific Instruments*, vol. 69, no. 3, pp. 1207–1223, 1998.
- [95] U. Keller, “Recent developments in compact ultrafast lasers,” *Nature*, vol. 424, no. 6950, pp. 831–838, 2003.
- [96] M. O. Thompson, J. W. Mayer, A. G. Cullis, H. C. Webber, N. G. Chew, J. M. Poate, and D. C. Jacobson, “Silicon melt, regrowth, and amorphization velocities during pulsed laser irradiation,” *Physical Review Letters*, vol. 50, no. 12, pp. 896–899, 1983.
- [97] P. H. Bucksbaum and J. Bokor, “Rapid melting and regrowth velocities in silicon heated by ultraviolet picosecond laser-pulses,” *Physical Review Letters*, vol. 53, no. 2, pp. 182–185, 1984.
- [98] I. W. Boyd, S. C. Moss, T. F. Boggess, and A. L. Smirl, “Temporally resolved imaging of silicon surfaces melted with intense picosecond 1 μm laser-pulses,” *Applied Physics Letters*, vol. 46, no. 4, pp. 366–368, 1985.

- [99] P. Stampfli and K. H. Bennemann, "Theory for the laser-induced instability of the diamond structure of Si, Ge and C," *Progress in Surface Science*, vol. 35, no. 1-4, pp. 161–164, 1990.
- [100] A. Cavalleri, K. Sokolowski-Tinten, J. Bialkowski, M. Schreiner, and D. von der Linde, "Femtosecond melting and ablation of semiconductors studied with time of flight mass spectroscopy," *Journal Of Applied Physics*, vol. 85, no. 6, pp. 3301–3309, 1999.
- [101] S. I. Kudryashov and V. I. Emel'yanov, "Band gap collapse and ultrafast 'cold' melting of silicon during femtosecond laser pulse," *Jetp Letters*, vol. 73, no. 5, pp. 228–231, 2001.
- [102] D. P. Korfiatis, K. A. T. Thoma, and J. C. Vardaxoglou, "Conditions for femtosecond laser melting of silicon," *Journal of Physics D – Applied Physics*, vol. 40, no. 21, pp. 6803–6808, 2007.
- [103] R. R. Gattass and E. Mazur, "Femtosecond laser micromachining in transparent materials," *Nature Photonics*, vol. 2, no. 4, pp. 219–225, 2008.
- [104] W. Kern, *Handbook of Semiconductor Wafer Cleaning Technology: Science, Technology, and Applications*. New Jersey: Noyes Publications, 1993.
- [105] M. Sher, M. Winkler, J. Sullivan, and E. Mazur, "Corrections to reflection measurements using an integrating sphere," *unpublished*, 2009.
- [106] E. Hall, "On a new action of the magnet on electric currents," *American Journal of Mathematics*, vol. 2, pp. 287–292, 1879.
- [107] E. H. Putley, *The Hall Effect and Semi-Conductor Physics*. New York: Dover Publications, Inc., 1960.
- [108] A. C. Beer, *Galvanomagnetic Effects in Semiconductors*. New York: Academic Press, 1963.
- [109] H. Wieder, *Laboratory notes on electrical and galvanomagnetic measurements*. New York: Elsevier Scientific Publishing Company, 1979.
- [110] C. Chien and C. Westgate, eds., *The Hall Effect and Its Applications*. New York: Plenum Press, 1979.
- [111] P. Blood and J. W. Orton, "Electrical characterization of semiconductors," *Reports on Progress in Physics*, vol. 41, no. 2, pp. 157–257, 1978.

- [112] D. A. Anderson and N. Apsley, "The Hall effect in III-V semiconductor assessment," *Semiconductor Science and Technology*, vol. 1, no. 3, pp. 187–202, 1986.
- [113] J. W. Orton and M. J. Powell, "The Hall effect in polycrystalline and powdered semiconductors," *Reports on Progress in Physics*, vol. 43, no. 11, pp. 1263–1307, 1980.
- [114] J. Blakemore, *Semiconductor Statistics*. New York: Dover Publications, Inc, 1987.
- [115] L. van der Pauw, "A method of measuring the resistivity and Hall coefficient on lamellae of arbitrary shape," *Philips Technical Review*, vol. 20, no. 8, p. 220, 1958.
- [116] R. Chwang, B. J. Smith, and C. R. Crowell, "Contact size effects on Van Der Pauw method for resistivity and Hall-coefficient measurement," *Solid-State Electronics*, vol. 17, no. 12, pp. 1217–1227, 1974.
- [117] D. W. Koon, "Effect of contact size and placement, and of resistive inhomogeneities on Van Der Pauw measurements," *Review of Scientific Instruments*, vol. 60, no. 2, pp. 271–274, 1989.
- [118] D. K. Devries and A. D. Wieck, "Potential distribution in the Van Der Pauw technique," *American Journal of Physics*, vol. 63, no. 12, pp. 1074–1078, 1995.
- [119] C. Yamanouchi, K. Mizuguchi, and W. Sasaki, "Electric conduction in phosphorus doped silicon at low temperatures," *Journal of the Physical Society of Japan*, vol. 22, no. 3, p. 859, 1967.
- [120] J. Olea, G. Gonzalez-Diaz, D. Pastor, and I. Martil, "Electronic transport properties of Ti-impurity band in Si," *Journal of Physics D-Applied Physics*, vol. 42, no. 8, 2009.
- [121] G. Gonzalez-Diaz, J. Olea, I. Martil, D. Pastor, A. Marti, E. Antolin, and A. Luque, "Intermediate band mobility in heavily titanium-doped silicon layers," *Solar Energy Materials and Solar Cells*, vol. 93, no. 9, pp. 1668–1673, 2009.
- [122] G. A. Thomas, M. Capizzi, F. Derosa, R. N. Bhatt, and T. M. Rice, "Optical study of interacting donors in semiconductors," *Physical Review B*, vol. 23, no. 10, pp. 5472–5494, 1981.
- [123] J. Monecke, W. Siegel, E. Ziegler, and G. Kuhnel, "On the concentration-

- dependence of the thermal impurity-to-band activation-energies in semiconductors,” *Physica Status Solidi B – Basic Research*, vol. 103, no. 1, pp. 269–279, 1981.
- [124] P. P. Edwards and M. J. Sienko, “The transition to the metallic state,” *Accounts of Chemical Research*, vol. 15, no. 3, pp. 87–93, 1982.
- [125] M. Marder, *Condensed Matter Physics*. New York: John Wiley Sons, Inc., 2000.
- [126] P. Norton, T. Braggins, and H. Levinstein, “Impurity and lattice scattering parameters as determined from Hall and mobility analysis in n-type silicon,” *Physical Review B*, vol. 8, no. 12, pp. 5632–5653, 1973.
- [127] D. Camphausen, H. M. James, and R. J. Sladek, “Influence of hydrostatic pressure and temperature on deep donor levels of sulfur in silicon,” *Physical Review B*, vol. 2, no. 6, p. 1899, 1970.
- [128] A. A. Lebedev, N. A. Sultanov, and V. Tuchkevich, “N-type negative resistance and photoconductivity of sulfur-doped p-type Si,” *Soviet Physics Semiconductors – USSR*, vol. 5, no. 1, p. 25, 1971.
- [129] E. Janzen, R. Stedman, G. Grossmann, and H. G. Grimmeiss, “High-resolution studies of sulfur-related and selenium-related donor centers in silicon,” *Physical Review B*, vol. 29, no. 4, pp. 1907–1918, 1984.
- [130] H. G. Grimmeiss, E. Janzen, and B. Skarstam, “Deep sulfur-related centers in silicon,” *Journal of Applied Physics*, vol. 51, no. 8, pp. 4212–4217, 1980.
- [131] M. Smith *unpublished*, 2009.
- [132] H. Overhof, M. Otte, M. Schmidtke, U. Backhausen, and R. Carius, “The transport mechanism in micro-crystalline silicon,” *Journal of Non-Crystalline Solids*, vol. 227, pp. 992–995, 1998.
- [133] S. Sze, *Physics of Semiconductor Devices*. New York: John Wiley Sons, Inc., 2 ed., 1981.
- [134] J. Gunn, “On carrier accumulation, and the properties of certain semiconductor junctions,” *International Journal of Electronics*, vol. 4, no. 1, pp. 17–50, 1957.
- [135] T. Bronger and R. Carius, “Carrier mobilities in microcrystalline silicon films,” pp. 7486–7489, 2007.

- [136] W. Kaiser, P. H. Keck, and C. F. Lange, "Infrared absorption and oxygen content in silicon and germanium," *Physical Review*, vol. 101, no. 4, pp. 1264–1268, 1956.
- [137] M. J. Aziz and C. W. White, "Solute trapping in silicon by lateral motion of (111) ledges," *Physical Review Letters*, vol. 57, no. 21, pp. 2675–2678, 1986.
- [138] R. G. Wilson, "Depth distributions of sulfur implanted into silicon as a function of ion energy, ion fluence, and anneal temperature," *Journal of Applied Physics*, vol. 55, no. 10, pp. 3490–3494, 1984.
- [139] R. L. Petritz, "Theory of an experiment for measuring the mobility and density of carriers in the space-charge region of a semiconductor surface," *Physical Review*, vol. 110, no. 6, pp. 1254–1262, 1958.
- [140] J. W. Mayer, O. J. Marsh, G. A. Shifrin, and R. Baron, "Ion implantation of silicon 2 – electrical evaluation using Hall-effect measurements," *Canadian Journal of Physics*, vol. 45, no. 12, p. 4073, 1967.
- [141] W. E. Krag, W. H. Kleiner, H. J. Zeiger, and S. Fischler, "Sulfur donors in silicon – infrared transitions and effects of calibrated uniaxial stress," *Journal of the Physical Society of Japan*, vol. S 21, p. 230, 1966.
- [142] M. Lundstrom, *Fundamentals of Carrier Transport*. Cambridge: University Press, 1990.
- [143] I. Granacher and W. Czaja, "Mobility and electron spin resonance linewidth in phosphorus doped silicon," *Journal of Physics and Chemistry of Solids*, vol. 28, no. 2, p. 231, 1967.
- [144] N. F. Mott, "Conduction in glasses containing transition metal ions," *Journal of Non-Crystalline Solids*, vol. 1, no. 1, pp. 1–17, 1968.
- [145] S. Z. Karazhanov, "Impurity photovoltaic effect in indium-doped silicon solar cells," *Journal of Applied Physics*, vol. 89, no. 7, pp. 4030–4036, 2001.
- [146] T. R. Polte, M. Y. Shen, J. Karavitis, M. Montoya, J. Pendse, S. Xia, E. Mazur, and D. E. Ingber, "Nanostructured magnetizable materials that switch cells between life and death," *Biomaterials*, vol. 28, no. 17, pp. 2783–2790, 2007.
- [147] J. Rayleigh, *The Theory of Sound*. London: Macmillan and co., 1 ed., 1877.
- [148] B. Newman, J. Sullivan, M. Winkler, M. Sher, M. Marcus, M. Smith, S. Gradecek, E. Mazur, and T. Buonassisi, "Illuminating the mechanism for sub-

bandgap absorption in chalcogen doped silicon materials for PV applications,” in *European Union Photovoltaic Solar Energy Conference*, (Hamburg, Germany), 2009.